# Sound propagation modelling in urban areas : from the street scale to the neighbourhood scale

Miguel Ángel Molerón Bermúdez

Université du Maine
École Doctorale: Sciences Pour l'Ingénieur, Géosciences, Architecture

**Doctoral thesis**
in Acoustics

**Miguel Ángel Molerón Bermúdez**

# Sound propagation modelling in urban areas: from the street scale to the neighbourhood scale

Defended on November 30, 2012

Examining committee:

| | | |
|---|---|---|
| **R. Marchiano** | Professor, Institut Jean Le Rond d'Alembert, Paris | Reviewer |
| **J. Vasseur** | Professor, IEMN, Lille | Reviewer |
| **P.-O. Mattei** | CNRS Researcher, LMA, Marseille | Examiner |
| **V. Valeau** | Professor, Institut PPRIME, Poitiers | Examiner |
| **F. Treyssède** | Researcher, IFSTTAR, Bouguenais | Invited |
| **J. Picaut** | Research Director, IFSTTAR, Bouguenais | Advisor |
| **S. Félix** | CNRS Researcher, LAUM, Le Mans | Co-advisor |
| **V. Pagneux** | CNRS Research Director, LAUM, Le Mans | Co-advisor |
| **O. Richoux** | Professor, LAUM, Le Mans | Co-advisor |

Université du Maine
École Doctorale: Sciences Pour l'Ingénieur, Géosciences, Architecture

**Thèse de doctorat**
en Acoustique

**Miguel Ángel Molerón Bermúdez**

---

# Modélisation de la propagation acoustique en milieu urbain : de la rue au quartier

---

Soutenue le 30 novembre 2012 devant le jury composé de :

| | | |
|---|---|---|
| **R. Marchiano** | Professeur, Institut Jean Le Rond d'Alembert, Paris | Rapporteur |
| **J. Vasseur** | Professeur, IEMN, Lille | Rapporteur |
| **P.-O. Mattei** | Chargé de recherche HDR, LMA, Marseille | Examinateur |
| **V. Valeau** | Maître de conférences, Institut PPRIME, Poitiers | Examinateur |
| **F. Treyssède** | Chargé de recherche, IFSTTAR, Bouguenais | Membre invité |
| **J. Picaut** | Directeur de recherche, IFSTTAR, Bouguenais | Directeur de thèse |
| **S. Félix** | Chargé de recherche, LAUM, Le Mans | Co-directeur de thèse |
| **V. Pagneux** | Directeur de recherche, LAUM, Le Mans | Co-directeur de thèse |
| **O. Richoux** | Maître de conférences HDR, LAUM, Le Mans | Co-directeur de thèse |

# Abstract

The improvement of the urban sound environment requires a good understanding of the acoustic propagation in urban areas. Available commercial softwares give the possibility to simulate urban acoustic fields at relatively low computational costs. However, these tools are mainly based on energy methods that do not contain information on the phase. Therefore, these tools are unable to capture interference effects (*e.g.*, resonances), providing a limited physical description of the acoustic field. Conversely, classical wave methods such as FEM, BEM or FDTD give the possibility to model interference effects, but their use is often restricted to very low frequencies due to discretisation and the huge extension of the propagation domain.

The main goal of this thesis is to develop efficient wave methods for the acoustic propagation modelling in extended urban areas, both in the frequency and time domain. The proposed approach is based on a coupled modal–finite elements formulation. The key idea is to consider the urban canyon as an open waveguide with a modal basis composed of leaky modes, *i.e.*, modes that radiate part of their energy into the atmosphere as they propagate. The approach combines a multimodal description of the acoustic field in the longitudinal direction and a finite elements computation of the transverse eigenmodes. This coupled approach, which has been successfully implemented at the scale of a single street, is extended in the present manuscript at a larger scale (the neighbourhood scale), in order to model problems arising in propagation domains containing many interconnected streets. A time domain version of the method, containing only the least damped mode, is also proposed.

Using these methods, we investigate wave phenomena arising in specific urban configurations, as forbidden frequency bands in periodic networks of interconnected streets, and resonances in inner yards. It is found that, despite the presence of significant radiative losses in the propagation medium, strong interference effects are still observed. Not only this result highlights the relevance of a wave approach to describe accurately urban acoustic fields at low frequencies, but it suggest the potential use of these phenomena to control the acoustic propagation in urban environments.

The last part of this dissertation presents a preliminary study on the use of metasurfaces (surfaces decorated with an array of resonators) to improve the performance

of noise barriers. It is shown that, exciting resonances in these structures, it is possible to achieve some unconventional behaviours, including negative angles of reflection and low frequency sound absorption.

# Résumé

Afin de réduire le bruit dans les villes, il est nécessaire d'avoir une bonne compréhension de la propagation acoustique en milieu urbain. Il existe aujourd'hui des logiciels commerciaux qui permettent de modéliser des champs acoustiques urbains à des coûts de calcul raisonnables. Toutefois, ces outils sont basés principalement sur des approches énergétiques qui ne contiennent pas d'informations sur la phase. Pour cette raison, elles ne permettent pas la prise en compte d'effets d'interférence (par exemple, des résonances), nous offrant ainsi une description physique limitée du champ acoustique. Inversement, des méthodes ondulatoires classiques (FEM, BEM, FDTD) permettent de prendre en compte ces effets. Or, en raison de la discrétisation et de la grande extension du domaine de propagation, leur utilisation est généralement limitée aux très basses fréquences.

L'objectif principal de cette thèse est de développer des méthodes ondulatoires performants, dans le domaine fréquentiel et temporel, nous permettant de modéliser la propagation acoustique dans des zones urbaines étendues. L'approche proposée est basée sur une formulation mixte modale–éléments finis. L'idée clé de cette méthode est de considérer la rue comme un guide d'ondes ouvert, dont la base modale est composée de modes de fuite (modes qui rayonnent une partie de leur énergie en se propageant). Cette approche combine une description multimodale du champ acoustique dans la direction longitudinale et un calcul par éléments finis des modes propres transverses. L'approche a été mise en œuvre précédemment à l'échelle d'une seule rue. Dans cette thèse, nous nous intéressons à l'extension de la méthode à l'échelle du quartier, afin de modéliser la propagation dans des milieux contenant un grand nombre de rues interconnectées. Une version simplifiée dans le domaine temporel, contenant uniquement le mode de propagatif le moins fuyant, est également développée.

En nous basant sur ces approches, nous étudions des phénomènes ondulatoires qui peuvent apparaître dans des configurations urbaines particulières. Plus précisément, nous nous intéressons à l'interaction des modes de la rue avec des résonances dans une cour intérieure adjacente, ainsi qu'à la formation de bandes de fréquences interdites dans des réseaux périodiques de rues interconnectées. Le résultat principal de cette étude est que, malgré la forte présence de pertes par radiation dans le milieu, des effets de résonance importants peuvent encore se produire. Les résultats presentés dans ce manuscrit mettent en évidence l'importance d'une approche ondulatoire pour décrire correctement des champs acoustiques aux basses fréquences, et ils suggèrent l'usage

potentiel de ces phénomènes afin de contrôler la propagation acoustique dans le milieu.

Enfin, nous présentons une étude sur l'utilisation de métasurfaces (surfaces contenant un réseau de résonateurs) pour améliorer la performance des murs antibruit. Nous démontrons que, grâce à l'excitation des résonances locales sur la métasurface, il est possible d'obtenir des propriétés non conventionnelles, comme par exemple des angles de réflexion négatifs ou de l'absorption acoustique aux basses fréquences.

# Contents

# Introduction

## General context and motivation

As a result of the growing concentration of population in urban areas, environmental noise is nowadays recognized as a public health problem. Accordingly to the World Health Organization, environmental noise in Western European cities generates the loss of, at least, 1 million years of healthy life per year [89]. Face to this problem, public authorities are taking actions since the last two decades with the aim of improving the sound environment in cities. In France, the law 92-1444 of 31 December 1992 gives a legal framework to the prevention and reduction of noise annoyance. At European level, the European Commission adopted the Directive 2002/49/EC that foresees the realisation of noise maps in the major Western European cities. Accordingly to this Directive, cities with more than 250000 inhabitants had to provide their noise maps in 2006, and cities with more than 100000 inhabitants are expected to do the same during 2012.

In this context, urban acoustics plays an essential role, as it provides scientific support to define strategies against noise annoyance. Studies in urban acoustics are divided in three main topics: (i) noise sources, mainly due to human activity (transportation means or heavy machinery, among others); (ii) the propagation of acoustic waves in the environment; and (iii) the perception of noise and its effects on health. The present thesis falls within the second topic.

Extensive researches over the past two decades have given rise to a variety of computational methods for the acoustic propagation modelling in urban environments (see the reference books [6, 50] for a detailed review). They can be classified into energy methods and wave methods. Energy methods are based on the estimation of quadratic quantities, *i.e.*, acoustic power or acoustic intensity. Examples are the ray tracing method [11], the image source method [20, 44, 53, 88], statistical approaches of particle transport [68, 69] and the radiosity method [9, 48, 49]. Due to their relatively low computational costs, these methods are the basis of the engineering tools that are commonly used to

predict urban acoustic fields. However, since in general, these methods do not take into account the phase information, they are usually limited to high frequencies. On the other hand, wave methods are based on the estimation of the pressure and the particle velocity through the resolution of the fundamental equations of acoustics. Examples of wave methods are the finite elements method (FEM), the boundary elements method (BEM), the finite difference time domain method (FDTD) [1, 2, 34, 71, 82], the equivalent sources approach [37, 39, 59], methods based on the parabolic equation [22, 52, 72], the transmission line matrix method (TLM) [33], the Fourier pseudospectral time domain method (PSTD) [37], and the multimodal method [13, 14, 19, 66, 67]. Although these methods are valid for any frequency range, their use is usually restricted to low frequencies due to discretisation.

The main goal of this thesis is to develop efficient frequency and time domain methods for the acoustic propagation modelling in extended urban areas. The starting point of this thesis is an earlier work by A. Pelat [65] in the Urban Acoustics research group at Laboratoire d'Acoustique de l'Universié du Maine. In his work, Pelat demonstrated the suitability of a multimodal approach to model the acoustic propagation in urban canyons. This approach, widely used in the study of wave propagation in waveguides [5, 28, 64, 76], consists in developing the acoustic field on the basis of eigenmodes of the transverse waveguide section. The key point when implementing this technique in the context of urban acoustics is to consider the street canyon as an open waveguide where waves are partly guided between buildings and partly radiated into the atmosphere. In such a waveguide, the modal basis is composed of leaky modes [42], complex modes that radiate energy to the surrounding media as they propagate. Since an analytical calculation of these modes is very difficult (if not impossible) in the general case, a coupled modal–finite elements method (hereafter called the modal–FE method) was proposed.

The modal–FE approach combines a multimodal description of the acoustic field in the longitudinal direction and a FE computation of the transverse waveguide modes. Solving the transverse problem numerically enables us to model complicated geometries and boundary conditions. On the other hand, since only the transverse section is meshed, the computational costs remain relatively low compared to full numerical methods. These features were exploited in [65] to investigate problems at the scale of a single street, including acoustic scattering by irregular facades, the presence of materials with different acoustic impedance or the effect of varying meteorological conditions on acoustic propagation. The present thesis focuses on extending this multimodal approach at the neighbourhood scale, in order to investigate problems arising in propagation domains containing many interconnected streets.

## Overview of the document

This dissertation is organised in six chapters. Chapter 1 introduces the principles of the modal–FE method using two different formulations. The first one is the initial value problem formulation proposed by Pelat [65], in which the source is modelled as

known pressure field at the input cross-section of the street canyon. The second one is a Green's function formulation, in which the source is modelled as a point source. The method is illustrated with several examples showing the acoustic propagation in street canyons containing different types of right–angled intersections.

Chapter 2 investigates the interaction of leaky modes propagating on the street with resonances in an adjacent courtyard. Chapter 4 presents a study of sound propagation in regular urban areas, regarded as a periodic lattice of interconnected streets. The aim of this Chapter is to investigate the formation of forbidden frequency bands in the urban environment, paying a particular attention to the interplay between multiple scattering and radiative losses, which are a distinctive feature of urban areas. Prior to this study, Chapter 3 introduces the basic concepts of wave propagation in periodic media using the *classical* multimodal method.

The results presented in Chapters 2 and 4 are confronted to a set of experiments performed on a scale model of urban area. The experimental results are in good agreement with the numerical predictions, which allows us to validate the proposed approach.

Chapter 5 presents a simplified time domain model of the acoustic propagation in networks of interconnected streets. The method is based on a previous characterisation in the frequency domain of all the elements forming the urban area (streets and intersections), which is performed using the modal–FE method. The data resulting from this characterisation is traduced to the time domain using Fourier analysis, and an algorithm is developed to compute the multiple wave scattering in the network.

Finally, Chapter 6 presents a study on the use of metasurfaces to improve the performance of noise barriers. We demonstrate the possibility to achieve unconventional by behaviour exploiting local resonances in these structures, such as negative angles of reflection and low frequency sound absorption.

# Chapter 1

# The modal–FE method

This Chapter introduces the modal–FE method. For clarity, the method is first presented in the case two-dimensional (2D) geometries in Sec. 1.1. Two formulations are proposed: an initial value problem formulation, in which the source is modelled as a pressure field imposed on the input cross–section; and a Green's function formulation, in which the source is modelled as a point source. The extension of the method to three-dimensional (3D) geometries is presented in Sec. 1.2, together with several exemples of acoustic fields in different types of right-angled intersections. Finally, Sec. 1.3 gives a summary of the main features of the method.

## 1.1 Formulation of the modal–FE method in 2D

### 1.1.1 Governing equations

Throughout this manuscript, we considered the propagation of linear acoustic waves in a non-dissipative inviscid fluid (air). Under these assumptions, the pressure $p$ and the particle velocity $\vec{v}$ satisfy the Euler equation,

$$\rho_0 \frac{\partial \vec{v}}{\partial t} + \vec{\nabla} p = 0, \tag{1.1}$$

and the mass conservation law,

$$\frac{1}{\rho_0 c_0^2} \frac{\partial p}{\partial t} + \vec{\nabla} \cdot \vec{v} = 0, \tag{1.2}$$

where $\rho_0$ is the mass density and $c_0$ is the sound speed in air. Combining equations (1.1) and (1.2) leads to the acoustic wave equation,

$$\left(\Delta - \frac{1}{c_0^2}\frac{\partial^2}{\partial_t^2}\right) p = 0, \tag{1.3}$$

which, assuming the time convention $\exp(-\jmath\omega t)$, turns into the Helmholtz equation in the harmonic regime,

$$\left(\Delta + k^2\right) p = 0, \tag{1.4}$$

with $k = \omega/c_0$ the wavenumber in free space and $\omega$ the angular frequency.

### 1.1.2 From open geometries to closed waveguides

Consider the geometry in Fig. 1.1a, consisting of a grounded half–space with a perfectly reflecting boundary along $z = -h$. The acoustic field in this domain is the solution of the following problem,

$$\left(\frac{\partial^2}{\partial x^2} + \frac{\partial^2}{\partial z^2} + k^2\right) p(x,z) = 0; \quad \forall x, \forall z \geqslant -h, \tag{1.5}$$

$$\frac{\partial}{\partial z} p(x,z) = 0; \quad \forall x, z = -h. \tag{1.6}$$

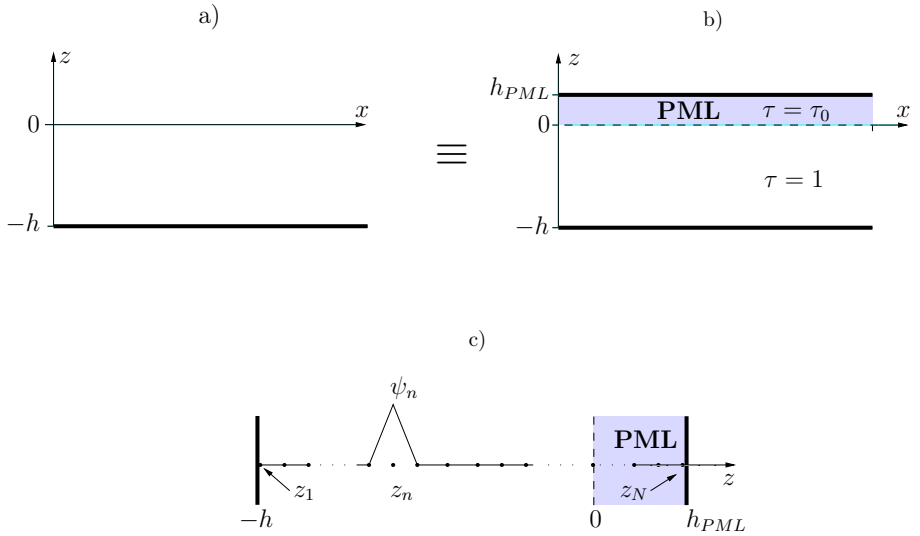


**Figure 1.1***: a) Grounded half-space, delimited by a rigid boundary at $z = -h$. b) Equivalent waveguide equivalent to the grounded half–space. c) FEM mesh of the transverse coordinate.*

The original open geometry shown in Fig. 1.1a is replaced with an equivalent closed waveguide represented in Fig. 1.1b. We accomplish this introducing a perfectly matched layer (PML) in the upper part, which takes into account the radiation in the vertical direction (see Appendix 1.A). The PML is characterised by the absorbing parameter $\tau(z)$. This parameter is chosen as a piecewise constant function of $z$, defined as

$$\tau(z) = \begin{cases} 1, & \text{if} \quad z \leqslant 0, \\ \tau_0, & \text{if} \quad z > 0, \end{cases} \tag{1.7}$$

with $\tau_0 = A\exp(\jmath\beta)$, and $A$ and $\beta$ real numbers fulfilling $A\beta > 0$. The problem to solve in this equivalent waveguide is

$$\left(\frac{\partial^2}{\partial x^2} + \frac{1}{\tau}\frac{\partial}{\partial z}\left(\frac{1}{\tau}\frac{\partial}{\partial z}\right) + k^2\right) p(x,z) \quad = 0; \quad \forall x, \forall z \in [-h, h_{\text{PML}}], \tag{1.8}$$

$$\frac{\partial}{\partial z} p(x,z) \quad = 0; \quad \forall x, z = -h, h_{\text{PML}}. \tag{1.9}$$

Notice that the solution to Eqs. (1.8) and (1.9) in the physical domain, $z \leqslant 0$, is identical to that in the original problem [Eqs. (1.5) and (1.6)].

Since the coordinate system is orthogonal and the geometry and boundary conditions are constant along the propagation direction $x$, the general solution to Eqs. (1.8) and (1.9) is separable, and can be written in the form of a modal expansion,

$$p(x,z) = \sum_i \phi_i(z)\left(A_i e^{\jmath k_{x,i} x} + B_i e^{-\jmath k_{x,i} x}\right), \tag{1.10}$$

with $i$ an integer, $k_{x,i}$ the longitudinal wavenumbers, fulfilling the dispersion relation $k_{x,i} = \sqrt{k^2 - \alpha_i^2}$, $\alpha_i$ the transverse wavenumbers, and $\phi_i(z)$ the transverse eigenfunctions. The couples $(\phi_i, \alpha_i^2)$ are the transverse eigenmodes of the guide, which elementary solutions of the transverse eigenproblem,

$$\left(\frac{1}{\tau}\frac{\partial}{\partial z}\left(\frac{1}{\tau}\frac{\partial}{\partial z}\right) + \alpha^2\right) \phi(z) \quad = 0; \quad \forall z \in [-h, h_{\text{PML}}], \tag{1.11}$$

$$\frac{\partial}{\partial z}\phi(z) \quad = 0; \quad z = -h, h_{\text{PML}}. \tag{1.12}$$

The transverse eigenproblem is solved numerically using the FE method. The coordinate $z$ is discretised on a $N$–nodes (see Fig. 1.1c) and $\phi(z)$ is developed on the basis of interpolating functions $\psi_n(z)$,

$$\phi(z) = \sum_{n=1}^{N} \Phi_n \psi_n(z) = {}^t\vec{\psi}(z)\vec{\Phi}, \tag{1.13}$$

The discrete form of the problem (1.11)-(1.12) takes the form

$$\left(\mathbf{K} - \alpha^2\mathbf{M}\right)\vec{\Phi} = \vec{0}, \tag{1.14}$$

or, equivalently,

$$\mathbf{M}^{-1}\mathbf{K}\vec{\Phi} = \alpha^2\vec{\Phi}, \tag{1.15}$$

where $\mathbf{M}$ is the mass matrix and $\mathbf{K}$ the stiffness matrix, which are respectively given by

$$M_{mn} = \int_{-h}^{h_{\mathrm{PML}}} \psi_m\psi_n dz, \tag{1.16}$$

and

$$K_{mn} = \int_{-h}^{0} \frac{\partial\psi_m}{\partial z}\frac{\partial\psi_n}{\partial z}dz + \int_{0}^{h_{\mathrm{PML}}} \frac{1}{\tau_0^2}\frac{\partial\psi_m}{\partial z}\frac{\partial\psi_n}{\partial z}dz. \tag{1.17}$$

The numerical eigenmodes of the transverse section of the guide are given as the eigenvectors $\vec{\Phi}_n$ and eigenvalues $\alpha_n^2$, $n = 1, 2, \cdots, N$ of the matrix $\mathbf{M}^{-1}\mathbf{K}$.

Now it is necessary to introduce the numerical eigenmodes in the formulation along the $x$–direction. We accomplish this developing the field $p(x, z)$ on the basis $\{\psi_n\}$:

$$p(x, z) = \sum_{n=1}^{N} P_n(x)\psi_n(z) = {}^t\vec{\psi}\vec{P}(x). \tag{1.18}$$

Hence, the problem defined in Eqs. (1.8)–(1.9) turns into the following discrete form,

$$\vec{P}''(x) + (k^2\mathbf{I} - \mathbf{M}^{-1}\mathbf{K})\vec{P}(x) = \vec{0}, \tag{1.19}$$

where the symbol $''$ denotes the second derivative with respect to $x$, $\mathbf{I}$ is the identity matrix and the element $P_n(x)$ of vector $\vec{P(x)}$ is the pressure at the $n$–th mesh node, at coordinate $x$: $P_n(x) = p(x, z_n)$. The general solution of Eq. (1.19) can be expressed as a function of the transverse eigenmodes $(\Phi_n, \alpha_n)$ as

$$\vec{P}(x) = \mathbf{\Phi}\left(\mathbf{D}(x)\vec{A} + \mathbf{D}(L - x)\vec{B}\right), \tag{1.20}$$

Note that equation (1.20) is the discrete form of Eq. (1.10), with $\mathbf{\Phi}$ the eigenvectors matrix ($\mathbf{\Phi} = [\vec{\Phi}_1, \vec{\Phi}_2, \cdots, \vec{\Phi}_N]$) and $\mathbf{D}(x)$ a diagonal matrix such that $D_{nn}(x) = \exp(\jmath k_{x,n}x)$, $k_{x,n} = (k^2 - \alpha_n^2)^{\frac{1}{2}}$. The unknown modal amplitudes of forward and backward modes, respectively $\vec{A}$ and $\vec{B}$, are obtained from the conditions at the waveguide extremities. The input condition at $x = 0$ (see Fig. 1.2) is defined as a known pressure field $\vec{P}(0)$. The output condition at $x = L$ is given as a generalised admittance matrix $\mathbf{Y}_L$, fulfilling $\vec{U}(L) = \mathbf{Y}_L\vec{P}(L)$, where $\vec{U}(x)$ contains the components of $\partial_x p$ on the basis $\{\psi_n\}$,

$$\vec{U}(x) = \mathbf{\Phi\Gamma}\left(\mathbf{D}(x)\vec{A} - \mathbf{D}(L - x)\vec{B}\right). \tag{1.21}$$

with $\Gamma_{nn} = \jmath k_{x,n}$ a diagonal matrix. From the pressure $\vec{P(x)}$ and its $x$–derivative $\vec{U}(x)$ at the extremities of the guide:

$$\vec{P}(0) = \mathbf{\Phi}\left(\vec{A} + \mathbf{D}(L)\vec{B}\right), \tag{1.22}$$

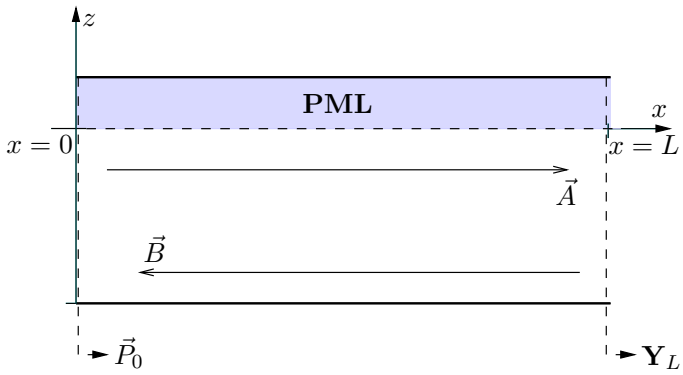


**Figure 1.2**: *Geometry of the initial value problem formulation.*

$$\vec{U}(0) = \mathbf{\Phi\Gamma}\left(\vec{A} - \mathbf{D}(L)\vec{B}\right), \tag{1.23}$$

$$\vec{P}(L) = \mathbf{\Phi}\left(\mathbf{D}(L)\vec{A} + \vec{B}\right), \tag{1.24}$$

$$\vec{U}(L) = \mathbf{\Phi\Gamma}\left(\mathbf{D}(L)\vec{A} - \vec{B}\right), \tag{1.25}$$

and combining Eqs. (1.22)–(1.25) we can obtain the unknown amplitude coefficients as

$$\vec{A} = \left[\mathbf{\Phi}\left(\mathbf{I} + \mathbf{D}(L)\mathbf{T}\mathbf{D}(L)\right)\right]^{-1}\vec{P}(0), \tag{1.26}$$

$$\vec{B} = \mathbf{T}\mathbf{D}(L)\vec{A}, \tag{1.27}$$

with $\mathbf{T} = \left(\mathbf{Y}_L\mathbf{\Phi} + \mathbf{\Phi\Gamma}\right)^{-1}\left(\mathbf{\Phi\Gamma} - \mathbf{Y}_L\mathbf{\Phi}\right)$. Additionally, it is possible to find the relationship between the input admittance matrix $\mathbf{Y}_0$ and the output admittance matrix $\mathbf{Y}_L$,

$$\mathbf{Y}_0 = \mathbf{\Gamma\Phi}\left(\mathbf{I} - \mathbf{D}(L)\mathbf{T}\mathbf{D}(L)\right)\left(\mathbf{I} + \mathbf{D}(L)\mathbf{T}\mathbf{D}(L)\right)^{-1}. \tag{1.28}$$

### 1.1.3 Green's function formulation

Consider now a point source situated at $(0, z_s)$ ( symbol "+" in Fig. 1.3). In this case, the acoustic field is the solution to the Green's problem

$$\left(\frac{\partial^2}{\partial x^2} + \frac{1}{\tau}\frac{\partial}{\partial z}\left(\frac{1}{\tau}\frac{\partial}{\partial z}\right) + k^2\right) g(x,z) = -\delta(x)\delta(z - z_s), \tag{1.29}$$

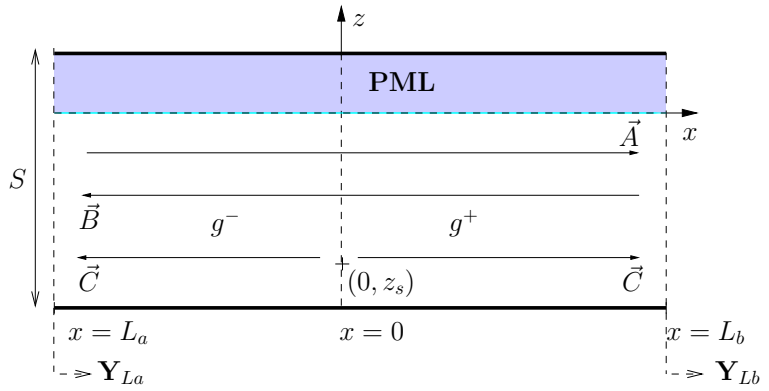


**Figure 1.3**: *Geometry of the Green's function formulation.*

with $(x_s, z_s)$ the position of the point source and $\delta$ the Dirac delta function. The Green's function $g(x, z)$ verifying the properties of continuity and derivative jump,

$$g^+(0,z) - g^-(0,z) = 0, \tag{1.30}$$

$$\partial_x g^+(0,z) - \partial_x g^-(0,z) = -\delta(z - z_s). \tag{1.31}$$

In Eqs. (1.30) and (1.31), the values of $g$ at $x < 0$ and $x > 0$ (see Fig. 1.3) are called, respectively, $g^-$ and $g^+$. As in the initial value problem case, the solution is developed on the basis of interpolating functions $\{\psi_n\}$:

$$g^-(x,z) = \sum_{n=1}^{N} G_n^-(x)\psi_n(z) = {}^t\vec{\psi}\vec{G}^-, \tag{1.32}$$

$$g^+(x,z) = \sum_{n=1}^{N} G_n^+(x)\psi_n(z) = {}^t\vec{\psi}\vec{G}^+, \tag{1.33}$$

and the general form of the solution can be expressed as

$$\vec{G}^-(x) = \mathbf{\Phi}\left(\mathbf{D}(x - L_a)\vec{A} + \mathbf{D}(L_b - x)\vec{B} + \mathbf{D}(-x)\vec{C}\right), \tag{1.34}$$

$$\vec{G}^+(x) = \mathbf{\Phi}\left(\mathbf{D}(x - L_a)\vec{A} + \mathbf{D}(L_b - x)\vec{B} + \mathbf{D}(x)\vec{C}\right). \tag{1.35}$$

In previous Eqs. (1.34) and (1.35), terms $\mathbf{D}(x)\vec{C}$ and $\mathbf{D}(-x)\vec{C}$ take into account the contribution of the direct field radiated by the point source, propagating away from the source in the direction of increasing and decreasing $x$, respectively. Terms $\mathbf{D}(x - L_a)\vec{A}$ and $\mathbf{D}(L_b - x)\vec{B}$ represent the contribution of modes reflected at the extremities of the guide, having their phase origin at $x = L_a$ and $x = L_b$, respectively.

Multiplying Eq. (1.31) by $\psi_n$ and integrating over the section $S$, we obtain [given Eqs. (1.34) and (1.35)]

$$\mathbf{M\Phi\Gamma}\left(\vec{C}+\vec{C}\right) = -\vec{\psi}(zs), \tag{1.36}$$

which leads to the expression for the coefficients $\vec{C}$,

$$\vec{C} = -\frac{1}{2}(\mathbf{M\Phi\Gamma})^{-1}\vec{\psi}(z_s). \tag{1.37}$$

The remaining coefficients $\vec{A}$ and $\vec{B}$ are obtained from the output admittance matrices $\mathbf{Y}_{La}$ and $\mathbf{Y}_{Lb}$ $x = L_a$ and $x = L_b$,

$$\vec{A} = \mathbf{T}_a\mathbf{D}(L_a)\vec{C}, \tag{1.38}$$

$$\vec{B} = \mathbf{T}_b\mathbf{D}(L_b)\vec{C}, \tag{1.39}$$

with $\mathbf{T}_a = \left(\mathbf{Y}_{La}\mathbf{\Phi} + \mathbf{\Phi\Gamma}\right)^{-1}\left(\mathbf{\Phi\Gamma} - \mathbf{Y}_{La}\mathbf{\Phi}\right)$ and $\mathbf{T}_b = \left(\mathbf{Y}_{Lb}\mathbf{\Phi} + \mathbf{\Phi\Gamma}\right)^{-1}\left(\mathbf{\Phi\Gamma} - \mathbf{Y}_{Lb}\mathbf{\Phi}\right)$.

### Validation in the case of an infinitely long waveguide

In the case of an infinitely long waveguide in the $x$–direction, the output admittance conditions $\mathbf{Y}_{La}$ and $\mathbf{Y}_{Lb}$ are defined as the characteristic admittance matrix of the guide, *i.e.*, the matrix that vanishes the amplitude of the the modes reflected at the extremities ($\vec{A} = \vec{B} = 0$). From Eqs. (1.38) and (1.39), it follows $\mathbf{Y}_{La} = \mathbf{Y}_{Lb} = \mathbf{\Phi\Gamma\Phi}^{-1}$. The solution of (1.29) is then given by

$$\vec{G}^{-}(x) = \mathbf{\Phi}\mathbf{D}(-x)\vec{C}, \tag{1.40}$$

$$\vec{G}^{+}(x) = \mathbf{\Phi}\mathbf{D}(x)\vec{C}. \tag{1.41}$$

On the other hand, the analytical Green's function $g_0$ of an infinite half–space is

$$g_0(x,z) = \frac{\jmath}{4}\left(H_0^1(k|\vec{r}-\vec{r_s}|) + H_0^1(k|\vec{r}-\vec{r}'_s|)\right) \tag{1.42}$$

with, $H_0^1$ the zero–th order Hankel function of the first kind, $|\vec{r}-\vec{r_s}| = \sqrt{(x-x_s)^2+(z-z_s)^2}$ the source–receptor distance and $|\vec{r}-\vec{r}'_s| = \sqrt{(x-x_s)^2+(z-z'_s)^2}$ the "image source"–receptor distance.

Fig. 1.4a shows the real part of the analytical solution and Fig. 1.4b shows the real part of the modal–FE method solution. The computational parameters are shown in the Tab. 1.2. We observe very good agreement between both solutions. In order to evaluate quantitatively the accuracy of the modal–FE solution, we calculate the relative error $\varepsilon$ as

$$\varepsilon = \left(\frac{\int_D \left\|g_{modal-FE} - g_0\right\|^2 dz}{\int_D \left\|g_0\right\|^2 dz}\right)^{1/2}, \tag{1.43}$$

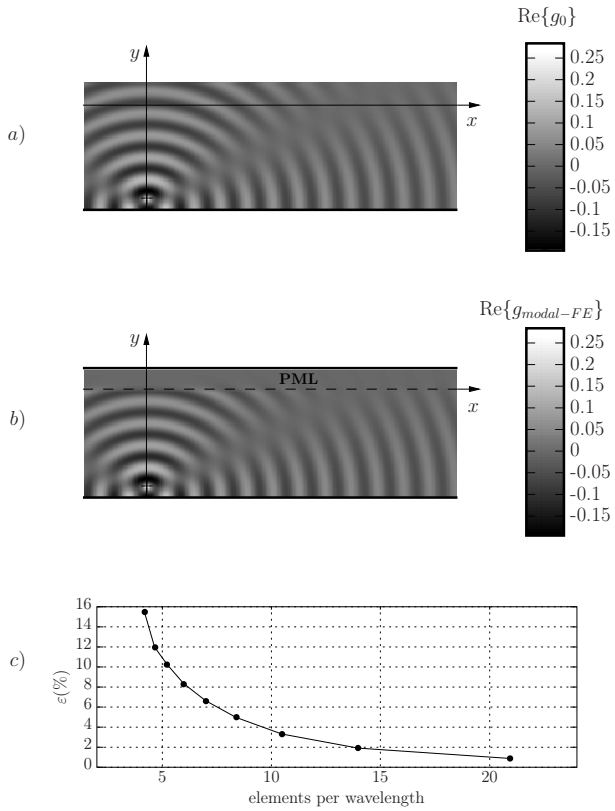


**Figure 1.4**: *Validation of the Green's function formulation. (a) Real part of the analytical solution $g_0$. (b) Real part of the modal–FE solution. (c) Relative error $\varepsilon$ versus the number of elements per wavelength.*

with $D$ the physical domain, $z \leqslant 0$. Fig. (1.4)c shows $\varepsilon$ as a function of the number of nodes per wavelength. We observe that the error converges to zero as the number of elements increases.

| Geometry | | | Source | | Transverse problem | PML | | |
|---|---|---|---|---|---|---|---|---|
| $h$ | $L_a/h$ | $L_b/h$ | $(x_s, z_s)/h$ | $\lambda/h$ | number of elements/$\lambda$ | $h_{\text{PML}}$ | $A$ | $\beta$ |
| 1 | $-0.5$ | 2.5 | $(0, -0.9)$ | 0.21 | $4 - 21$ | $\lambda$ | $\sqrt{2}$ | $\pi/4$ |

**Table 1.1**: *Parameters for the validation of the Green's function formulation.*

### 1.1.4 Study of discontinuities: the admittance matrix method

We consider now the propagation in a waveguide with sudden changes in the cross-section, as shown the Fig. 1.5. The side opening are substituted with PML, in order to obtaining an equivalent closed waveguide with piecewise constant cross–section. The transverse eigenmodes of each cross-section are computed by FE and the field in each straight segment takes the form of Eq. (1.20).

We use the impedance matrix method [64, 76] to find the relationship between the modal expansions of each straight segment. At the discontinuities, the field must fulfil the continuity equations for the pressure and its normal derivative,

$$\left\{\begin{array}{rcll} p^{(u)} & = & p^{(d)} & \text{on } S^{(u)} \cap S^{(d)}, \\ \partial_x p^{(u)} & = & \partial_x p^{(d)} & \text{on } S^{(u)} \cap S^{(d)}, \\ \partial_x p^{(u) \text{ or } (d)} & = & 0 & \text{on } S^{(u)} \setminus S^{(d)}, \end{array}\right. \tag{1.44}$$

where superscripts $(u)$ and $(d)$ indicate quantities upstream and downstream from the discontinuity (see Fig. 1.6). Developing Eqs. (1.44) on the basis $\{\psi_n\}$ leads to the matching relationships for pressure and admittance. For the sudden expansion, Fig. 1.6.a, the continuity equations are

$$\vec{P}^{(d)} = \left(\mathbf{Y}^{(d)}\right)^{-1} \mathbf{F} \mathbf{Y}^{(u)} \vec{P}^{(u)}, \tag{1.45}$$

$$\mathbf{Y}^{(u)} = \left[\mathbf{F}\left(\mathbf{Y}^{(d)}\right)^{-1} {}^{t}\mathbf{F}\right]^{-1}, \tag{1.46}$$

while for the sudden narrowing, Fig. 1.6.b, these equations are given by

$$\vec{P}^{(d)} = \mathbf{F}\vec{P}^{(u)}, \tag{1.47}$$

$$\mathbf{Y}^{(u)} = \mathbf{F}\mathbf{Y}^{(d)\,t}\mathbf{F}. \tag{1.48}$$

where $\mathbf{F}$ is called the matching matrix and ${}^{t}\mathbf{F}$ is its transposed. When identical meshes and identical interpolating functions are generated on both sides of the discontinuity,

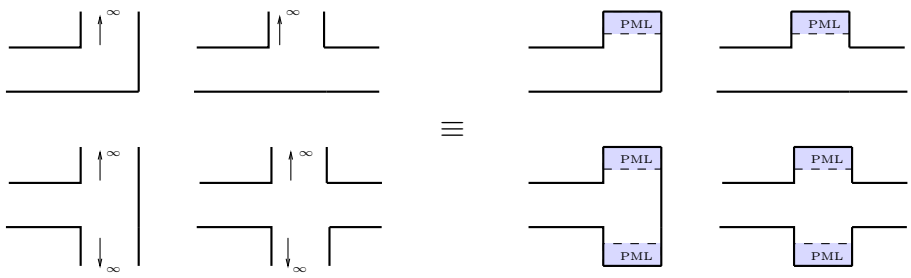


**Figure 1.5***: Modelling of right angled intersections as piecewise constant waveguides. The side openings towards the adjacent street are substituted with PML.*


**Figure 1.6**: *Possible types of discontinuities: a) suden Expansion and b) suden narrowing.*

the matching matrix is simply defined by [65]

$$F_{mn} = \begin{cases} 1, & \text{if } z_m^{(d)} = z_n^{(u)} \\ 0, & \text{otherwise.} \end{cases} \tag{1.49}$$

Then, given the admittance matrix at the output segment, the admittance can be computed, step by step, from the output to the input waveguide section using alternatively Eq. (1.28), in the straight segments and Eq. (1.46) or (1.48) at the discontinuities. Finally, from the source condition at the input segment, the field can be computed within the domain using Eqs. (1.20)–(1.27) in straight segments and Eq. (1.45) or (1.47) at the discontinuities. In the Green's function formulation is used, the field in the first segment is computed as indicated in Sec. 1.1.3.

### 1.1.5 Examples in 2D

Consider the case of a L–intersection between two perpendicular streets illustrated the Fig. 1.7. In the following, lengths are nondimensionalised using $h$ as the characteristic length. We also define the reduced wavenumber $k_a = kh/2\pi$. The geometrical parameters are $L_1/h = 5/3$ and $L_2 = 1$. The pressure is calculated using the initial value formulation, with a source condition $\vec{P}(0)$ in the form of a gaussian beam, given by the expression

| Geometry | | | Source | | Transverse problem | PML | | |
|---|---|---|---|---|---|---|---|---|
| $h$ | $L_a/h$ | $L_b/h$ | $(x_s, z_s)/h$ | $\lambda/h$ | number of elements/$\lambda$ | $h_{\text{PML}}$ | $A$ | $\beta$ |
| 1 | $-0.5$ | 2.5 | $(0, -0.9)$ | 0.21 | $4 - 21$ | $\lambda$ | $\sqrt{2}$ | $\pi/4$ |

**Table 1.2**: *Parameters for the validation of the Green's function formulation. Geometrical parameters*

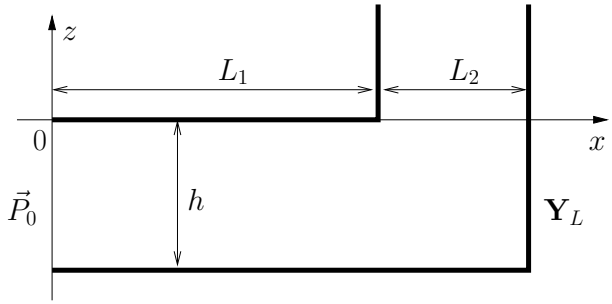


**Figure 1.7**: *Geometry of the L–intersection.*

$$P_{0n} = e^{-\frac{(z_n - z_s)^2}{2\sigma^2}}, \tag{1.50}$$

where $z_s = -h/2$ is the central point and $\sigma = 0.4$ the standard deviation, that determines the width of the beam. The rigid wall imposed an output admittance $\mathbf{Y}_L = [0]$. The maximum mesh size $mms$ is fixed to $mms = \lambda/30$, which generates 61 nodes in the first section and 91 nodes in the second section. The inner boundary of the PML is placed at $z = 0$, with parameters $h_{\mathrm{PML}} = \lambda, A = 2$ and $\beta = \pi/5$. The resulting acoustic field is shown in Fig. 1.8a. The result is compared to a full–FE simulation performed with the Matlab PDE Toolbox (Fig. 1.8b). The mesh size and the PML are the same in both cases, but in the full-FE computation the PML is placed at $z = 1$. Since the PML creates an anechoic termination, the result should be independent on the PML position. Therefore, both results should be identical in the region $z < 0$. To corroborate this, Fig. 1.8d superposes both solutions at $z = -0.9$. We observe a very good agreement between with the full-FE simulation.

If desired, it is possible to compute the acoustic field on the side street along the $z$–direction. For this, we expand the input pressure $p(x, z = 0)$ on the basis of the horizontal modes $\phi_m(x)$ transverse section of the side street,

$$\phi_m(x) = \sqrt{\frac{2 - \delta_{m0}}{L_2}} \cos\left(\frac{m\pi}{L_2}(x - L_1)\right), \tag{1.51}$$

with $m \in \mathbb{N}$. The pressure in the side street reads

$$p(x, z > 0) = \sum_{m=0}^{\infty} A_m \phi_m(x) e^{\jmath k_{z,m} z}, \tag{1.52}$$

with $k_{z,m} = \sqrt{k^2 - (m\pi/L_2)^2}$ and $A_m$ the coefficients of the modal expansion,

$$A_m = \int_{L_1}^{L_1+L_2} p(x, z = 0)\phi_m(x)\mathrm{d}x. \tag{1.53}$$

The result shown in the Fig. 1.8c is the same as that in Fig. 1.8b, except that the field along the adjacent street has been computed using Eq. (1.52). For this computation, the series (1.52) was truncated to 30 modes, from which 4 modes are propagative. A comparison with the reference solution at $z = 0.5$ (dashed arrows in Figs. 1.8b and 1.8c) is shown in Fig. 1.8d. The agreement with the full-FE computation is excellent.

Three extra examples using the Green's function formulation are shown in the Figs. 1.9a–c. The frequency of the point source is $k_a = kh/2\pi = 4.8$. The output condition is $\mathbf{Y}_L = [0]$ Fig. 1.9a and $\mathbf{Y}_L = \mathbf{\Phi\Gamma\Phi^{-1}}$ Fig. 1.9a and Fig. 1.9b. The maximum mesh size was fixed to $mms = \lambda/21$. Notice that the continuity of the pressure field at the discontinuities is fulfilled perfectly.

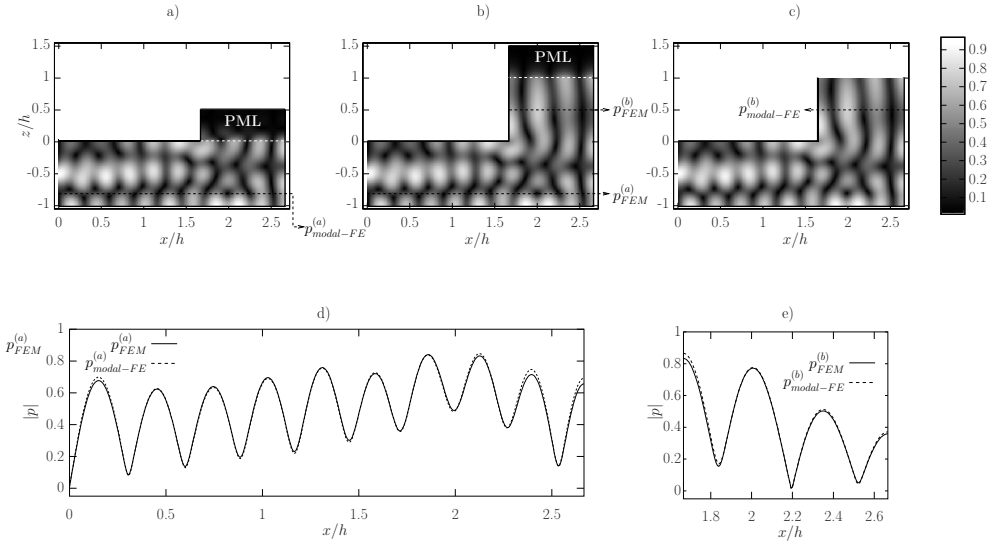


**Figure 1.8***: Modulus of the pressure in the L–shaped intersection. a) modal–FE result. b) Full FEM result. c) modal–FE result computing the field in the adjacent street with Eq* (1.52) *d) Pressure fields at* $z = -0.9$*. e) Pressure fields at* $z = 0.5$*.*

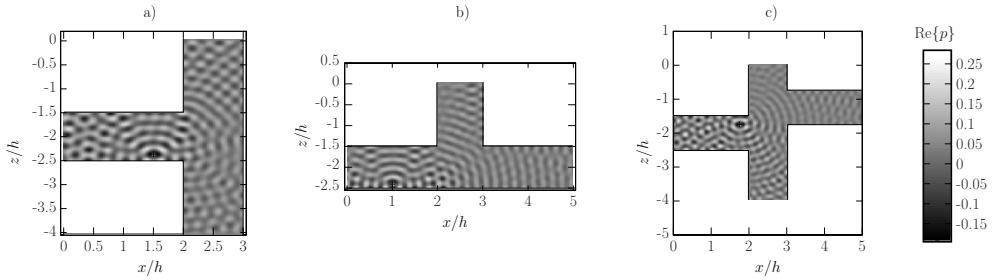


**Figure 1.9***: Real part of the pressure field in a),b) a T–shaped intersection and c) a cross intersection. The source position is indicated the symbols "+".*

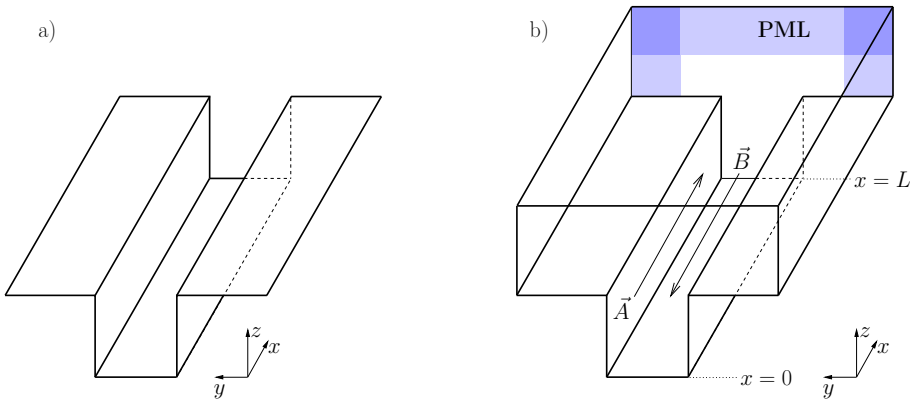


**Figure 1.10***: a) Geometry of the street canyon. b) Waveguide equivalent to the street canyon.*

## 1.2 Extension to 3D geometries

### 1.2.1 The uniform street canyon

Consider the urban canyon with uniform cross–section illustrated in Fig. 1.10a. As in the 2D geometry, PML's are inserted to transform the original open domain into an equivalent closed waveguide, see Fig. 1.10b. The PML is defined in this case by two coefficients: $\tau_y$ for waves traveling in the $y$–direction, and $\tau_z$ for waves traveling in the $z$–direction. These parameters are defined as piecewise constant functions of the space coordinates (see Fig. 1.11). They are defined as,

$$\tau_y(y) = \begin{cases} \tau_0, & \text{in lateral PML,} \\ 1, & \text{otherwise,} \end{cases} \tag{1.54}$$

and

$$\tau_z(z) = \begin{cases} \tau_0, & \text{in the top PML,} \\ 1, & \text{otherwise.} \end{cases} \tag{1.55}$$

The problem to solve in the equivalent waveguide is

$$\left( \frac{\partial^2}{\partial x^2} + \frac{1}{\tau_y} \frac{\partial}{\partial y} \left( \frac{1}{\tau_y} \frac{\partial}{\partial y} \right) + \frac{1}{\tau_z} \frac{\partial}{\partial z} \left( \frac{1}{\tau_z} \frac{\partial}{\partial z} \right) + k^2 \right) p(x, y, z) = 0, \tag{1.56}$$

The domain is meshed in the transverse coordinates $(y, z)$ using the FE method[1] (see Fig. 1.11b), and the field $p(x, y, z)$ is developed on the basis of interpolating functions

[1] In this case, the computation of the transverse problem is performed with the Matlab PDE Toolbox, using a Delunay triangular mesh with first order Legendre polynomials.

$\psi_n(y,z)$,

$$p(x,y,z) = \sum_n^N P_x(x)\psi_n(y,z) = {}^t\vec{\psi}\vec{P}(x) \tag{1.57}$$

with $P_n(x) = p(x, y_n, z_n)$. Therefore, the problem (1.56) takes the discrete form

$$\vec{P}''(x) + (k^2\mathbf{I} - \mathbf{M}^{-1}\mathbf{K})\vec{P}(x) = \vec{0},$$

where the mass matrix $\mathbf{M}$ and the stiffness matrix $\mathbf{K}$ are given by

$$M_{mn} = \int_\Omega \psi_m\psi_n \mathrm{d}y\mathrm{d}z, \tag{1.58}$$

with $\Omega = \Omega_p \cup \Omega_y \cup \Omega_z \cup \Omega_{y,z}$ the whole cross-section (see Fig. 1.11), and

$$\begin{aligned} K_{mn} = &\int_{\Omega_p} \frac{\partial\psi_m}{\partial y}\frac{\partial\psi_n}{\partial y} + \frac{\partial\psi_m}{\partial z}\frac{\partial\psi_n}{\partial z}\mathrm{d}y\mathrm{d}z + \int_{\Omega_y} \frac{1}{\tau_0^2}\frac{\partial\psi_m}{\partial y}\frac{\partial\psi_n}{\partial y} + \frac{\partial\psi_m}{\partial z}\frac{\partial\psi_n}{\partial z}\mathrm{d}y\mathrm{d}z + \\ &\int_{\Omega_z} \frac{\partial\psi_m}{\partial y}\frac{\partial\psi_n}{\partial y} + \frac{1}{\tau_0^2}\frac{\partial\psi_m}{\partial z}\frac{\partial\psi_n}{\partial z}\mathrm{d}y\mathrm{d}z + \int_{\Omega_{y,z}} \frac{1}{\tau_0^2}\frac{\partial\psi_m}{\partial y}\frac{\partial\psi_n}{\partial y} + \frac{1}{\tau_0^2}\frac{\partial\psi_m}{\partial z}\frac{\partial\psi_n}{\partial z}\mathrm{d}y\mathrm{d}z. \end{aligned} \tag{1.59}$$

The solution takes the same form as in the 2D case [Eq. (1.20)], with $\vec{\Phi}_n$ the eigenvectors and $\alpha_n^2$ the eigenvalues of the matrix $\mathbf{M}^{-1}\mathbf{K}$.

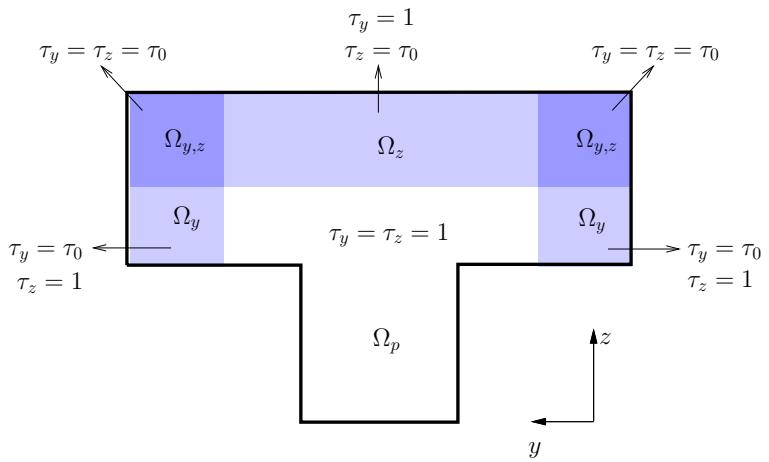


**Figure 1.11**: *Definition of the PML inserted in transverse section of the street canyon.*

### 1.2.2 Modelling of right–angled intersections

We illustrate the modal–FE method in 3D considering two configurations usually found in urban areas. The first one represents a street canyon with several perpendicular

intersecting streets, 1.12. The second one is a Π–intersection, consisting of two parallel streets intersected by a perpendicular one, 1.13.

Figs. 1.14 and 1.15 show the real part of the pressure field obtained with the Green's function formulation. The point source position is indicated with symbols "+". The output condition is the characteristic admittance $\mathbf{Y}_L = \mathbf{\Phi\Gamma\Phi}^{-1}$. The computation parameters are given in Tabs. 1.3 and 1.4. The figures show horizontal planes of the acoustic field at different heights. Notice the wave guiding within the buildings and the radiation into the atmosphere.

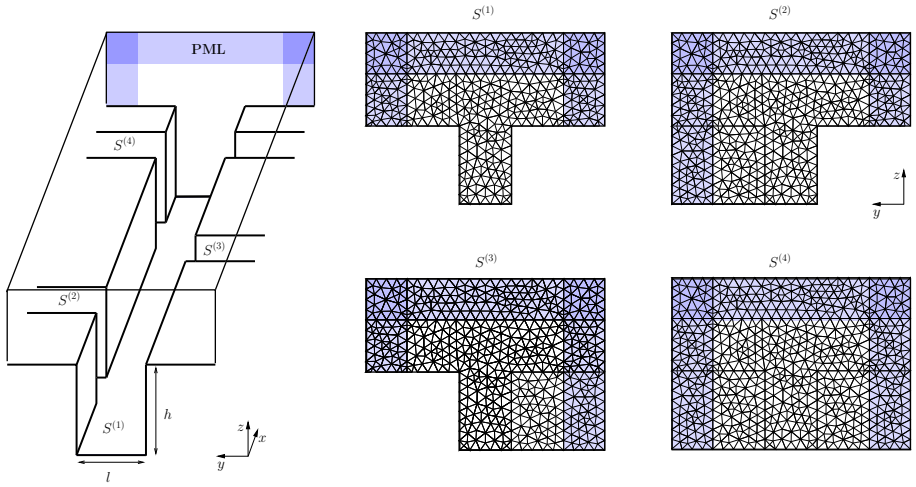


**Figure 1.12**: *Equivalent closed waveguide representing a street canyon with several right–angled intersections. Figures on the right show the meshes of the four different cross–sections, denoted by* $S^{(1)}, S^{(2)}$, $S^{(3)}$ *and* $S^{(4)}$.

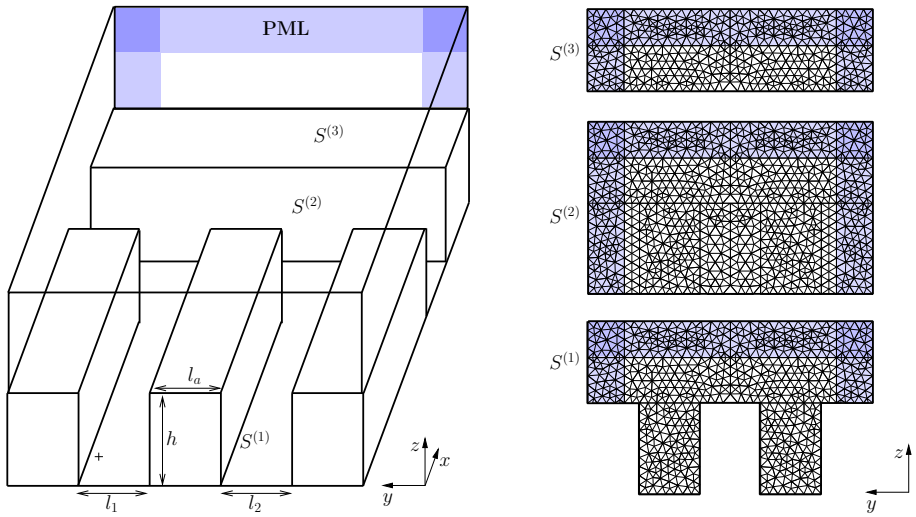


**Figure 1.13**: *Equivalent closed waveguide representing a* Π*-intersection. Figures on the right show the meshes of the three different cross–sections, denoted by* $S^{(1)}$, $S^{(2)}$ *and* $S^{(3)}$.

| **Right–angled intersections** | | | | | | | | | |
|---|---|---|---|---|---|---|---|---|---|
| Geometry | | Frequency | Meshes | | | | PML | | |
| $l$ | $h/l$ | $kl/2\pi$ | $S^{(1)}$ | $S^{(2)}$ | $S^{(3)}$ | $S^{(4)}$ | depth | $A$ | $\beta$ |
| 1 | 1.5 | 1.6 | 2403 | 3507 | 3513 | 4617 | $\lambda$ | $\sqrt{2}$ | $\pi/4$ |

**Table 1.3***: Computation parameters for the field shown in Fig. 1.14*

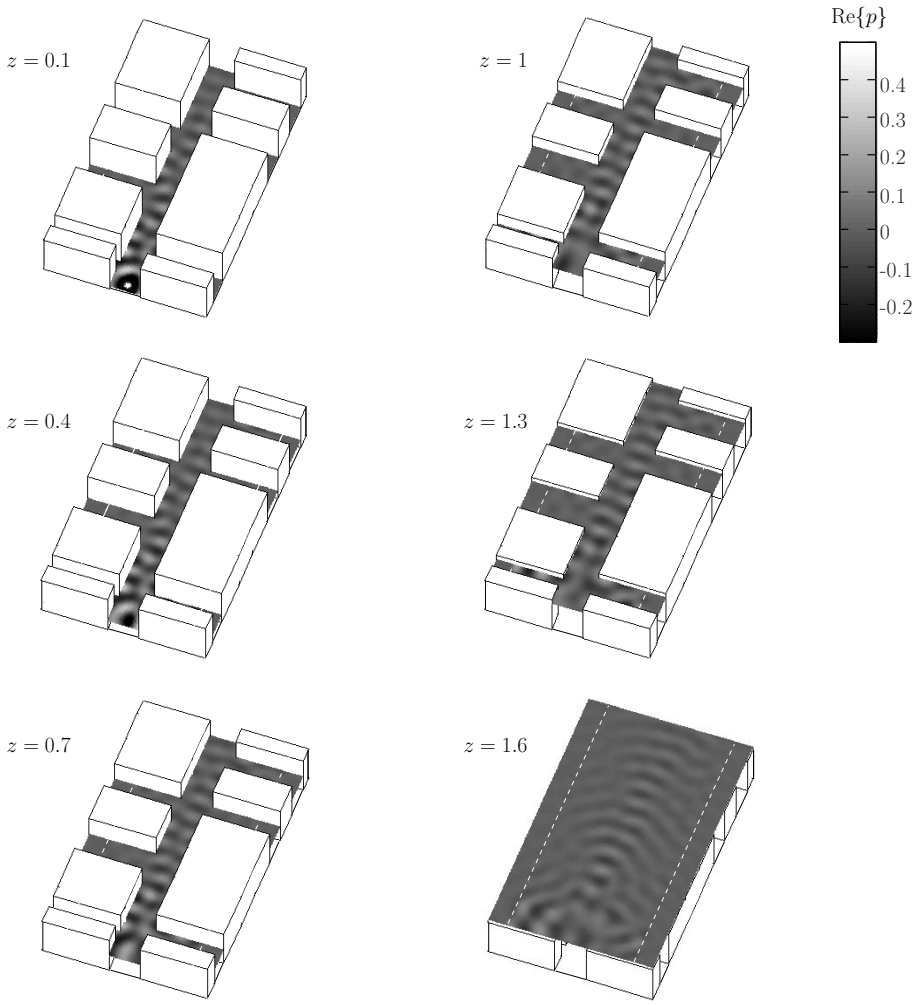


**Figure 1.14***: Real part of the pressure in a street with several right angled intersections.*

| Π-intersection | | | | | | | | | | | | |
|---|---|---|---|---|---|---|---|---|---|---|---|---|
| Geometry | | | | | | Frequency | Number of nodes | | | PML | | |
| $l_1$ | $\frac{l_2}{l_1}$ | $\frac{l_a}{l_1}$ | $\frac{h}{l_1}$ | $\frac{L_1}{l_1}$ | $\frac{L_2}{l_1}$ | $k \times l_1/2\pi$ | $S^{(1)}$ | $S^{(2)}$ | $S^{(3)}$ | width | $A$ | $\beta$ |
| 1 | 1 | 1 | 1 | 3.5 | 1.25 | 2.94 | 5103 | 3172 | 7361 | $\lambda$ | $\sqrt{2}$ | $\pi/4$ |

**Table 1.4***: Computation parameters for the field shown in Fig. 1.15. Distances are normalised to* $l_1$

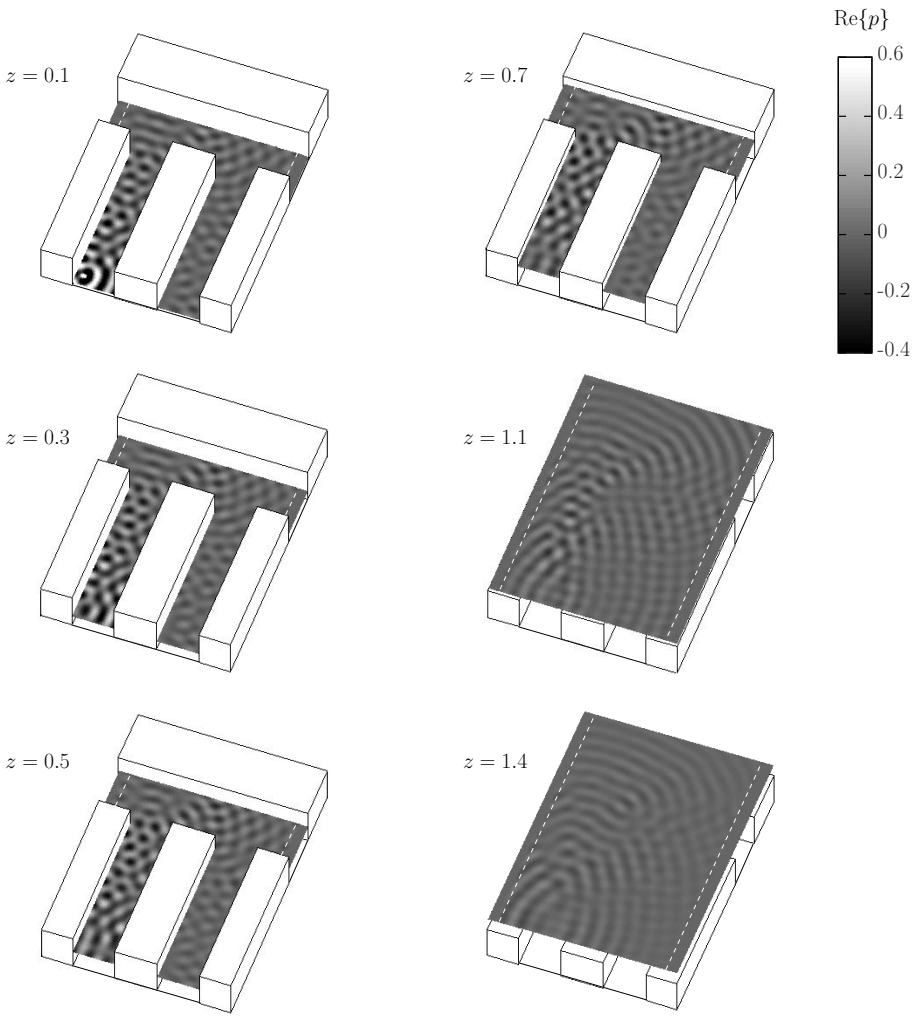


**Figure 1.15***: Real part of the pressure trough the* Π*–shaped intersection*

## 1.3 Summary

This chapter has introduced the modal–FE method and its application to the modeling of different kinds of right–angled intersections. Two formulations have been proposed: an initial value formulation, where the source takes the form of a known pressure field at the input waveguide section; and a Green's function formulation, enabling us to model point sources within the domain. The implementation of the method is divided in three main steps:

- The original, open geometry is substituted with an equivalent, closed waveguide.
- The transverse eigenmodes of the resulting waveguide are computed with FE and the general solution in each straight segment is expressed as a function of these eigenmodes [Eq. (1.20)].
- The modal amplitudes are calculated from the conditions at the waveguide extremities using the impedance matrix method (Sec. 1.1.4).

The modal–FE method can be implemented in any geometry convertible into a piecewise constant waveguide, regardless of the geometry and boundary conditions. Moreover, this approach provides information on the propagation and coupling of the different modes in the medium. This property is very useful in order to gain a fundamental understanding of the studied problems. In addition, since only the transverse section is meshed, the computational costs remain low compared to full–numerical methods. We will take advantage of these features to investigate wave propagation phenomena in the following Chapters.

# Appendix 1.A. Perfectly matched layers

A PML is an artificial absorbing layer used in numerical simulations to truncate an infinite propagation medium [8]. The feature that distinguish this layer from other absorbing boundary conditions is that waves incident upon the interface, coming from the physical domain, does not generate spurious reflections.

Consider a 1D Helmholtz problem defined in the spatial coordinate $y$,

$$\frac{\partial^2 p}{\partial_y^2} + k^2 p = 0. \tag{1.60}$$

The region of interest is $y \leqslant 0$, therefore a PML is introduced to truncate the domain, as shown in the Fig. 1.16a. The PML is defined by a complex coordinate stretching of the spatial coordinate $y$,

$$y \to \tilde{y} = \int_0^y \tau(y')dy', \tag{1.61}$$

where $\tau$ is a complex function such that

$$\tau = \begin{cases} 1, & \text{in the physical domain} \\ \tau_0, & \text{in the PML} , \end{cases} \tag{1.62}$$

where $\tau_0$ verifies $\mathrm{Re}\{\tau_0\} \times \mathrm{Im}\{\tau_0\} > 0$. In this work $\tau_0$ is chosen as constant in the PML region. Therefeore, equation (1.60) becomes

$$\frac{\partial^2 \tilde{p}}{\partial_{\tilde{y}}^2} + k^2 \tilde{p} = 0 \tag{1.63}$$

Then, given the coordinate stretching defined by Eq. 1.61, the operator $\frac{\partial}{\partial_{\tilde{y}}}$ can be substituted by $\frac{1}{\tau}\frac{\partial}{\partial_y}$, and the equation to solve becomes

$$\left(\frac{1}{\tau}\frac{\partial}{\partial_y}\left(\frac{1}{\tau}\frac{\partial}{\partial_y}\right) + k^2\right) p = 0. \tag{1.64}$$

In the physical domain, the solution to this equation for a wave propagating towards increasing $y$ is $p(y \leqslant 0) = A\exp(\jmath k y)$, which corresponds to the solution of the original problem. In the PML domain, the solution is $p(y > 0) = A\exp(\jmath k \tilde{y})$, which, given the imaginary part of $\tilde{y}$, corresponds to a wave with exponentially decreasing amplitude. On the other hand, since both solutions verifies the matching conditions $p(0^-) = p(0^+)$ and $\partial_y p(0^-) = \partial_y p(0^+)$, the incident wave is completely transmitted at the interface and absorbed in the PML region.

Theoretically, the thickness of the PML and its absorption can be chosen arbitrarily to vanish completely the incident field. In practice, due to discretisation, the continuity at the interface is not fulfilled exactly, which creates spurious reflections. This drawback

is minimised using a mesh sufficiently fine to describe correctly the exponential decay inside the PML. In this work, we found a satisfactory absorption meshing the PML with ten elements and imposing a PML thickness equal to one wavelength.

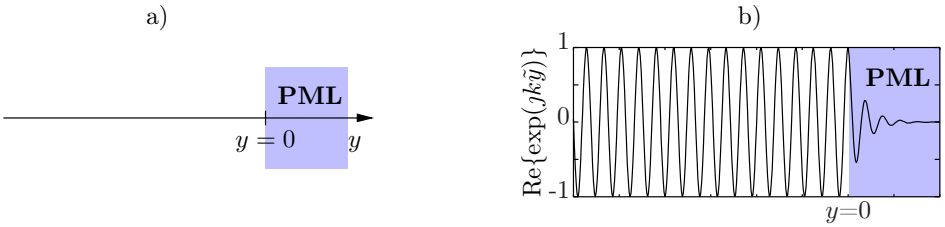


**Figure 1.16***: a) y–coordinate truncated by a PML at* $y = 0$*. b) The field in the PML is damped exponentially.*

# Chapter 2

# Resonance phenomena in urban courtyards

Courtyards are frequently found in the city centers of many French and European cities (Fig. 2.1 shows some examples). From an acoustical point of view, these enclosed spaces can be regarded as open cavities, which resonances can be excited by waves generated in the urban environment. The goal of this Chapter is to investigate resonance phenomena in these configurations.

This Chapter is based on an articile to be submitted to the *Journal of the Acoustical Society of America* [57].



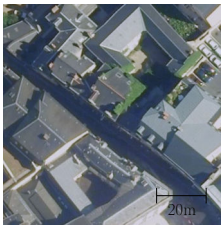



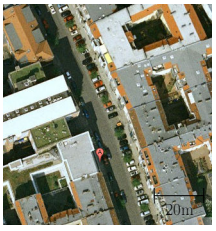



**Figure 2.1***: Typical courtyards considered in this Chapter. Images from left to right correspond to Boteros Street in Seville, Spain; Victor Bonhommet Street in Le Mans, France; and Novalis Street in Berlin, Germany.*

## 2.1 Introduction

Quiet urban areas are often identified as areas that are not directly exposed to traffic noise, as the inner yards found in the city centers [61]. However, studies have shown that inner yards can present considerably high noise levels [40]. This unexpected high levels of noise are partly generated by interior sources, but also by traffic noise reaching the courtyard, either above buildings or through façade openings.

Over the last years, authors have studied this problem in several ways. Frequently, the problem is simplified by a two-dimensional (2D) geometry, representing the transverse cross-section of two parallel canyons. [38, 40, 60, 83, 84] In such geometry, the source is placed in one of the canyons and the courtyard is represented by the other canyon. Authors have investigated in detail the influence of several parameters in noise shielding, as the roof shape, height-width ratio of the canyon, nature of façade surfaces [86], noise screens, source type or weather conditions. More recently, Hornikx and Forssén [41] investigated the sound propagation in 3D urban courtyards. Apart from the parameters mentioned above, this authors evaluated the effect of a façade opening, representing the entrance that connects the courtyard to the adjacent canyon. It was shown that the noise level inside the courtyard can be increased up to 10 dB(A) in the frequency band up to 500 Hz with respect to a courtyard without façade openings. Moreover, this work pointed out that a 3D model is necessary to predict correctly the sound level inside the courtyard; differences up to 4.4 dB(A) were found in the noise abatement estimation with respect to similar 2D configurations.

An additional factor that might increase the sound level inside the courtyard is the excitation of its acoustic resonances, particularly at low frequency. Such low frequency waves can be practically measured in urban environments as being produced by either heavy industrial machineries, intense impulse noise, or, for a part, the traffic noise [15, 62] and they may propagate on long distances, compared with higher frequency waves.

This work aims at investigating resonance phenomena in inner yards, both experimentally, using a scale model, and numerically, with the modal–FE method. From a fundamental point of view, the problem is that of a waveguide (the street) connected to a side resonator (the courtyard). This setup has been studied extensively in the literature, due to the intriguing physical phenomena that it exhibits. Fano resonances [35], localized modes [35, 81], negative bulk modulus [25] or nonlinear bandgap behavior [73] have been reported in waveguides connected to side resonators. The present work focuses on a distinctive characteristic of the 3D urban environment: the wave radiation above buildings, which enables the interaction between the waveguide and the resonator even when no direct connections exists between them. The scope of the present study is limited to the study of two practical aspects regarding urban acoustics applications, the amplification of the sound level inside the courtyard, and the attenuation of the acoustic field transmitted on the street due to the excitation of the courtyard resonances.

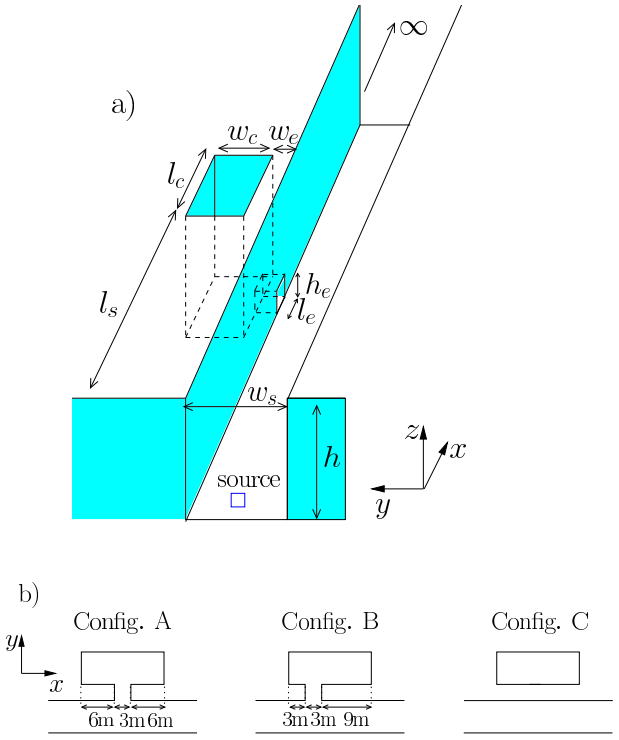


**Figure 2.2***: a) Geometry of the problem. b) Geometrical configurations. Config. A, centered entrance; Config. B, decentered entrance and Config. C, closed entrance.*

## 2.2 Geometry of the problem

Consider a courtyard adjacent to a urban canyon, as shown in Fig. 2.2(a). The courtyard is represented by the cavity with dimensions $(l_c \times w_c \times h)$. The street canyon has a rectangular cross–section $S = (w_s \times h)$ and it is considered as infinitely long in the $x-$direction. The courtyard and the street canyon are connected with the entrance defined by the small volume $(l_e \times w_e \times h_e)$. The source is placed in the street at the distance $l_s$ from the courtyard in the $x$–direction. The geometrical parameters are given in Table. 6.1.

The three geometrical configurations investigated are illustrated in Fig. 2.2(b). Configurations A and B correspond to a courtyard with centered entrance and decentered entrance, respectively. The comparison between Configs. A and B allows us to study the influence of the entrance position in the resonance phenomena. Config. C corresponds to a courtyard with closed entrance. The interest of Config. C is twofold. First, the comparison of Config. C with Configs. A and B allows us to evaluate the impact of the façade opening in the resonance phenomena. Secondly, it is relevant to investigate the

| | street canyon | | | courtyard | | entrance | | |
|---|---|---|---|---|---|---|---|---|
| parameter | $l_s$ | $w_s$ | $h$ | $l_c$ | $w_c$ | $l_e$ | $w_e$ | $h_e$ |
| full scale (meters) | 45 | 9 | 12 | 15 | 6 | 3 | 3 | 3 |
| 1:30 scale model (meters) | 1.5 | 0.3 | 0.4 | 0.5 | 0.2 | 0.1 | 0.1 | 0.1 |

**Table 2.1***: Geometrical parameters.*

behaviour of this geometry since the only possible interaction with the street is due to waves radiated above the roof level.

## 2.3 Experimental setup

The experimental setup consists on a 1:30 scale model, as shown in Fig. 2.3.a. Experiments are carried out in a semi-anechoic room with walls coated by a melamine foam that effective from 1 kHz onwards. The ground is made of a plexiglass plate. Buildings are made of plexiglass blocks with dimensions $(0.5 \times 0.3 \times 0.4)$ m. The entrance to the courtyard is built with 5 cm side varnished wooden cubes. An anechoic termination made of melamine dihedrals in inserted at the output to simulate the infinite extension of the canyon in the $x-$direction.

The sound source consists on a loudspeaker enclosed in a rigid box, connected to the canyon by a flanged rectangular duct with cross-section $S_s = (5 \times 5)$ cm, as shown in Fig. 2.3.b. The transverse field inside the duct should be assumed as constant up to 3.4 kHz, the cutoff frequency of the first mode of the cross-section $S_s$. In this work the frequency band is limited to 3 kHz, that corresponds to 100 Hz at full scale.

The acoustic pressure is measured using 1/4 in. microphones (B&K 4190), connected to a preamplifier (B&K 2669) and a conditioning amplifier (B&K Nexus 2669). For the measurements of insertion losses and transfer functions shown before in Sec. 2.5, the microphone is placed manually and the acquisition is performed using a SRS analyser model SR785. For the wave field maps, the microphone position is controlled by a 3D robotic system. The spatial step is fixed to 20 points per wavelength. The acquisition of the acoustic pressure is performed using an eInstrument-PC acquisition system from Innovative Integration. The sampling frequency is $f_e = 20f$ (20 samples per period) during a time length $T_e = N_e/f_e$, where $N_e = 2000$ (100 periods) is the number of samples. The RMS value of acoustic pressure is estimated by a least mean square method to determine the mean value, the amplitude and the phase of the signal.

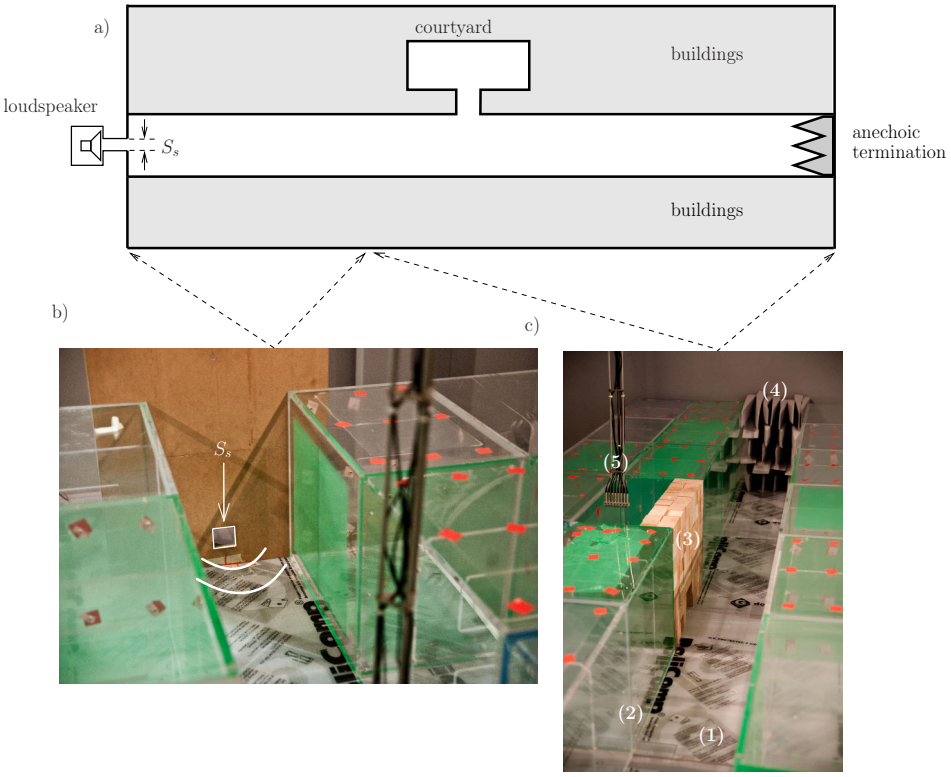


**Figure 2.3**: *a) Schematics of the experimental setup. b) The acoustic source is a loudspeaker enclosed in a rigid box, which is connected to the canyon through a flanged rectangular duct with cross-section $S_s = (5 \times 5)$ cm. c) (1) Ground made of a plexiglass plate (2) Buildings made of $50cm \times 30cm \times 40cm$ plexiglass blocks. (3) Entrance to the courtyard, built up using 5 cm side wooden cubes. (4) Anechoic termination. (5) Microphones*

## 2.4 Numerical model

The acoustic field in the equivalent waveguide represented in Fig. 2.4a is the solution to the following problem:

$$\begin{cases} \left[\dfrac{\partial^2}{\partial x^2} + \dfrac{1}{\tau}\left(\dfrac{\partial}{\partial y}\right)\dfrac{1}{\tau_y}\left(\dfrac{\partial}{\partial y}\right) + \dfrac{1}{\tau_z}\left(\dfrac{\partial}{\partial z}\right)\dfrac{1}{\tau_z}\left(\dfrac{\partial}{\partial z}\right) + k^2\right] p = & 0, \text{ in } \Omega \\ \partial_n p = & 0, \text{ on } \partial\Omega \end{cases} \tag{2.1}$$

where $\Omega$ is the domain and $\partial\Omega$ its boundaries. The PML parameters $\tau_y$ and $\tau_z$ have been defined in Sec. 1.2. The problem is meshed in the transverse coordinates $y$ and $z$ and the eigenmodes of each transverse cross-section are calculated using the FE (Fig. 2.4.b

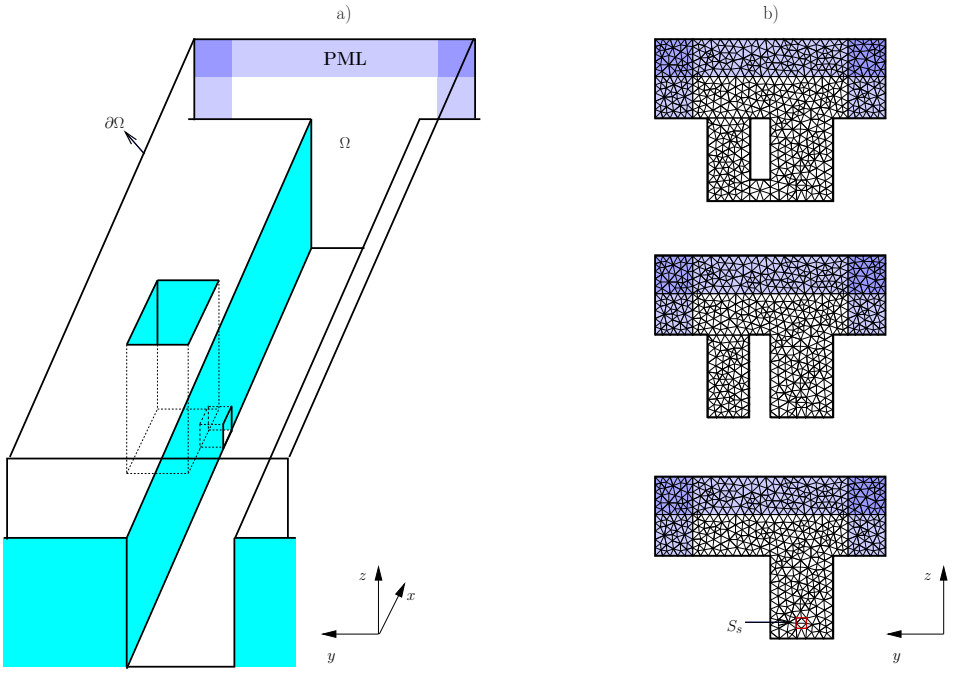


**Figure 2.4**: *a) Equivalent waveguide closed with PML. b) Exemples of FEM meshes of the three different cross sections.*

shows examples of meshes of the three different cross-sections of the guide). The solution in each different straight segment takes general form given in Eq. (1.20). The output condition is defined as a the characteristic admittance, $\mathbf{Y}_L = \mathbf{\Phi\Gamma\Phi}^{-1}$, and the admittance is calculated from the output section to the input the input cross-section using the procedure described in Sec. 1.1.4. Then, we compute the acoustic field in the domain from an input $\vec{P}_0$ following Eqs. (1.45)–(1.47).

In order to determine the input pressure field that corresponds to the experimental source, we define first the input condition as a normal derivative source condition $\vec{U}_0 = \partial_x \vec{P}_0$. From Fig. 2.3.b the components of $\vec{U}_0$ are,

$$U_{0,n} = \begin{cases} 1, \text{ if } (y_n, z_n) \in S_s \\ 0, \text{ elsewhere} \end{cases} \tag{2.2}$$

with $(y_n, z_n)$ the coordinates of the $n-$th node. The pressure source condition is the product of $\vec{U}_0$ and the input impedance, $\vec{P}_0 = \mathbf{Y}_0^{-1}\vec{U}_0$, where is the input $\mathbf{Y}_0$.

## 2.5 Results and discussion

The following expression [Eq. (2.3)] gives the resonance frequencies of the courtyard with a non-radiative condition $p = 0$ imposed on the upper part and ignoring the façade opening:

$$f_{(\mu_x,\mu_y,\mu_z)} = \frac{c_0}{2}\sqrt{\left(\frac{\mu_x}{l_c}\right)^2 + \left(\frac{\mu_y}{w_c}\right)^2 + \left(\frac{2\mu_z+1}{2h}\right)^2}, \tag{2.3}$$

where, $(\mu_x, \mu_y, \mu_z) \in \mathbb{N}^3$ are the number of nodal planes perpendicular to directions $x$, $y$ and $z$, respectively. Table 2.2 gives the first ten frequencies obtained with Eq. (2.3). They are approximated values of the actual resonance frequencies and will be used to identify the resonance peaks observed in the following study.

The spectrum of the transverse eigenmodes obtained by FE is shown in Fig. 2.5. The insets display the modulus of the pressure of some of the modes. The eigenmodes are denoted by the couple $(\nu_h, \nu_v)$, indicating the number of horizontal and vertical nodal lines, respectively. Due to wave radiation, the modes are attenuated during their propagation along the street and this attenuation is described by the imaginary part of the propagation constants, $\mathrm{Im}\{k_{x,(\nu_h,\nu_v)}\}$, $k_{x,(\nu_h,\nu_v)} = \sqrt{k^2 - \alpha^2_{(\nu_h,\nu_v)}}$. Like the classical modes in usual waveguides, the leaky modes in the canyon can be considered as being evanescent or propagating, depending on the frequency. We have checked that the modes $(0,0)$, $(0,1)$, $\cdots$, $(0,5)$, when propagating, are the least attenuated modes (see Appendix 2.A). Therefore these modes are supposed to provide the highest amount of energy. For this reason, and in order not to overload the discussion, the analysis will be based only on these modes.

### 2.5.1 Modal scattering

The behavior of the courtyard can be characterized by means of the modal scattering that it generates. Let $\vec{C}_I$ and $\vec{C}_R$ be the components of the incident and reflected fields, respectively. Then, the reflection matrix $\mathbf{R}$ is given by $\vec{C}_R = \mathbf{R}\vec{C}_I$. Fig. 2.6 shows the modulus of the diagonal terms of $\mathbf{R}$ corresponding to the modes $(0,0)$ to $(0,5)$. The

| $(\mu_x,\mu_y,\mu_z)$ | $f_{(\mu_x,\mu_y,\mu_z)}$(Hz) | $(\mu_x,\mu_y,\mu_z)$ | $f_{(\mu_x,\mu_y,\mu_z)}(Hz)$ |
|---|---|---|---|
| $(0,0,0)$ | 7.1 | $(0,0,1)$ | 29.2 |
| $(0,1,0)$ | 13.4 | $(1,2,0)$ | 31.1 |
| $(1,0,0)$ | 21.3 | $(0,1,1)$ | 31.3 |
| $(0,2,0)$ | 23.7 | $(0,3,0)$ | 34.7 |
| $(1,1,0)$ | 24.1 | $(2,0,0)$ | 35.4 |

**Table 2.2**: *First ten frequencies of resonance of the courtyard, estimated with Eq.* (2.3).

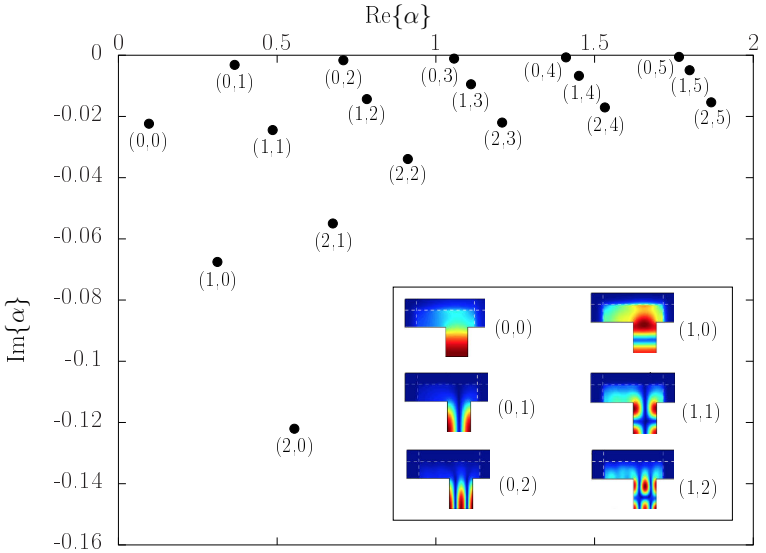


**Figure 2.5***: Spectrum of the complex eigenmodes of the transverse waveguide section. The insets display the modulus of some of the corresponding eigenmodes,* $|\vec{\Phi}_{(\nu_y,\nu_z)}|$.

vertical lines indicate the cutoff frequencies of these modes, given by $\mathrm{Re}\{f_{(\nu_y,\nu_z)}\}$ (see Fig. 2.6).

The graphs exhibit several resonance peaks due to the courtyard resonances. We corroborate this comparing the position of the peaks with the values in Table 2.2. The first peak at $f = 6.3$ Hz corresponds to the fundamental resonance of the courtyard $f_{(0,0,0)} = 7.1$ Hz. The second peak at $f = 13$ Hz corresponds to the first higher order resonance $f_{(0,1,0)} = 13.4$ Hz. Other resonances can also be identified in the band $20 - 40$ Hz as $f_{(0,2,0)} = 23.7$ Hz, $f_{(0,1,1)} = 31.3$ Hz and $f_{(0,3,0)} = 34.7$ Hz. Note that the frequencies observed in the graphs are slightly lower than those estimated by Eq. (2.3) because of the radiation losses above the courtyard, which are neglected by Eq. (2.3).

The curves of Fig. 2.6 reveal several important characteristics. One is that the courtyard is very sensitive to the presence of a façade opening. In Configs. A and B (with façade opening) several peaks appear in the reflection coefficients of all modes. The differences between Configs. A and B are explained by the proximity of the entrance to a given nodal plane (this will be discussed in the following sections). In Config. C (without façade opening) the courtyard has a significant effect only for the fundamental mode $(0, 0)$, and a very weak scattering is observed for higher order modes.

It is also remarkable that the first peak, corresponding to the fundamental resonance, has a similar amplitude in all cases. This indicates that this resonance is mainly excited by waves propagating above the roof level, being much less sensitive to the presence of a façade opening. Another important feature is that, given an incident mode, the

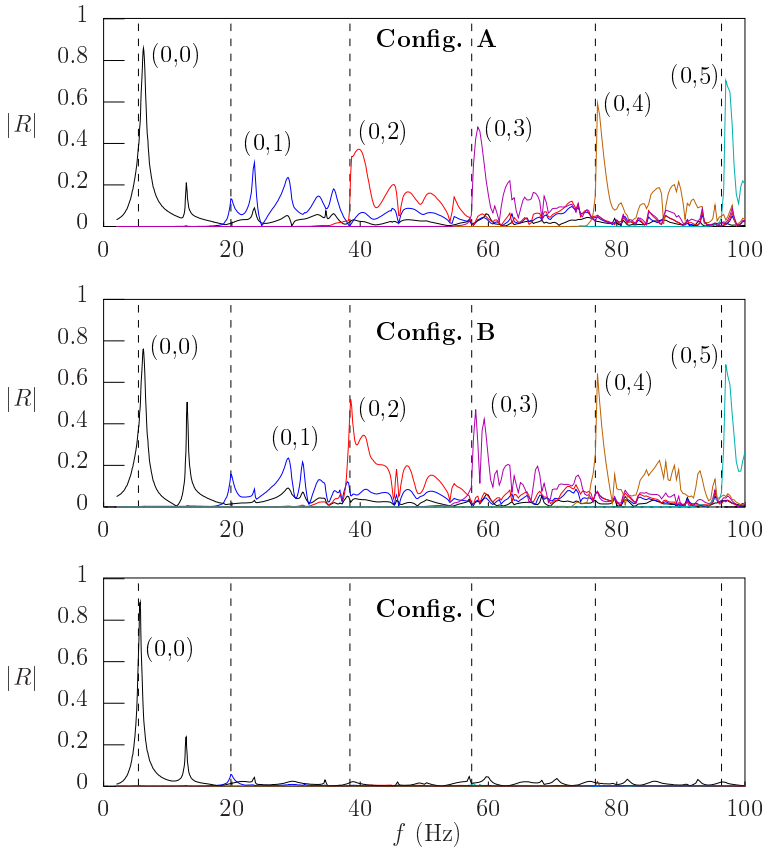


**Figure 2.6**: *(color online) Modulus of the diagonal terms of the reflection matrix* **R** *corresponding to modes* $(0,0)$ *to* $(0,5)$*, obtained in each geometrical configuration. The vertical lines represent the cutoff frequencies of these modes.*

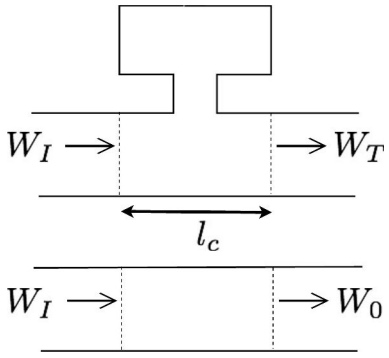


**Figure 2.7**: *The insertion loss is computed as* $A_c = 10\log_{10}(W_0/W_T)$*, where* $W_T$ *is the energy flux with the courtyard and* $W_0$ *is the energy flux transmitted through a uniform segment of urban canyon with length* $l_c$*.*

modal scattering mainly occurs at resonances close to the cutoff frequency of the mode. Note that the reflection peaks with highest amplitude are comprised between the cutoff of the mode and the cutoff of the next mode. This indicates that the behavior of the courtyard is strongly linked to the modal content of the incident field.

### 2.5.2 Insertion Loss

In order to evaluate the attenuation of the acoustic field in the urban canyon due to resonances we calculate the insertion loss, $A_c$. The energy flux is given by

$$W = \frac{1}{2S}\int\int_S \mathrm{Im}\{p^*\partial_x p\}\,\mathrm{d}y\,\mathrm{d}z, \tag{2.4}$$

where "$*$" denotes the conjugate. Since the street canyon also induces attenuation due to radiative losses, the ratio of the incident flux $W_I$ to the transmitted flux $W_T$ is not enough to determine the attenuation due to the courtyard resonances (see Fig. 2.7). Indeed, the attenuation created by the courtyard alone is computed as

$$A_c = 10\log_{10}\left(\frac{W_I/W_T}{W_I/W_0}\right) = 10\log_{10}\left(\frac{W_0}{W_T}\right), \tag{2.5}$$

where $W_0$ is the energy flux computed without the courtyard at a distance $l_c$ (see Fig. 2.7). Details on the computation of $W_T$ and $W_0$ are given in Appendix 2.B.

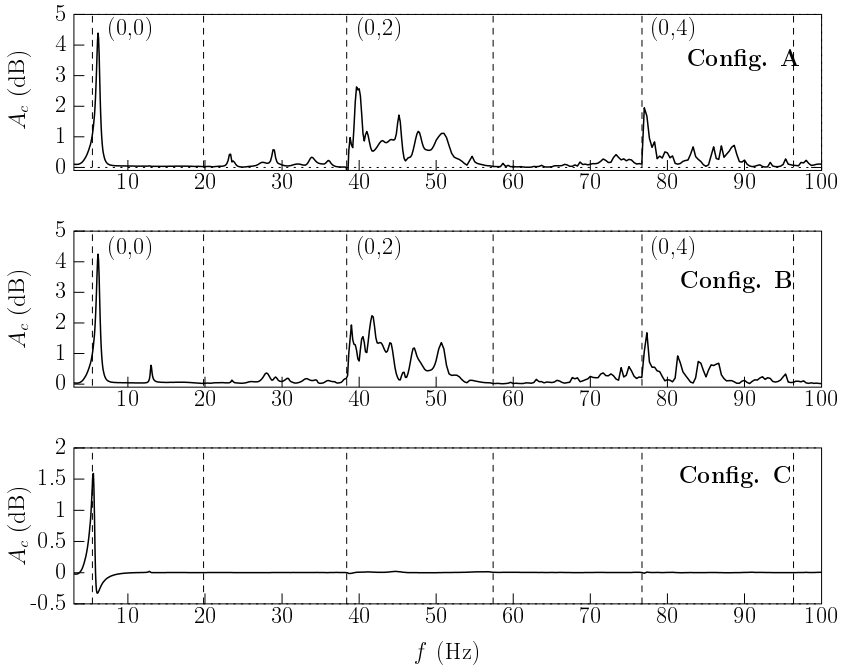


**Figure 2.8***: Insertion loss considering a coherent incident field.*

### Coherent incident field

Let us consider first a coherent incident field generated by the source described in Secs. III and IV. The corresponding attenuation curve is given in Fig. 2.8. In Configs. A and B it can be observed that the attenuation peaks appear close to the cutoff frequencies of modes $(0,0)$, $(0,2)$ and $(0,4)$, that are the only modes excited by the source in theory. The attenuation is around 4 dB at the fundamental resonance and oscillate between 1 and 2 dB at the other ones. In Config. C a single attenuation peak with amplitude 1.5 dB is observed at the fundamental resonance.

Unfortunately it is difficult to obtain an experimental equivalent of $A_c$, since it would require the measurement of the pressure field in the whole section $S$ as a function of frequency, which would require a lot of time. Instead, a measurement at a single point can be sufficient to give an experimental evidence of the phenomena described before. For this, the microphone is placed in the waveguide, downstream from the courtyard position, near the ground. The measured attenuation $A_{\text{meas}}$ is then given by $A_{\text{meas}} = 20\log_{10}(|p_0/p_T|^2)$, where $p_0$ is the pressure without the courtyard and $p_T$ is the pressure with the courtyard.

Fig. 2.10a shows $A_{(meas)}$ obtained in Config. A. The main attenuation peaks are generated close to the cutoff frequencies of the transverse modes of the street, that

is in good qualitative agreement with the numerical predictions (Fig. 2.8). In order to visualize the effect of attenuation, the wave field at some relevant frequencies have been measured and compared to the numerical fields. The left (resp. right) column of Fig. 2.10b shows horizontal planes of the measured (resp. numerical) fields at $f = 6.3$ Hz and $f = 39.6$ Hz, where a strong attenuation of the field is observed. The fields have been obtained at height 1.5 m. The mitigation of the acoustic field along the canyon is obvious. At $f = 39.6$ Hz an attenuation of about 15 dB is found in both the numerical and the experimental fields. At $f = 6.3$ Hz, the attenuation is about 10 dB in the experimental field and 15 dB in the numerical field. The cause of this discrepancy is probably the limited absorption of the room and the anechoic termination at such low frequencies (note that the frequency range corresponds to $f < 1050$ Hz at real scale).

### Incoherent incident field

It is also interesting to study the attenuation due to the courtyard in the case of an incident field. Such a field can be found in urban areas as generated by a big number of uncorrelated sources. If $\vec{P}_I = \mathbf{\Phi}\vec{C}_I$ is the incident field, and $m$ and $n$ indicates the $m-$th and $n-$th node of the mesh in the transverse plane, the definition of an incoherent incident field implies the following condition on $\vec{P}_I$:

$$< P^*_{I,m}, P_{I,n} >= \delta_{m,n}, \tag{2.6}$$

where $\delta_{m,n}$ is the Kronecker symbol, and a unitary amplitude has been assumed ($|P_{I,n}| = 1$). Introducing Eq. (2.6) in the computation of the energy flux (see Appendix A) allows us to compute the attenuation when a diffuse incident field is considered.

From the point of view of the modes propagating in the street, a diffuse field can be defined as the superposition of a large number of incoming modes with the same amplitude and random phase. Then, the attenuation in the incoherent case can be regarded as the averaged attenuation obtained when a large number of realizations is done, with a single incident mode in each realization. The results in this case should differ noticeably from the case of the coherent incident field. In particular, the attenuation is expected to be lower and the concentration of attenuation peaks around the cutoff frequencies should disappear.

The attenuation curves obtained in this case are shown in Fig. 2.9. As expected, the modal behavior observed previously in the coherent case (Fig. 2.8) has disappeared and the attenuation peaks are more uniformly distributed along the frequency range. Also, the absorption peaks have a smaller amplitude. Only the first peak is similar to that obtained with a coherent source The reason is that at such low frequencies, the single propagative mode in the street canyon is the mode $(0, 0)$. Therefore the concept of incoherent incident field is meaningless. Indeed, whatever the modal content of the incident field at these low frequencies, after a short propagation distance the transverse field in the canyon will be dominated by the mode (0,0). Thus, the attenuation obtained should depend weakly on the type of incident field.

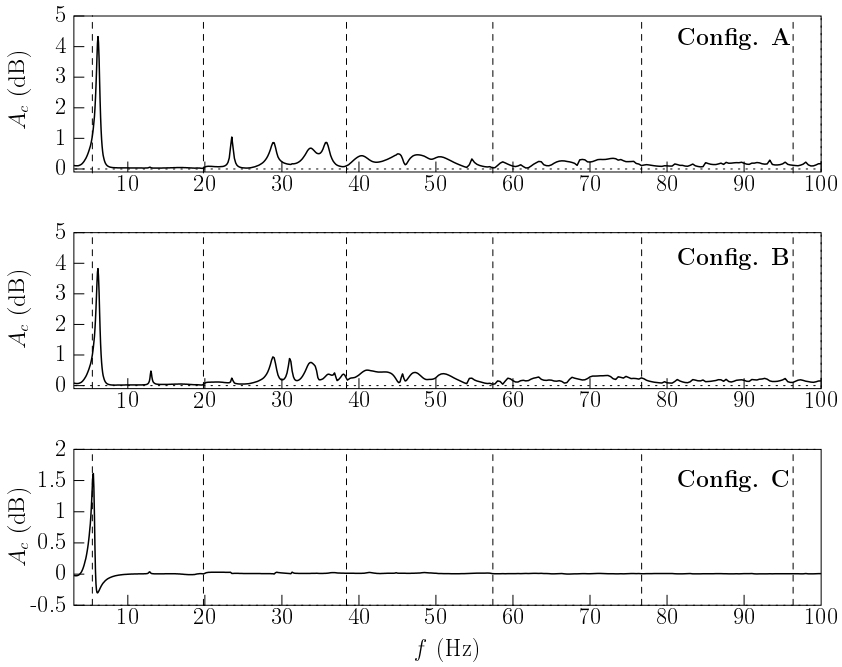


**Figure 2.9***: Insertion loss considering an incoherent incident field.*

### 2.5.3 Amplification of the sound level inside the courtyard

Inspecting the pressure field at the courtyard resonances, it is observed that the sound level inside the courtyard is similar or even higher than the sound level in the street [Fig. 2.10(b)]. This is in contradiction with the noise shielding effect that is usually expected in these configurations. To evaluate more precisely the sound amplification inside the courtyard, the transfer function $H = p_c/p_s$ between the pressure at a point inside the courtyard $p_c$ and a point close to the source $p_s$ (cf. Fig. 2.3) has been measured and compared with the numerical model. The point inside the courtyard is appropriately chosen close to a corner, since it represents a maximum of pressure for any of the courtyard resonances. Thus, an increase of the sound level generated by a resonance should be detected by this measurement.

Fig. 2.11 shows the amplitude in dB of the measured and the predicted transfer functions. Insets in Fig. 2.11 show the field inside the courtyard in the horizontal plane at a given resonance, computed with the modal-FE method. At low frequencies ($f < 40$ Hz) curves show well differentiated peaks with amplitudes around $10 - 15$ dB. From 40 Hz onwards, it is difficult to identify other resonances because of the high modal overlapping.

A good agreement is observed between experimental and numerical results. How-

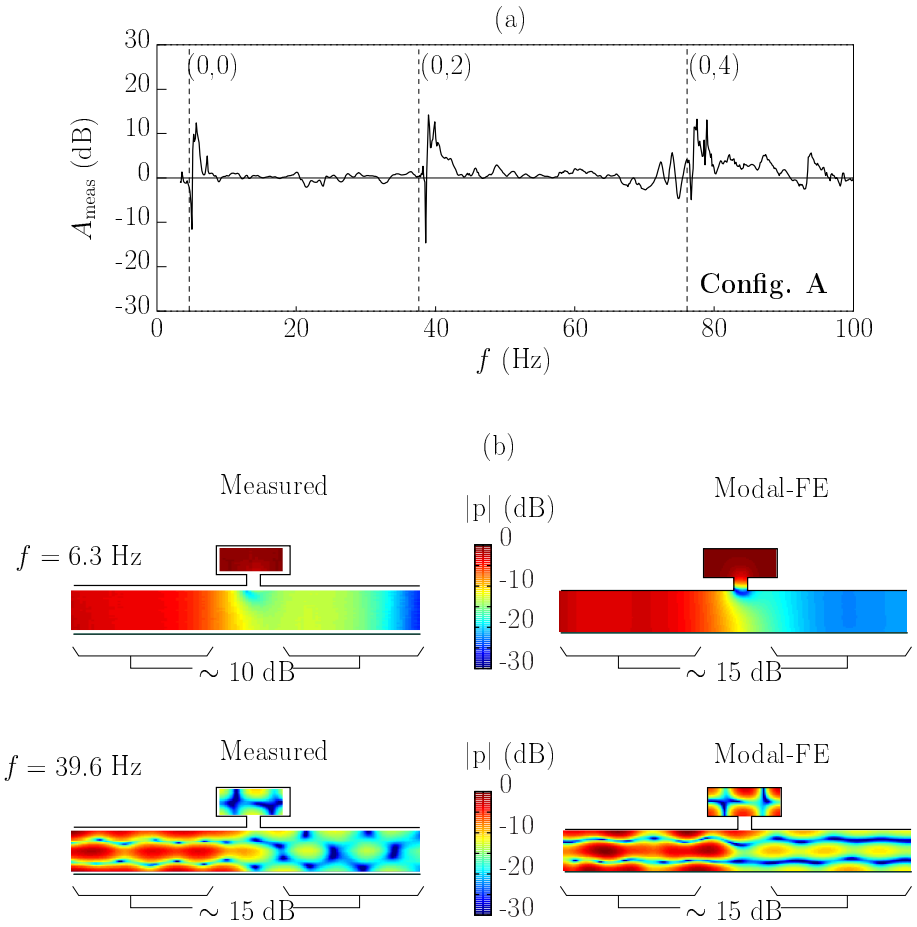


**Figure 2.10**: *(a) Measured attenuation $A_{meas}$ obtained in Config. A. (b) Amplitude in dB of the pressure field in the horizontal plane at frequencies $f = 6.3$ Hz and $f = 39.6$ Hz, obtained in configuration A in source position I. Fields have been measured at height 5 cm (1.5 m at full scale). Images on the left display measured fields, while images on the right display fields calculated with the modal-FE method.*

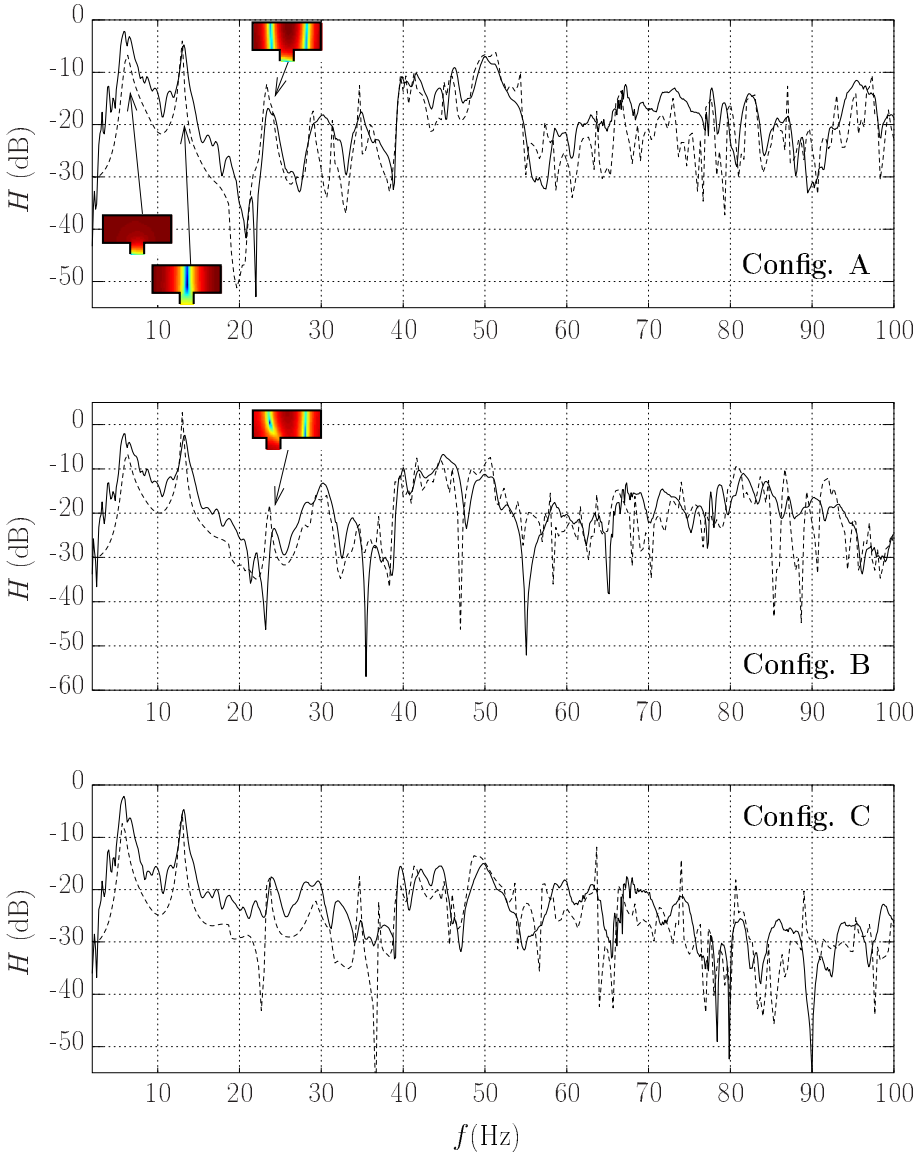


**Figure 2.11**: *Measured (solid lines) and predicted (dashed lines) amplitude of the transfer functions in dB. The insets represent the pressure field inside the courtyard at a given resonance.*

ever, the amplitude of the measured transfer functions are about 5 dB higher than the predicted ones in the band $f < 35$ Hz. Again this discrepancy is certainly due to the already mentioned difficulty of absorbing such low frequencies by the room and the anechoic termination. Also, it is observed that resonance peaks are more damped in the experimental case (see, *e.g.*, the first three modes mentioned by the arrows, at $\sim 6.3$, 13 and 23.6 Hz: the peaks are larger in the experimental results). The reason is that the only damping mechanism in the numerical model is the wave radiation above the courtyard, while in the experimental device other inherent damping phenomena exist, as viscous and thermal losses or a finite impedance of wood.

As it has been observed in the modal reflection coefficients (Fig. 2.6) the position of the façade opening modifies the behavior of the courtyard. This is explained by the proximity of the entrance to the nodal lines of a given resonance mode (see the insets in Fig. 2.11). The most evident example is the peak at $f = 23.6$ Hz (mode $(0, 2, 0)$), which amplitude is more than 5 dB higher in Config. A than in Config. B. The amplitude of the second resonance peak at $f = 13$ Hz is slightly higher in Config. B than in Config. A for a similar reasons.

Regarding the curve of Config. C, a relevant point is the strong excitation of the first two resonant modes. Note that their amplitude is similar to configurations A or B and indicate that the sound level inside the courtyard is only a few decibels lower than the source level (0 dB), which is located 45m away. Note also that this confirms the result predicted previously in Sec. 2.5.1: the excitation of the fundamental resonance is done mainly by waves propagating above the buildings to reach the courtyard. With increasing frequency the resonant behavior is much less pronounced and a decay of the transfer function is observed. This agrees also with the corresponding curve of Fig. 2.6, that shows a weak excitation of the courtyard resonances from 20 Hz onwards.

## 2.6 Conclusion

We have investigated numerically and experimentally acoustic resonances in urban courtyards. Numerical and experimental results are in good agreement and show a strong resonant behaviour of these configurations. As a result of the resonances, the sound level inside the courtyard increases considerably, which generates in turn an important reduction of the acoustic field on the street. Remarkably, the sound level inside the courtyard at resonance is comparable to the sound level in the street. On the other hand, the strong interaction between the courtyard resonances and the acoustic field on the street suggests the use of these configurations to control the propagation of low and very low frequency waves in urban environments, which are difficult to be controlled otherwise.

# Appendix 2.A. The least damped modes of the street

In order to determine the least damped modes on the street we have computed the imaginary part of the propagation constants as a function of frequency and aspect ratio $r = h/w$, with $h$ and $w$ being the height and width of the street. Figure 2.12 show $\mathrm{Im}\{k_{x,(\nu_h,\nu_v)}\}$ versus frequency for $r = 1$, $r = 3$, and $r = 5$. Regardless of the aspect ratio, the least damped mode is the always the mode (0,0) for frequencies below the cutoff frequencies of the family $(0, \nu_v)$. After their respective cutoff frequencies, the family $(0, \nu_v)$ become the least damped modes. The family $(1, \nu_v)$ is always more attenuated than the family $(0, \nu_v)$. Indeed, as a general rule, the attenuation of a given mode $(\nu_h, \nu_v)$ increases as $\nu_h$ increases. Physically, we explain this from the fact that the mode becomes more and more directed in the vertical direction as $\nu_h$ increases, which facilitates the energy radiation.

# Appendix 2.B. Computation of the energy flux

In the modal–FE method, the pressure $p$ and its $x-$derivative $\partial_x p$ are developed on the basis of the interpolating polynomials $\psi_n(y, z)$,

$$p = \sum_{m=1}^{N} P_m \psi_m = {}^t\vec{\psi}\vec{P}, \tag{2.7}$$

$$\partial_x p = \sum_{n=1}^{N} U_n \psi_n = {}^t\vec{\psi}\vec{U}. \tag{2.8}$$

For an incident field $p = p_I$, the solution takes the form

$$\vec{P}_I = \mathbf{\Phi}\vec{C}_I \tag{2.9}$$

$$\vec{U}_I = \mathbf{Y}_c\vec{P}_I \tag{2.10}$$

with $\mathbf{Y}_c = \mathbf{\Phi\Gamma\Phi}^{-1}$ the characteristic impedance matrix of the guide, and $\mathbf{\Gamma}$ a diagonal matrix such that $\Gamma_{nn} = \jmath k_{x,n}$. On the other hand, the incident energy flux across the section $S_1$ of the guide is defined as

$$W_I = \frac{1}{2S_1}\int\int_{S_1} \mathrm{Im}\{p_I^*\partial_x p_I\}\,\mathrm{d}y\,\mathrm{d}z. \tag{2.11}$$

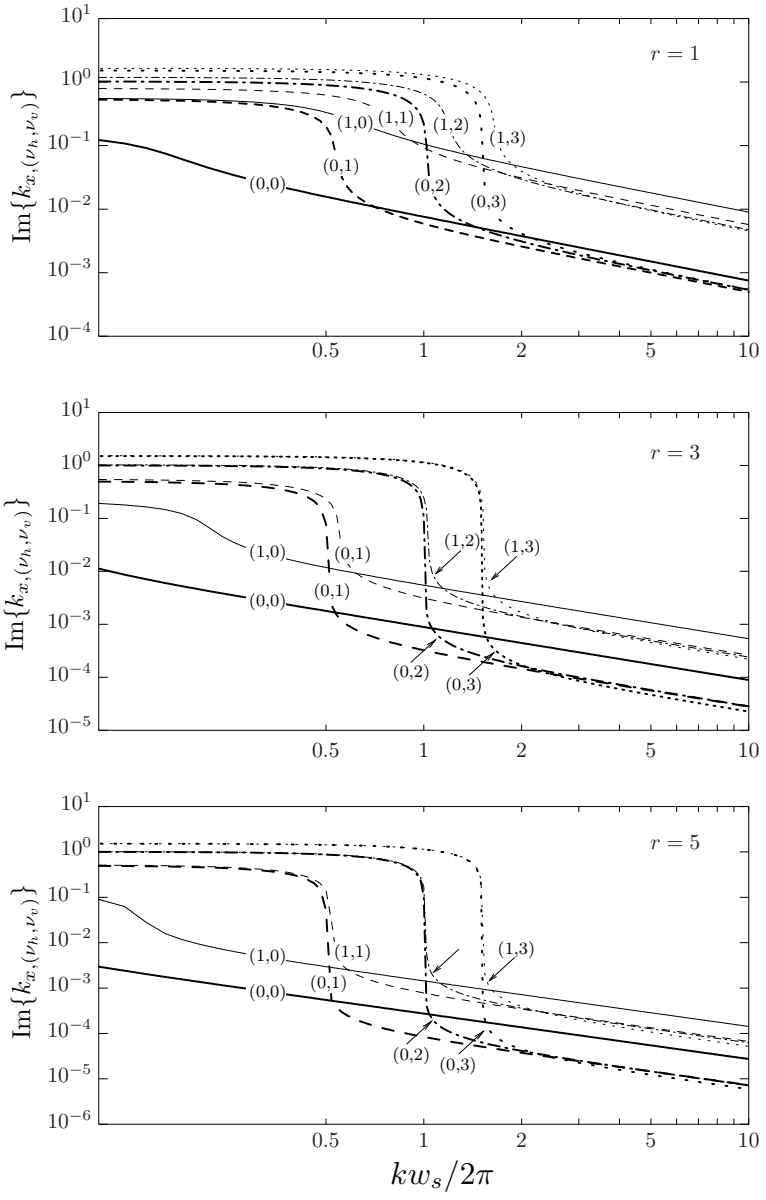


**Figure 2.12**: *Im*$\{k_{x,(\nu_h,\nu_v)}\}$ *versus frequency for* $r = 1$ *(top panel),* $r = 3$ *(center panel), and* $r = 5$ *(bottom panel)*

Introducing Eqs. (2.9) and (2.10) into Eq. (2.11) one obtains

$$\begin{aligned} W_I &= \frac{1}{2S_1}\sum_m^N\sum_n^N \mathrm{Im}\left\{P^*_{i,m}U_{i,n}\int\int_{S_1}\psi_m\psi_n \mathrm{d}y\mathrm{d}z\right\} \\ &= \frac{1}{2S_1}\mathrm{Im}\left\{{}^t\vec{P}^*_I\mathbf{G}\mathbf{Y}_c\vec{P}_I\right\}, \end{aligned} \tag{2.12}$$

where $\mathbf{G} = \int\int_{S_1}\psi_m\psi_n \mathrm{d}y\mathrm{d}z$. Similarly, if $\vec{P}_T = \mathbf{T}_n\vec{P}_I$ is the transmitted field, with $\mathbf{T}_n$ the nodal transmission matrix, the transmitted energy flux is given by

$$W_T = \frac{1}{2S_1}\mathrm{Im}\left\{{}^t\vec{P}^{*t}_I\mathbf{T}^*_n\mathbf{G}\mathbf{Y}_c\mathbf{T}_n\vec{P}_I\right\}. \tag{2.13}$$

The energy flux $W_0$ in the absence of the courtyard has the same form, with $\mathbf{T}_n$ the transmission matrix calculated in the absence of the courtyard (it thus simply describe the damping of the leaky waveguide mode while propagating).

In the case of a diffuse incident field such that $< P^*_{I,m}, P_{I,n} >= \delta_{m,n}$, one obtains $W_T = \mathrm{Im}\left\{\mathrm{tr}\left({}^t\mathbf{T}^*_n\mathbf{G}\mathbf{Y}_c\mathbf{T}_n\right)\right\}$, where tr denotes the trace.

The energy flux across the section $S$ of the street is obtained replacing $S_1$ with $S$ in Eqs. (2.11)–(2.13) and reducing vectors and matrices to the that nodes located inside the section $S$.

# Chapter 3

# Multimodal approach of the acoustic propagation in periodic media

## 3.1 Introduction

For decades, wave propagation in periodic media has fascinated scientists from different fields and has motivated intensive research. In the late 80s, Yablanovitch and John [46, 93] proved simultaneously that a transparent material with periodically modulated dielectric properties could avoid the transmission of light at certain frequencies. Such materials were called photonic band gap materials (or photonic crystals), in analogy to the energy gaps firstly observed in crystalline atomic arrangements [12]. Several years later, a similar phenomenon was observed for acoustic waves, giving rise to phononic crystals (Martínez-Sala *et al.* [55]). Related to the periodicity, other unique phenomena are also found in periodic media, as strong dispersion or negative refraction [45, 54]. Since their discovery, the interest in phononic crystals has increased enormously, due to their fundamental interest and also to their application in many areas of science and technology (as filtering, wave guiding or superlensing). For an overview of the historical development and recent advances on this field, the reader can refer to [75].

In this dissertation, two Chapters are concerned with the wave propagation in periodic media: Chapter 4, which investigates the formation of bandgaps in periodic urban areas; and Chapter 6, which studies the unconventional acoustic response of metasurfaces. Before addressing these challenging studies, the goal of the present Chapter is to introduce the basic principles of wave propagation in periodic media.

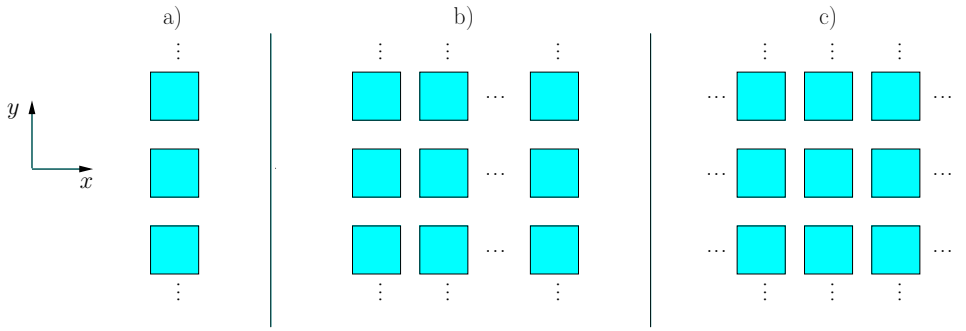


**Figure 3.1**: *Geometries under consideration: a) system composed by a single periodic row along y, b) system composed by a series of periodic rows along y, c) periodic system along x and y.*

We considered 2D systems composed of periodic arrangements of rectangular scatterers, Fig. 3.1. Since the modal basis of the transverse sections of these systems can be obtained analytically, a classical multimodal formulation [64] is used.

## 3.2 System composed of a single row

Consider the geometry represented by the Fig 3.2. It consists on a single infinite periodic row of rectangular rigid scatterers disposed along the $y-$direction. $L_b$ and $h_b$ denotes respectively the length and the height of the scatterers $L_a$ is the length of the periodic free space on both sides of the row, $h_a$ is the gap between two consecutive scatterers, and $D_y$ is the period.

When the system is excited with a harmonic plane, the Bloch–Floquet theorem [12] imposes the following condition on the pressure field,

$$p(x, y + nD_y) = \mathrm{e}^{\jmath n k_y D_y} p(x, y), \tag{3.1}$$

with $n \in \mathbb{Z}$, $k_y = k \sin(\theta)$, and $\theta$ the incidence angle with respect to $x$. This condition indicates that the acoustic field in the media is also periodic with period $D_y$, meaning that the propagation domain can be entirely represented from a single unit cell (Fig. 3.2).

The unit cell is composed of two regions denoted with superscripts $(I)$ and $(II)$. In the region $(I)$, the pressure field is developed on the basis of plane waves $\phi_n^{(I)}(y)$ defined by the Bloch–Floquet condition [Eq. (3.1)],

$$\phi_n^{(I)}(y) = \frac{1}{\sqrt{D_y}} \mathrm{e}^{\jmath \beta_n y}, \tag{3.2}$$

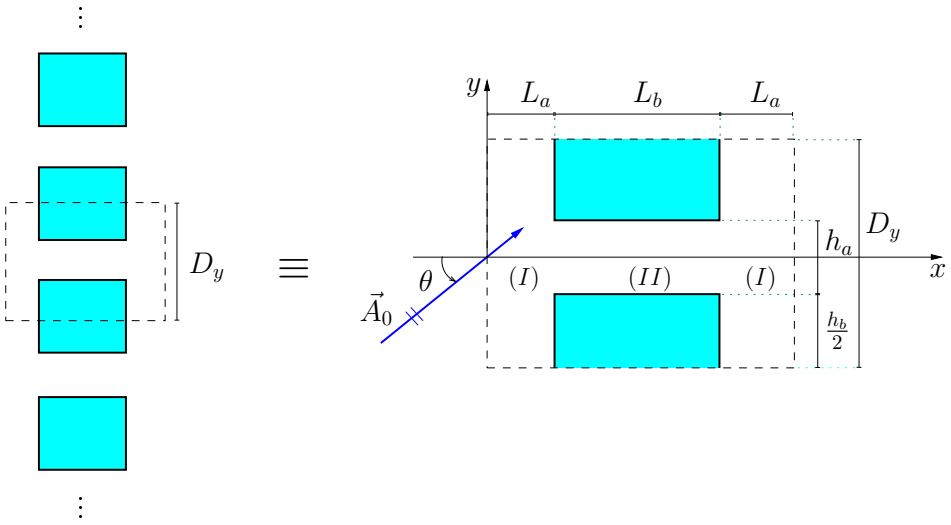


**Figure 3.2***: Left, a system composed by a single periodic row along y. Right, unit cell of the row.*

where $\beta_n$ are the Bloch wavenumbers in the $y-$direction,

$$\beta_n = k_y + \frac{2\pi n}{D_y}. \tag{3.3}$$

The pressure field in region $(I)$ takes then form

$$p^{(I)}(x,y) = \sum_{n=-\infty}^{\infty} \phi_n^{(I)}(y) \left( A_n^{(I)} \mathrm{e}^{\jmath k_n^{(I)} x} + B_n^{(I)} \mathrm{e}^{-\jmath k_n^{(I)} x} \right), \tag{3.4}$$

with $k_n^{(I)} = \sqrt{k^2 - \beta_n^2}$ the wavenumbers in the $x-$direction. In region $(II)$, the pressure field is developed on the basis of the transverse eigenfunctions (cosine functions in this case):

$$p^{(II)}(x,y) = \sum_{m=0}^{\infty} \left( A_m^{(II)} \mathrm{e}^{\jmath k_{x_m}^{(II)} x} + B_m \mathrm{e}^{-\jmath k_{x_m}^{(II)} x} \right) \phi_m^{(II)}(y), \tag{3.5}$$

with

$$\phi_m^{(II)}(y) = \sqrt{\frac{1+\delta_{m0}}{h_a}} \cos\left[ \frac{m\pi}{h_a} \left( y - \frac{h_a}{2} \right) \right],$$

where $\delta$ is the Kronecker symbol and $k_{x,m}^{(I)} = \sqrt{k^2 - (m\pi/h_a)^2}$.

At the matching sections between the regions, the field must satisfy the continuity

conditions for pressure and normal velocity

$$\begin{cases} p^{(I)} = p^{(II)} & , \quad |y| \leq h_a/2, \\ \partial_x p^{(I)} = \partial_x p^{(II)} & , \quad |y| \leq h_a/2. \end{cases} \tag{3.6}$$

and the rigid boundary condition on the lateral walls

$$\partial_x p^{(I)} = 0, |y| > h_a/2. \tag{3.7}$$

The scattering matrix of the single row, $\mathbf{S}_e$, relates the incident and scattered waves on each side of the unit cell. This matrix is defined as

$$\begin{pmatrix} \vec{B}_0 \\ \vec{A}_L \end{pmatrix} = \mathbf{S}_e \begin{pmatrix} \vec{A}_0 \\ \vec{B}_L \end{pmatrix}, \tag{3.8}$$

where $\vec{A}_0, \vec{B}_L$ are the modal amplitudes of incident waves, and $\vec{B}_0, \vec{A}_L$ are the modal amplitudes of reflected waves (see Fig. 3.3a). Since the unit cell is symmetrical with respect to $x$, the matrix $\mathbf{S}_e$ is

$$\mathbf{S}_e = \begin{bmatrix} \mathbf{R}_e & \mathbf{T}_e \\ \mathbf{T}_e & \mathbf{R}_e \end{bmatrix}, \tag{3.9}$$

with $\mathbf{R}_e$ and $\mathbf{T}_e$ the reflection and transmission matrices, valid both for left– and right–going incident waves. These matrices can be calculated using the operator "$\star$", defined in Appendix 3.A, which enables us to assemble consecutive scattering elements. Accordingly to Fig. 3.3b, the scattering matrix $\mathbf{S}_e$ can be expressed as

$$\mathbf{S}_e = \mathbf{S}_1 \star \mathbf{S}_2 \star \mathbf{S}_3 \star \mathbf{S}_4 \star \mathbf{S}_1, \tag{3.10}$$

where $\mathbf{S}_1, ..., \mathbf{S}_4$ are the scattering matrices of each of the elements of the cell, considered separately. Since elements 1 and 3 are straight segments, its reflection terms are zero

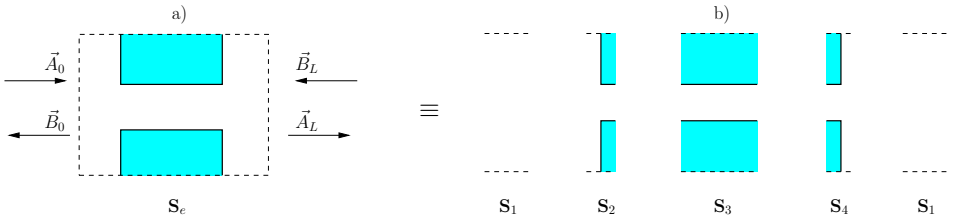


**Figure 3.3**: *a) Incident and scattered waves on each side of the unit cell.* $\mathbf{S}_e$ *indicates the scattering matrix of the cell. b) Decomposition of the unit cell in elementary scattering elements.* $\mathbf{S}_1 - \mathbf{S}_4$ *indicate the scattering matrices of each element.*

matrices [0] and the corresponding scattering matrices $\mathbf{S}_1$ and $\mathbf{S}_3$ are simply given by

$$\mathbf{S}_1 = \begin{bmatrix} [0] & \mathbf{D}^{(I)}(L_1) \\ \mathbf{D}^{(I)}(L_1) & [0] \end{bmatrix}, \tag{3.11}$$

$$\mathbf{S}_3 = \begin{bmatrix} [0] & \mathbf{D}^{(II)}(L_2) \\ \mathbf{D}^{(II)}(L_2) & [0] \end{bmatrix}, \tag{3.12}$$

with $\mathbf{D}^{(i)}(x) = \text{diag}\{\exp(\jmath k_{x_n}^{(i)} x)\}$, $i = I, II$. Matrices $\mathbf{S}_2$ and $\mathbf{S}_4$ are obtained from the modal expansions of the continuity equations (3.6) and (3.7). From the admittance matrix technique presented in Sec. 1.1.4, these matrices are obtained as

$$\mathbf{S}_2 = \begin{bmatrix} \mathbf{R}_b & \mathbf{T}_a \\ \mathbf{T}_b & \mathbf{R}_a \end{bmatrix}, \tag{3.13}$$

$$\mathbf{S}_4 = \begin{bmatrix} \mathbf{R}_a & \mathbf{T}_b \\ \mathbf{T}_a & \mathbf{R}_b \end{bmatrix}, \tag{3.14}$$

with,

$$\begin{aligned}
\mathbf{R}_a &= \left[\mathbf{I} + \mathbf{F}\left(\mathbf{\Gamma}^{(I)}\right)^{-1}\left({}^t\mathbf{F}^*\mathbf{\Gamma}^{(II)}\right)\right]^{-1}\left[\mathbf{F}\left(\mathbf{\Gamma}^{(I)}\right)^{-1}\left({}^t\mathbf{F}^*\mathbf{\Gamma}^{(II)}\right) - \mathbf{I}\right], \\
\mathbf{T}_a &= \left(\mathbf{\Gamma}^{(I)}\right)^{-1} {}^t\mathbf{F}^*\mathbf{\Gamma}^{(II)}\left(\mathbf{I} - \mathbf{R}_a\right), \\
\mathbf{R}_b &= \left(\mathbf{\Gamma}^{(1)} + {}^t\mathbf{F}^*\mathbf{\Gamma}^{(II)}\mathbf{F}\right)^{-1}\left(\mathbf{\Gamma}^{(I)} - {}^t\mathbf{F}^*\mathbf{\Gamma}^{(II)}\mathbf{F}\right), \\
\mathbf{T}_b &= \mathbf{F}\left(\mathbf{I} + \mathbf{R}_b\right),
\end{aligned}$$

where $\mathbf{\Gamma}^{(i)} = \text{diag}\left\{\jmath k_{xn}^{(i)}\right\}$, $i = I, II$, $\mathbf{I}$ is the identity matrix, $\mathbf{F}$ is the matching matrix, defined as,

$$F_{mn} = \int_{-h_b/2}^{h_b/2} \phi_n^{(I)} \phi_m^{(II)} \mathrm{d}y, \tag{3.15}$$

and ${}^t\mathbf{F}^*$ the conjugate transpose of $\mathbf{F}$.

## 3.3 System composed of $N_r$ rows

The scattering matrix, $\mathbf{S}_g$, of a system composed of $N_r$ periodic rows can be calculated simply from the scattering matrices of each row, $\mathbf{S}_{ej}$, $j = 1, 2, \ldots, N_r$ (Fig. 3.4). The matrix $\mathbf{S}_g$ is given by

$$\mathbf{S}_g = \mathbf{S}_{e1} \star \mathbf{S}_{e2} \star \ldots \star \mathbf{S}_{eN_r}. \tag{3.16}$$

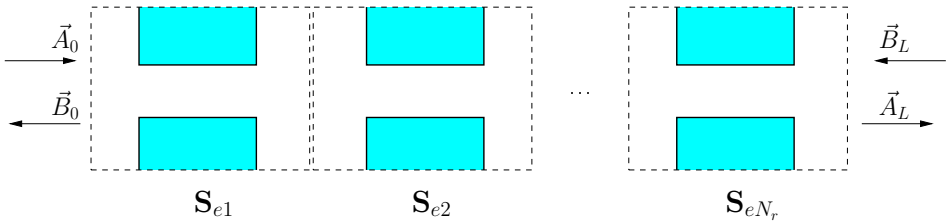


**Figure 3.4**: *Scattering matrix of a system composed of $N_r$ periodic rows.*

## 3.4 Infinite periodic system

Consider now the case of an infinite periodic system along $x$ and $y$. The goal is to find the Bloch wavenumbers, $k_B$, giving the dispersion relation of the system.

The application of the Bloch-Floquet theorem in both directions $x$ and $y$ enables us to reduce the domain to its unit cell, shown in the Fig. 3.5. The amplitude coefficients at each side of the cell satisfies the Bloch conditions

$$\begin{pmatrix} \vec{A}_L \\ \vec{B}_L \end{pmatrix} = \mu \begin{pmatrix} \vec{A}_0 \\ \vec{B}_0 \end{pmatrix}, \tag{3.17}$$

with $\mu = \exp(\jmath k_B D_x)$ the phase shift in the $x-$direction. Combining Eqs. (3.17) and (3.8), leads to the following generalised eigenvalue problem [10, 23]:

$$\begin{bmatrix} \mathbf{T}_e & \mathbf{R}_e \\ [0] & \mathbf{I} \end{bmatrix} \begin{pmatrix} \vec{A}_0 \\ \vec{B}_L \end{pmatrix} = \mu \begin{bmatrix} \mathbf{I} & [0] \\ \mathbf{R}_e & \mathbf{T}_e \end{bmatrix} \begin{pmatrix} \vec{A}_0 \\ \vec{B}_L \end{pmatrix}. \tag{3.18}$$

For a fixed frequency and angle of incidence, the eigenvalues of this problem, $\mu$, give the Floquet-Bloch wavenumbers $k_B$ through the relation

$$k_B = \frac{1}{D_x} \left( \arg \mu - \jmath \ln |\mu| \right) \tag{3.19}$$

and the associated eigenvectors $\left(\vec{A}_0, \vec{B}_L\right)$ contain the modal amplitudes allowing us to compute the wave field associated to each Bloch mode. In the absence of losses (as in the present case) we find two types of solutions: propagative modes ($k_b \in \mathbb{R}$) and evanescent modes ($k_b \in \mathbb{I}$). Note that propagative modes are bounded in the interval $k_B = [-\pi/D_x, \pi/D_x]$. Frequency bands where no propagative modes exists are called band gaps.

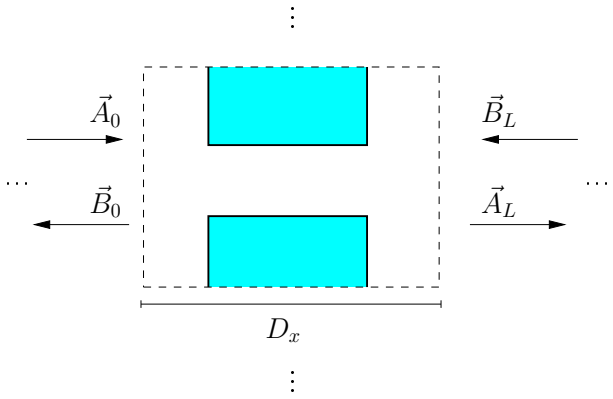


**Figure 3.5**: *Unit cell of the infinite lattice.*

## Direct lattice, reciprocal lattice and band structure

The physical lattice defined in the space $(x, y)$ is called the direct lattice. To this lattice, it is associated a reciprocal lattice in the space $(k_x, k_y)$, which is also periodic with periods $2\pi/D_x$ and $2\pi/D_y$ [see Eqs. (3.3) and (3.19)]. Thus, the reciprocal lattice can also be reduced to a unit cell, where all possible wavenumbers are entirely represented. If, in addition, the geometry of the lattice is symmetric, this unit cell can be reduced to an even smaller zone, called the first Brillouin zone. This zone is obtained by folding the $(k_x, k_y)$–space following the symmetry axis.

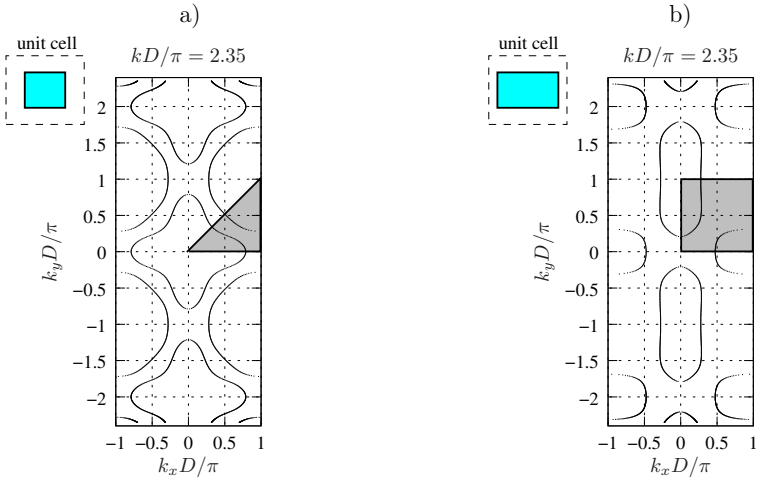


**Figure 3.6**: *$(k_x, k_y)$–space for a) a square lattice with square scatterers and b) a square lattice with rectangular scatterers. The shaded region represents the Brillouin zone. The insets represent a single period of the corresponding direct lattices.*

Fig. 3.6 shows the $(k_x, k_y)$–space, at a given frequency, for two types of lattice. The first one, Fig. 3.6a, is a square lattice with square scatterers. Since, the lattice is geometrical with respect to the $x-$axis, the $y-$axis and the axis defined by $x = y$, the Brillouin zone is represented with a triangle. The second case, shown in Fig. 3.6b, is a square lattice with rectangular scatterers. Since in this case the axis of symmetry are the $x-$axis and $y-$axis, the Brillouin zone is represented with a square. Note that all the possible solutions are represented inside the Brillouin zone, and the entire $(k_x, k_y)$–space can be constructed by successively unfolding this zone. The band structure of the lattice is obtained from the solutions located on the edge of the Brillouin zone.

## 3.5 Results

### 3.5.1 Transmission coefficient of a system composed of $N_r$ rows

Consider a lattice composed of $N_r$ periodic rows (see Fig. 3.4), excited at normal incidence, $\theta = 0$, with $D_y = D_x = D$, $L_b = h_b = D/2$. The energy trasmission coefficient of the lattice, $T$, is

$$T = \frac{W_t}{W_i} \tag{3.20}$$

where $W_t$ and $W_i$ are respectively the transmitted and incident energy flux, see Eq. (2.4). From the orthogonality of functions $\phi_n^{(I)}(y)$, the energy flux is

$$W_i = \frac{1}{2k}\mathrm{Im}\left\{ {}^t\vec{A}_0^{(I)*}\Gamma^{(I)}\vec{A}_0^{(I)} \right\}, \tag{3.21}$$

$$W_t = \frac{1}{2k}\mathrm{Im}\left\{ {}^t\vec{A}_L^{(I)*}\Gamma^{(I)}\vec{A}_L^{(I)} \right\}. \tag{3.22}$$

The modal expansions are truncated to 15 plane waves in region (I) and 8 modes in region (II). Fig. 3.7a shows the transmission coefficient vs. the reduced wavenumber $kD/\pi$. The curves shows the variation of $T$ for $N_r = 2, 4$ and 6 rows. We observe the formation of gaps in the transmission coefficient, which attenuation increases with the number of rows.

The results are compared to the band structure of the corresponding infinite lattice (see Fig. 3.7b). The dispersion relation exhibit three bandgaps coinciding with the dips observed in the transmission coefficient.

### 3.5.2 Complete band structure of the infinite periodic lattice

Figure 3.8 shows the complete band structure of the system. The result is compared to the band structure calculated using a plane wave expansion (PWE) code implemented

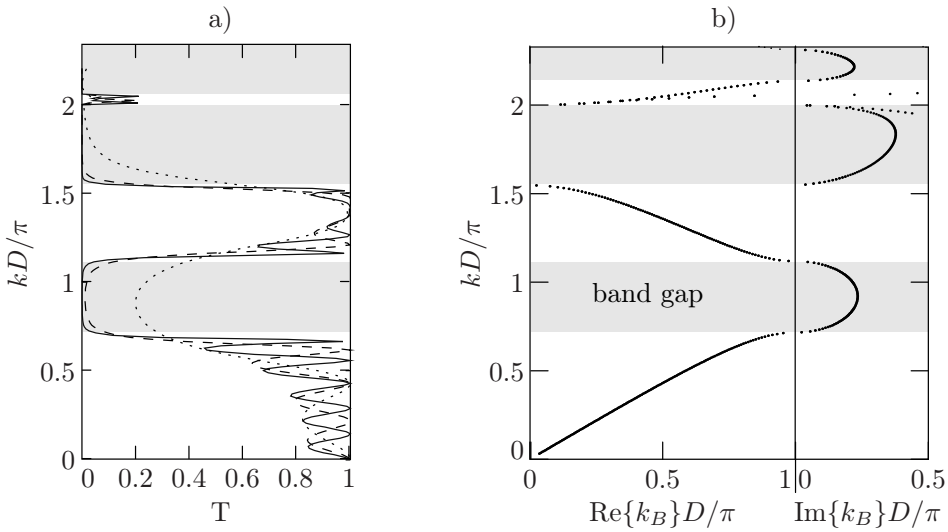


**Figure 3.7***: a) Transmission coefficient at normal incidence of a lattice composed of 2 rows (dotted line), 4 rows (dashed line), and 6 rows (solid line). b) Real and imaginary parts of the dispersion relation.*

in our research group (see [70] for details). Convergence of the multimodal result was achieved taking 16 modes in region $(I)$ and 8 modes in region $(II)$, while 50 plane waves were used in the PWE computation. Both results are in excellent agreement, which allows us to validate the multimodal approach presented in this Chapter.

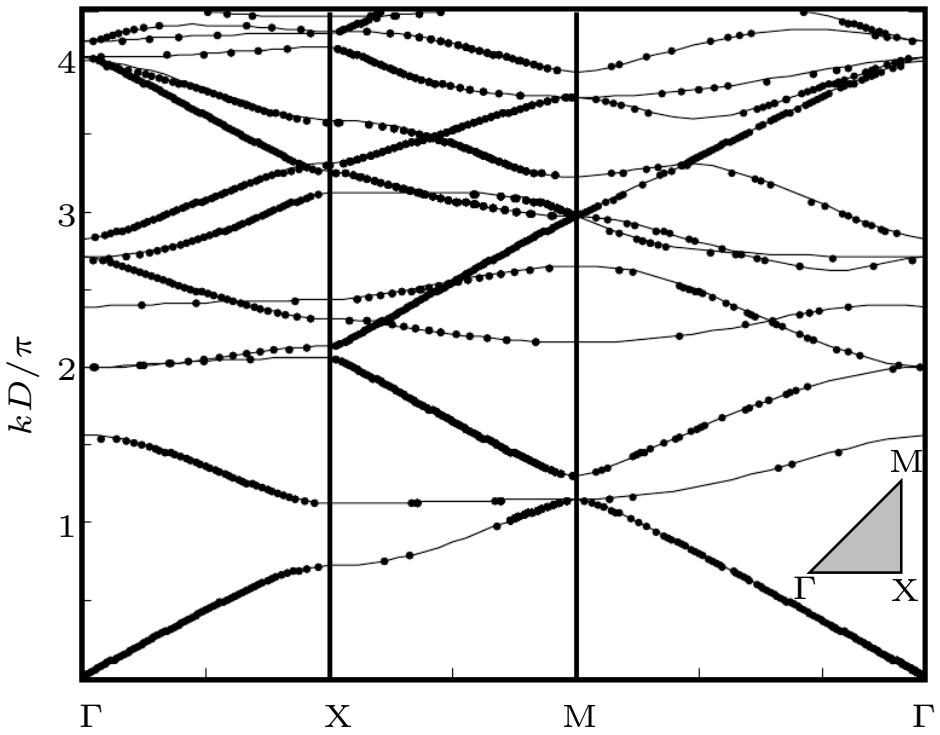


**Figure 3.8***: complete band structure of a periodic lattice with dimensions* $D_y = D_x = D$*,* $L_b = h_b = D/2$*. Points represent the multimodal solutions and lines represent the PWE solution.*

# Appendix 3.A. Assembling of scattering matrices

Consider two scattering objects I and II characterised by their respective scattering matrices $\mathbf{S}_{\mathrm{I}}$ and $\mathbf{S}_{\mathrm{II}}$, as indicated in the Fig. 3.9. These matrices are given by

$$\begin{pmatrix} A_2 \\ B_1 \end{pmatrix} = \mathbf{S}_{\mathrm{I}} \begin{pmatrix} A_1 \\ B_2 \end{pmatrix}, \tag{3.23}$$

$$\mathbf{S}_{\mathrm{I}} = \begin{bmatrix} T_{\mathrm{I}} & R'_{\mathrm{I}} \\ R_{\mathrm{I}} & T'_{\mathrm{I}} \end{bmatrix}, \tag{3.24}$$

and

$$\begin{pmatrix} A_3 \\ B_2 \end{pmatrix} = \mathbf{S}_{\mathrm{II}} \begin{pmatrix} A_2 \\ B_3 \end{pmatrix}, \tag{3.25}$$

$$\mathbf{S}_{\mathrm{II}} = \begin{bmatrix} T_{\mathrm{II}} & R'_{\mathrm{II}} \\ R_{\mathrm{II}} & T'_{\mathrm{II}} \end{bmatrix}. \tag{3.26}$$

Combining the previous equations, it is possible to find the global scattering matrix $\mathbf{S}_{\mathrm{I,II}}$ relating the quantities on both extremities [27]:

$$\begin{pmatrix} A_3 \\ B_1 \end{pmatrix} = \mathbf{S}_{\mathrm{I,II}} \begin{pmatrix} A_1 \\ B_3 \end{pmatrix}, \tag{3.27}$$

$$\mathbf{S}_{\mathrm{I,II}} = \begin{bmatrix} T_{\mathrm{II}}(1 - R'_{\mathrm{I}} R_{\mathrm{II}})^{-1} T_{\mathrm{I}} & R'_{\mathrm{II}} + T_{\mathrm{II}}(1 - R'_{\mathrm{I}} R_{\mathrm{II}})^{-1} R'_{\mathrm{I}} T'_{\mathrm{II}} \\ R_{\mathrm{I}} + T'_{\mathrm{I}}(1 - R_{\mathrm{II}} R'_{\mathrm{I}})^{-1} R_{\mathrm{II}} R'_{\mathrm{I}} & T'_{\mathrm{I}}(1 - R_{\mathrm{II}} R'_{\mathrm{I}})^{-1} T'_{\mathrm{II}} \end{bmatrix}. \tag{3.28}$$

The previous matrix relation is denoted by de the symbol "$\star$", such that $\mathbf{S}_{I,II} = \mathbf{S}_I \star \mathbf{S}_{II}$.

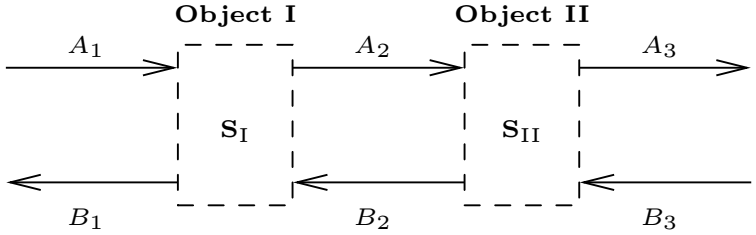


**Figure 3.9***: Assembling of two scattering objects.*

# Chapter 4

# Sound propagation in periodic urban areas

A regular urban area can be considered, as a first approximation, as a periodic lattice of interconnected streets, see Fig. 4.1 below. Under this assumption specific properties of wave propagation in periodic media can be investigated in a urban context. This Chapter is concerned with the formation of forbidden frequency bands in periodic urban areas. Particular attention is payed to the effect of radiative losses in the media, an essential characteristic of the urban environment. The Chapter is adapted from of an article published in the *Journal of Applied Physics* [56].

**Figure 4.1***: Aerial view of The Eixample district, Barcelona (Spain). Image: Xavier Jubierre / El Periódico*

## 4.1 Introduction

In styling 3D extended distributions of buildings, the assumption of a periodic distribution is convenient to model the acoustic field, as it describes reasonably well some real situations (see the works by Picaut [69] and Heimann [34]). Doing this, it is possible to investigate the propagation through a large built area, while taking into account rigorously the three-dimensional characteristics of the problem, as the radiation above the streets. Periodic media are known to exhibit peculiar properties (band gaps, strong dispersion, anisotropy, negative refraction) and have attracted a great deal of interest in electromagnetics and optics [45, 54] as, more recently, for acoustic and elastic waves [23, 30, 85, 87, 90, 92]. By assuming a periodic distribution of buildings in modelling the sound propagation in an urban environment, one may thus expect specific properties of periodic media to occur. However, would these properties remain in the case (a lattice of open urban Ions) where important radiative losses are generally observed? The aim of this Chapter is to investigate the competitive effects of the periodicity and the wave radiation.

In this work we investigate both experimentally and numerically the specific properties of open periodic lattices, in particular the presence of band gaps. The experimental lattice is made of $9 \times 26$ wooden cuboids, which represent the buildings. The numerical characterisation of the lattice is based on the modal–FE formulation of the wave propagation within open waveguiding structures, see Chapter 1. It basically consists in a finite element (FE) discretisation of the problem in the transverse section of the waveguide (the street) with the open side artificially closed by perfectly matched layers (PML [8]), and a multimodal formulation of the propagation in the longitudinal direction.

The Chapter is organised as follows. Sec. 4.2 shows the experimental device used in this work. Sec. 4.3 outlines the application of the modal–FE method to the study of periodic lattices. Two kinds of problems are treated: an infinite periodic lattice along one of the horizontal directions and an infinite periodic lattice along the two horizontal directions. In this section, some common issues on leaky modes and PML modes are discussed. Experimental and numerical results are presented in Sec. 4.4. The effect of the opening is evaluated by comparing the open lattice with an identical one, closed at the top with a rigid boundary. In the sequel, the open lattice is called OL and the closed one is called CL.

## 4.2 Experimental setup

The experimental setup is shown in the Fig. 4.2. Experiments are carried out in a semi-anechoic room. Walls are coated with a melamine foam, effective from 1 kHz onwards. The studied lattice is composed of $9 \times 26$ rectangular wooden cuboids with spatial periods $D_x = D_y = 7.5$ cm and obstacles dimensions $l_x \times l_y \times h = 5 \times 5 \times 15$ cm. Thus, the lattice has a total surface of $0.67 \times 1.95$ m$^2$ and the filling fraction is

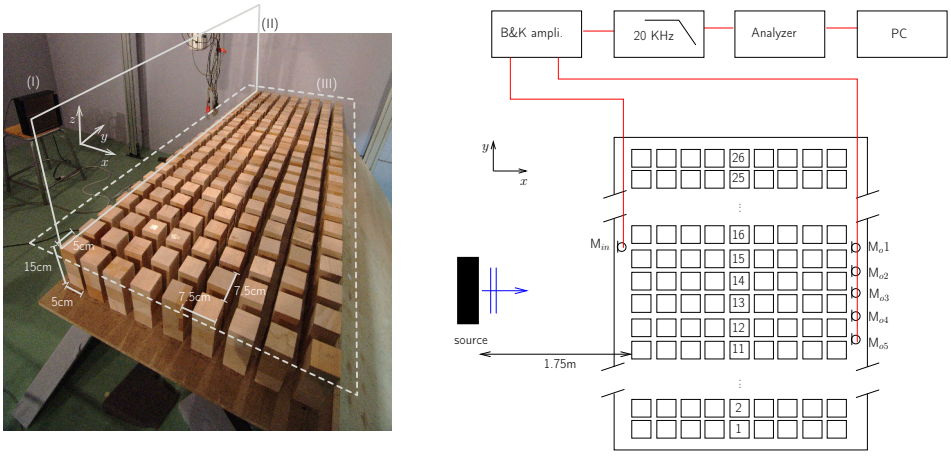


**Figure 4.2**: *Experimental setup. The image on the left shows a picture of the experimental setup. Symbol (I) indicates the parametric antenna, (II) represents a screen permitting to avoid direct sound transmission over the lattice, (III) indicates the covering used to obtain the CL. The figure on the right shows a schematic representation of the experimental setup. The parametric antenna is placed perpendicular to the lattice at the distance 1.75 m. Symbols '×' represent microphones positions. The input pressure is measured at the position denoted by $M_{in}$. The output pressure is taken at five points behind the lattice, denoted by $M_{o1}$ to $M_{o5}$, respectively. Signals are amplified and lowpass filtered to eliminate any remaining high frequency waves radiated by the source.*

$ff = 44\%$. A screen is placed above the first row to avoid direct sound propagation from the source to the back of the lattice, which could distort the measurements. The CL is obtained by covering the OL with a wooden board, as indicated by the dashed rectangle in the Fig. 4.2.

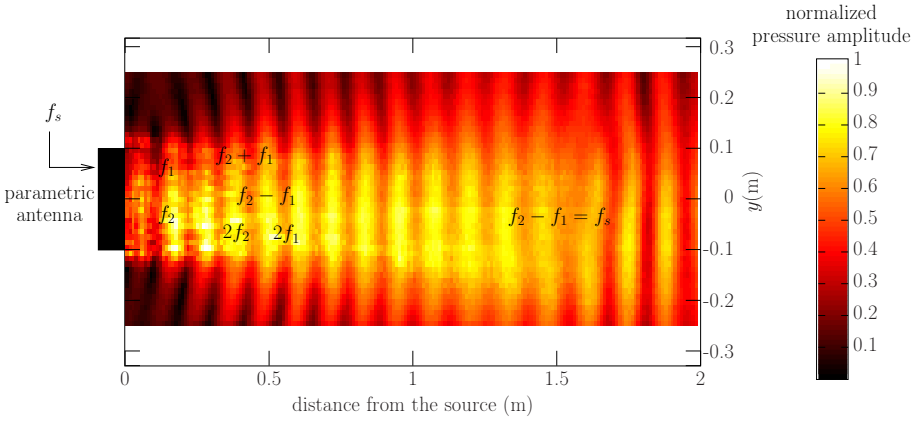


**Figure 4.3**: *Acoustic field emitted by the parametric antenna in the $(x, y)$–plane.*

The lattice is excited using a parametric antenna model HSS (HyperSound Audio System), product from the American Technology Corporation. From an input signal at frequency $f_s$, the source emits separately two high amplitude ultrasonic waves at frequencies $f_1$ and $f_2$, related by $f_2 = f_1 + f_s$, with $f_1 = 47$ kHz. Then, due to non-linear interactions, new spectral components appear, among which are $f_1 - f_2, 2f_1, f_1 + f_2, 2f_2$. Because of the increase of attenuation with frequency, the difference frequency component $f_s = f_2 - f_1$ is predominant far from the source, while keeping the ultrasound properties. Thus, this device is able to deliver ultra-directive plane waves in the audible frequency range.

Fig. 4.3 shows the radiated field, measured at $f_s = 1.6$ kHz. The figure shows high frequency components in the near field, that vanish approximately 1 m away from the source. Beyond this distance, only the difference frequency $f_s$ remains, and it can be observed that wavefronts become plane.

Experiments have been performed by placing the antenna at 1.75 m from the lattice and the source signal is a sweep sine from 1 to 8.3 kHz. To fix ideas, this would correspond to a few tens of a Hertz at "urban" scale. For instance, if the laboratory experiment corresponds to 1:100 scale, the frequency range at full scale would be 10 to 83 Hz. Such low frequency waves can be practically measured in urban environments as being produced by either heavy industrial machineries, intense impulse noise, or, for a part, the traffic noise [16, 63], and they may propagate on long distances, compared with higher frequency waves.

The acoustic pressure is measured using 1/2 in. microphones (B&K 4190), connected to a preamplifier (B&K 2669) and a conditioning amplifier (B&K Nexus 2669). Additionally, signals are lowpass filtered up to 20 kHz to eliminate any remaining high frequency component emitted by the source.

With the aim of detecting the band gaps and passbands of the lattice, we measured the transfer function between the input and output pressure field. The transfer function was obtained as the averaged pressure value at 5 output points, designed by $M_{01}$ to $M_{05}$ in Fig. 4.2. The input pressure is measured at the position denoted by $M_{in}$ in the same figure. A single input point was found to be representative enough of the incident field.

We also measured the pressure field on a horizontal plane above the lattice. This measurement was performed using the same system as in Chapter 2

## 4.3 Modelling of periodic lattices using the modal–FE Method

### 4.3.1 The infinite periodic lattice along $y$

Consider the domain represented in Fig. 4.4.a. It consists in a finite series of periodic rows of rectangular cuboids, disposed along the $y-$direction. All the rows have the same spatial period $D_y$. The obstacles size and the distance between rows are arbitrary along the $x-$direction. $\Omega$ represents the whole domain and $\Gamma$ designs the boundaries (obstacles and ground) which are assumed to be perfectly reflecting. To our purposes, the domain is closed at the top with a PML. Next, assuming an harmonic plane wave excitation, the Floquet-Bloch theorem imposes the following condition to the pressure field $p(x, y, z)$:

$$p(x, y + mD_y, z) = \exp\left(\jmath mk \sin(\theta) D_y\right) p(x, y, z), \tag{4.1}$$

with $m \in \mathbb{Z}$, $k$ the wavenumber and $\theta$ the angle of incidence with respect to the $x-$axis. From Eq. (4.1), $\Omega$ can be reduced to the equivalent domain $\Omega_e$, shown in the Fig. 4.4.b. This domain can be regarded as a piecewise constant waveguide, delimited at both sides by periodic boundaries $\Gamma_L$ and $\Gamma_R$ and at the top by the PML. This waveguide contains $N_s$ straight segments with lengths $L^{(i)}$, $i = 1, ..., N_s$, and two different cross–sections $S_1$ and $S_2$.

The problem in $\Omega_e$ is written as

$$\begin{cases} \left(\Delta_\tau + k^2\right) p(x, y, z) = 0, \ \forall (x, y, z) \in \Omega_e, \\ \partial_n p(x, y, z) = 0, \ \forall (x, y, z) \in \Gamma, \\ p(x, y \in \Gamma_R, z) = \mu_y p(x, y \in \Gamma_L, z), \\ \partial_n p(x, y \in \Gamma_R, z) = -\mu_y \partial_n p(x, y \in \Gamma_L, z), \end{cases} \tag{4.2}$$

where $\partial_n$ denotes the outward normal derivative with respect to the boundaries, $\mu_y = \exp(\jmath k \sin(\theta) D_y)$ is the phase-shift imposed by the Floquet-Bloch theorem and $\Delta_\tau$,

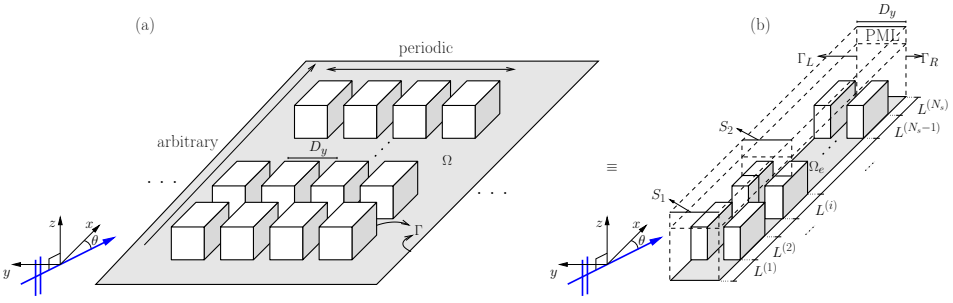


**Figure 4.4**: *a) Geometry of the periodic lattice along y. b) Unit cell of the lattice.*

defined as

$$\Delta_\tau = \frac{\partial^2}{\partial x^2} + \frac{\partial^2}{\partial y^2} + \frac{1}{\tau}\frac{\partial}{\partial z}\left(\frac{1}{\tau}\frac{\partial}{\partial z}\right), \tag{4.3}$$

denotes the modified Laplacian operator which takes into account the PML. The coefficient $\tau$ of the PML is given by

$$\tau = \begin{cases} A\exp(\jmath\beta), \text{ inside the PML,} \\ 1, \text{ elsewhere,} \end{cases} \tag{4.4}$$

with $A > 0$ and $0 < \beta < \pi/2$. The transverse problem is discretised using the FEM and Eqs. (4.2) are transformed into the discrete form

$$\vec{P}''(x) + \left(k^2\mathbf{I} - \mathbf{M}_p^{-1}\mathbf{K}_p\right)\vec{P}(x) = \vec{0}, \tag{4.5}$$

where $\mathbf{K}_p, \mathbf{M}_p$ are respectively the stiffness and mass matrices, resulting from the FEM discretization of the transverse differential operators, and verifying the lateral Bloch conditions (see Appendix 4.A).

In each straight segment, a general solution of (4.5) can be found as a function of the eigenvalues $\alpha_n^2$ and eigenvectors $\vec{\Phi}_n$ of the matrix $\mathbf{M}_p^{-1}\mathbf{K}_p$

$$\vec{P}^{(i)}(x) = \mathbf{\Phi}\left(\mathbf{D}(x)\vec{C}_1 + \mathbf{D}(L^{(i)} - x)\vec{C}_2\right), \tag{4.6}$$

where $\mathbf{\Phi} = [\vec{\Phi}_1, \vec{\Phi}_2, ..., \vec{\Phi}_N]$ is the eigenvectors matrix, $\mathbf{D}(x)$ is a diagonal matrix such that $D_{nn} = \exp(\jmath k_{xn}x)$, with $k_{xn} = (k^2 - \alpha_n^2)^{1/2}$ the propagation constants, and vectors $\vec{C}_1$, $\vec{C}_2$ contain the unknowns modal amplitudes for forward and backward waves, respectively, which depend on the conditions at the extremities of the segments. To find these coefficients, the mode-matching method is used. The continuity equations for pressure and normal velocity are established at the waveguide discontinuities. Then, an output condition is defined by an admittance matrix $\mathbf{Y}$, fulfilling $\vec{U} = \mathbf{Y}\vec{P}$, with $\vec{U}$ the $x-$component of the particle velocity on the basis of the interpolating polynomials used for the FEM computation. Later, using the continuity equations, the input and output admittance matrices of each straight segment are computed, step-by-step, from the output to the input segment. Finally, from a source condition, the wave field can be obtained at any point within the domain [27, 28, 64]. The output condition corresponds to the characteristic admittance of the medium.

### 4.3.2 The infinite periodic lattice along $x$ and $y$

An infinite periodic lattice along $x$ and $y$ is now considered. A similar process as described in Sec. 3.4 is used to find the Bloch wavenumers $k_B$. The application of the

Floquet-Bloch theorem in both directions allows to reduce the domain to its unit cell represented in the Fig. 4.5. Then, using the mode-matching method, the scattering matrix $\mathbf{S}$ of the unit cell, relating incident and scattered waves at the extremities, is obtained as

$$\begin{pmatrix} \vec{C}_b \\ \vec{C}_c \end{pmatrix} = \mathbf{S} \begin{pmatrix} \vec{C}_a \\ \vec{C}_d \end{pmatrix}, \tag{4.7}$$

where $\mathbf{S}$ takes the form

$$\mathbf{S} = \begin{bmatrix} \mathbf{R} & \mathbf{T} \\ \mathbf{T} & \mathbf{R} \end{bmatrix}, \tag{4.8}$$

$\mathbf{T}$ and $\mathbf{R}$ being the transmission and reflection matrices, respectively. Additionally, the periodicity in the $x-$direction imposes the following condition to the amplitude coefficients

$$\begin{pmatrix} \vec{C}_c \\ \vec{C}_d \end{pmatrix} = \mu_x \begin{pmatrix} \vec{C}_a \\ \vec{C}_b \end{pmatrix}, \tag{4.9}$$

with $\mu_x = \exp(\jmath k_B D_x)$. Then, the combination of Eqs. (4.7) and (4.9), leads to the generalised eigenproblem

$$\begin{bmatrix} \mathbf{T} & \mathbf{R} \\ [0] & \mathbf{I} \end{bmatrix} \begin{pmatrix} \vec{C}_a \\ \vec{C}_d \end{pmatrix} = \mu_x \begin{bmatrix} \mathbf{I} & [0] \\ \mathbf{R} & \mathbf{T} \end{bmatrix} \begin{pmatrix} \vec{C}_a \\ \vec{C}_d \end{pmatrix}, \tag{4.10}$$

with $[0]$ the zero matrix and $\mathbf{I}$ the identity matrix. Finally, the eigenvalues $\mu_x$ of this problem give the Floquet-Bloch wavenumbers $k_B$ and the associated eigenvectors

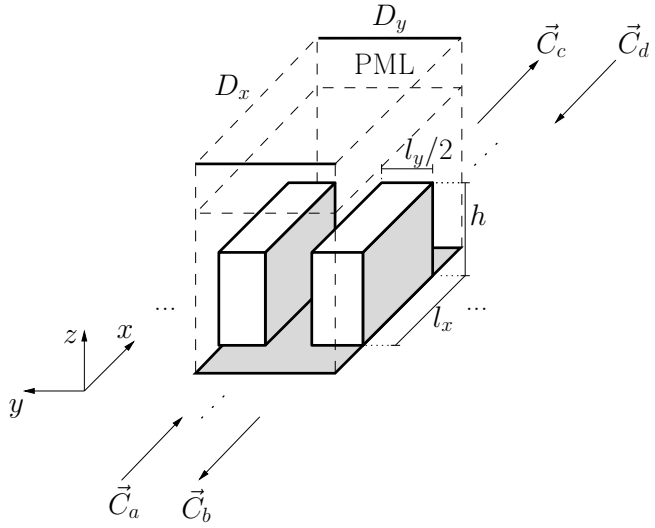


**Figure 4.5**: *Unit cell of the periodic lattice along $x$ and $y$. The spacial periods are $D_x$ and $D_y$. The obstacles length, width and height, are respectively denoted by $l_x$, $l_y$ and $h$.*

$\left(\vec{C}_a, \vec{C}_d\right)$ contain the amplitude coefficients allowing to compute the wave field for each mode.

### 4.3.3 Modelling of closed lattices

Using the techniques described in Secs. 4.3.1 and 4.3.2, the CL is modelled by replacing the PML termination at the top by a rigid boundary and considering $\tau = 1$ in the entire domain to obtain the classical Helmholtz equation.

### 4.3.4 On leaky modes and PML modes

When considering the CL, band gaps and propagative bands are represented by the solutions $\mu_x$ such that $\mathrm{Im}\{k_B\} \neq 0$ and $\mathrm{Im}\{k_B\} = 0$, respectively. In contrast, for the OL, all wavenumbers $k_B$ are complex because of the radiation losses above the lattice. Such solutions represent the so-called leaky modes, modes that are partly propagated through the lattice and partly radiated towards the upper part (the Fig. 4.6.b shows an example). A criterion for discriminate between band gaps and propagative bands for the leaky modes can be defined by a threshold value $\eta_0$ of the loss factor

$$\eta = \left| \frac{\mathrm{Im}\{k_B\}}{\mathrm{Re}\{k_B\}} \right|, \tag{4.11}$$

from which a given solution can be considered, either propagative $\eta(k_B) < \eta_0$, or evanescent $\eta(k_B) > \eta_0$.

Additionally, with the introduction of PML, "PML" modes arises [74, 77]. These modes, strongly localised in the artificial absorbing layer (Fig. 4.6.b), must be discarded since they do not represent solutions of the original problem. Indeed, they are unphysical solutions of the equivalent PML problem. A useful criterion to separate PML modes and leaky modes was proposed by Shi *et al.* [77], based on the ratio $E$ of the energy stored inside the PML volume $V_{PML}$ to the energy stored in the total volume $V_{tot}$ of the unit cell:

$$E = \frac{\int_{V_{PML}} |p|^2 \mathrm{d}V}{\int_{V_{tot}} |p|^2 \mathrm{d}V}. \tag{4.12}$$

From Figs. 4.6.a and 4.6.b, one should expect the ratio $E$ to present values close to zero for the leaky modes and much higher values for the undesired PML modes.

The main drawback of such criterion is that $E$ must be computed for each solution of Eq. (4.10), which considerably increases the computation time. However, a straightforward way to identify the PML modes comes from the fact that they mainly propagate in the free space above the periodic domain Then, for a given angle of incidence $\theta$, the wavenumbers of PML modes lie close to the so-called sound line, $k = k_x / \cos(\theta)$,

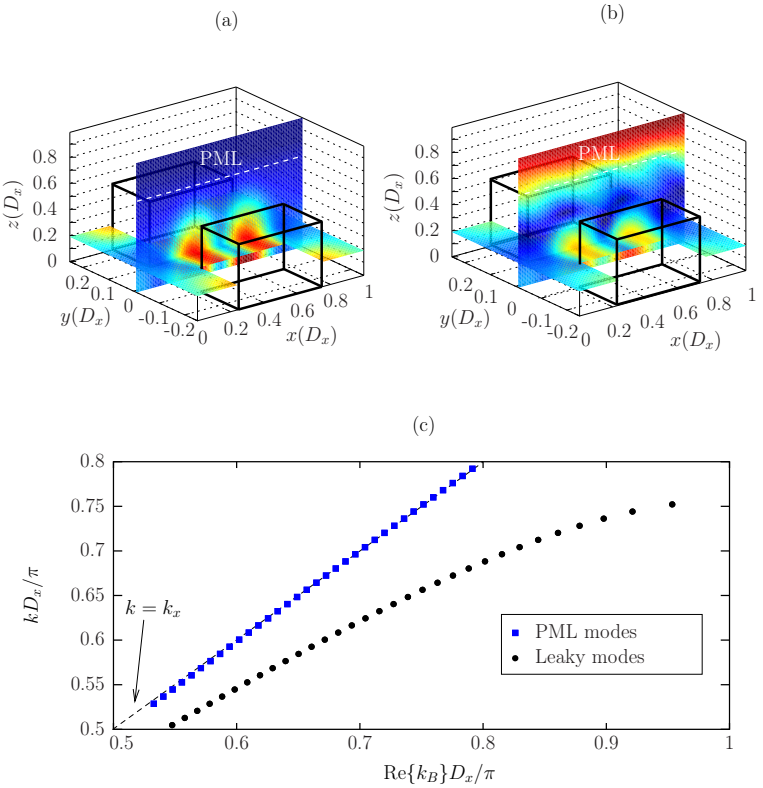


**Figure 4.6***: a) leaky mode, b) PML mode, c) dispersion relation for the leaky (dots) and PML modes (squares) in normal incidence. Note that PML solutions matches the sound line $k = k_x$ (dashed line)*

representing the dispersion relation of a plane wave propagating in the free space. This is illustrated in Fig. 4.6.c, where an arbitrary example of the dispersion relation of leaky and PML modes with normal incidence ($\theta = 0$) is represented. It is observed that the PML solutions match the sound line, while the leaky mode dispersion relation is bended, influenced due to the scattering in the medium. Note that the sound line is analogous to the light line for electromagnetic waves [77, 80]. This line can be regarded as the transition between evanescent and propagative leaky modes: assuming normal incidence ($k_y = 0$) and considering only the real part of $k_B$, the dispersion relation is approximated by $k^2 = (\mathrm{Re}\{k_B\})^2 + k_z^2$. From this relation, we see that for modes above the sound line ($\mathrm{Re}\{k_B\} < k$), the vertical wave vector component $k_z$ is real. In other words, these modes are directed vertically, so radiated above the lattice. Modes coinciding with the sound line ($\mathrm{Re}\{k_B\} = k$) represent waves propagating parallel to the horizontal plane and travelling at the speed of sound in free space. Finally, modes bellow the sound line ($\mathrm{Re}\{k_B\} > k$) become evanescent along $z$ and propagate along the $x-$direction with radiation losses defined by the imaginary part of $k_B$.

## 4.4 Results

### 4.4.1 Band gaps in the lattice

Figs. 4.7.b and 4.8.b show the band structure in normal incidence for the CL and OL, respectively. For the later case, the threshold loss factor $\eta_0$ is adjusted to $\eta_0 = 0.1$ to filter the evanescent modes, and PML solutions has been eliminated.

In these figures, labels 'mode $\nu$' denote the number $\nu$ of horizontal nodal lines of the mode: 'mode 0' indicates 0 nodal lines; 'mode 1', 1 nodal line, and so on. Figs. 4.7.c and 4.8.c show the shape of modes 0, 1 and 2 at a given frequency for the CL and the OL, respectively (note that the shape of this modes varies with frequency, although it keeps the same number of horizontal nodal lines). For the CL, the cutoff frequencies of these modes can be obtained by solving the 1D Helmholtz problem along $z$ with rigid boundary conditions. They are given by

$$f_\nu^{(\mathrm{CL})} = \frac{\nu c_0}{2h}.$$

Considering the sound speed $c_0 = 340$ m·s$^{-1}$, the first three frequencies are $f_{0,1,2}^{(\mathrm{CL})} = 0$ Hz, 1133 Hz and 2267 Hz. They are represented by the dashed lines in Fig. 4.7.b. For the OL, the cutoff frequencies of modes 0, 1, 2 are determined by the sound line, represented by the oblique dashed line in Fig. 4.8.b.

Since, with the present configuration, the source impinges uniformly on the input cross–section of the lattices, one should expect that only the mode 0 will be excited. For this reason, the band gaps for this mode have been highlighted, denoted by the shaded regions in Figs. 4.7.b and 4.8.b. Four band gaps are obtained in each case, defined in $[1.65 - 2.39]$ kHz, $[3.11 - 4.18]$ kHz, $[4.72 - 5.36]$ kHz and $[6.80 - 7.70]$ kHz for the CL and in $[1.70 - 2.49]$ kHz, $[3.09 - 4.23]$ kHz, $[4.73 - 5.39]$ kHz and $[6.80 - 7.91]$ kHz for the OL. Note that the band gaps positions for the mode 0 are quite similar in both cases.

Simulated results are compared to the experimental transfer functions shown in the Figs. 4.7.a and 4.8.a. The curves for the OL and CL are quite similar. They also show four band gaps, which are in good agreement with the computed band structures. Nevertheless, some differences in amplitude are visible. For instance, it can be observed that the first 3 band gaps are more attenuated in the OL, while the fourth band gap is more attenuated in the CL. This could be the result of a weak excitation of higher order modes, which could vary from one lattice to another. Comparing theoretical and experimental results, one observes that the measured band gaps are in general wider, surely due to the inherent weak disorder and finite dimensions of the experimental lattice. Other dissipative effects, as the absorption of wood, may also play a role.

Regarding only the first mode, it can be concluded that the main factor governing the behaviour of this mode is the periodicity in the horizontal directions, while the condition

at the top (closed or open) is not too relevant. In contrast, this does not happen with the higher order modes. Taking them into account, the presence of propagative modes is much more pronounced in the case of the CL. That seems logical since it is a lossless medium. However, an unexpected behaviour appears in the frequency band 3.85−4 kHz. The Fig. 4.9.b shows a zoom in this region of the band structure. It is observed that no propagative modes exist in the CL, while the mode 2 arises in the OL. To observe this phenomenon experimentally, we modify the lattice excitation. As mentioned before, the present configuration excites only the plane mode. In order to excite higher order modes, we place 5 cm height bar in front of the lattice (see Fig.4.9.a). With this configuration, the excitation is not plane anymore in the vertical direction $z$, meaning that higher order modes can be excited. The transfer functions are measured again in the frequency band $3.7 - 4.3$ kHz, as shown in the Fig. 4.9.c. The curve of the CL shows a gap in the region $3.85 - 4$ kHz, while the curve of the OL exhibits a slight bump, which agrees with the theoretical results.

### 4.4.2 Pressure fields

The wave field in the horizontal plane 1 cm above the lattice, at 2 kHz, has been measured (Fig. 4.10.a) and compared with the numerical field (Fig. 4.10.b), computed with the technique explained in Sec. 4.3.1. The field is computed for a single period $D_y$, then repeated 6 times to give an overall result. As the excitation frequency is located in the first band gap, fields exhibit a decay along the $x-$direction. Differences between the pressure fields are observed, that surely come from the non-uniformity of the experimental input signal, unlike the numerical excitation that equally extends over the $y-$direction. Also, the finite size and slight disorder of the experimental lattice may play a role. Despite the differences, both results seems to describe a similar global decay along $x$. To corroborate this, the mean value of pressure along the $y-$direction vs. $x$ has been computed. Results are compared in the Fig. 4.10.c. Globally, both curves show a similar behaviour. Discrepancies are observed before the distance 0.3 m, where the position of the theoretical lobes are shifted and their amplitude varies significantly with respect to the experimental curve. The agreement is better from 0.3 m onwards.

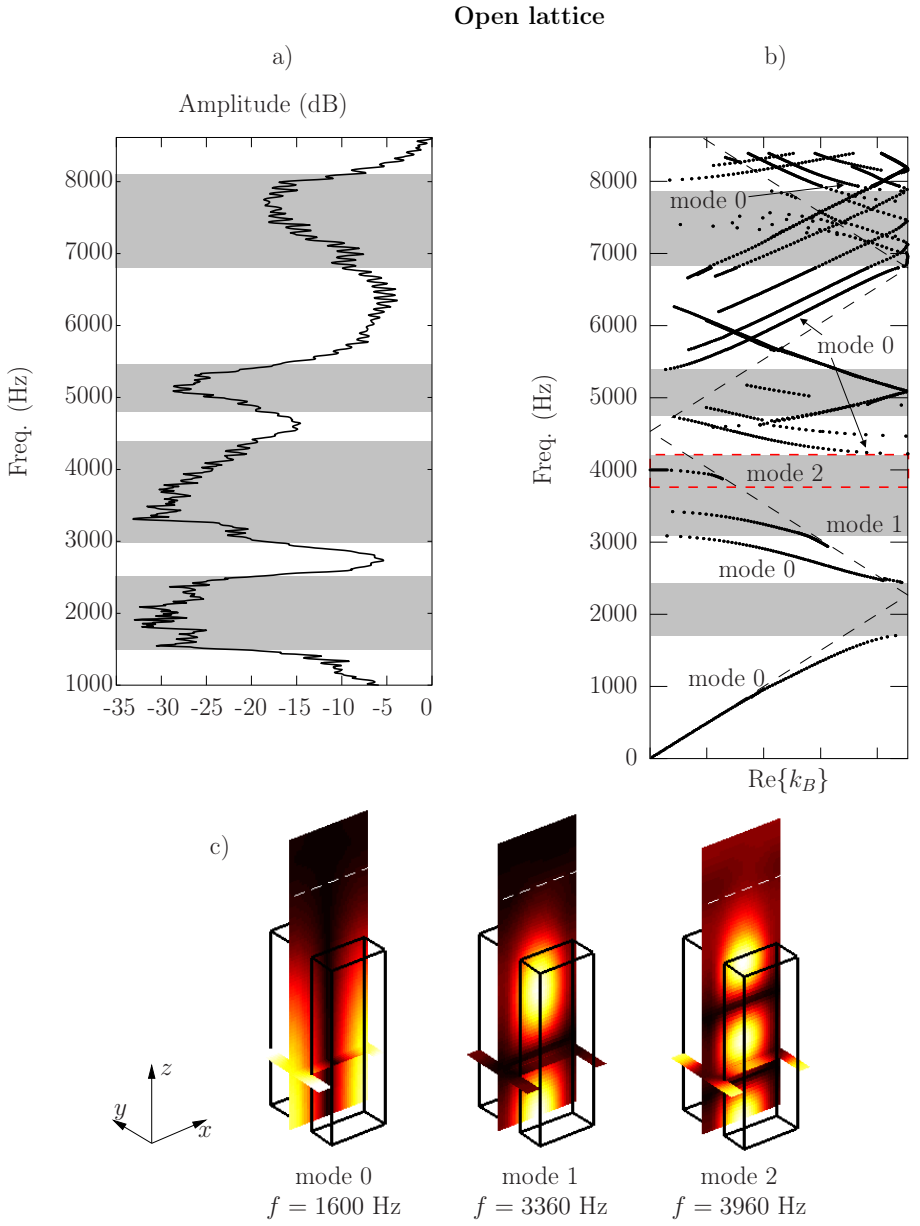


**Figure 4.7***: Results for the open lattice. a) Measured transfer function. Curves are normalised to 0 dB for a more comfortable reading. Shaded zones indicates band gaps. b) Band diagrams. Shaded zones indicates band gaps for the mode 0; c) Shape of modes 0, 1 and 2 at a given frequency.*

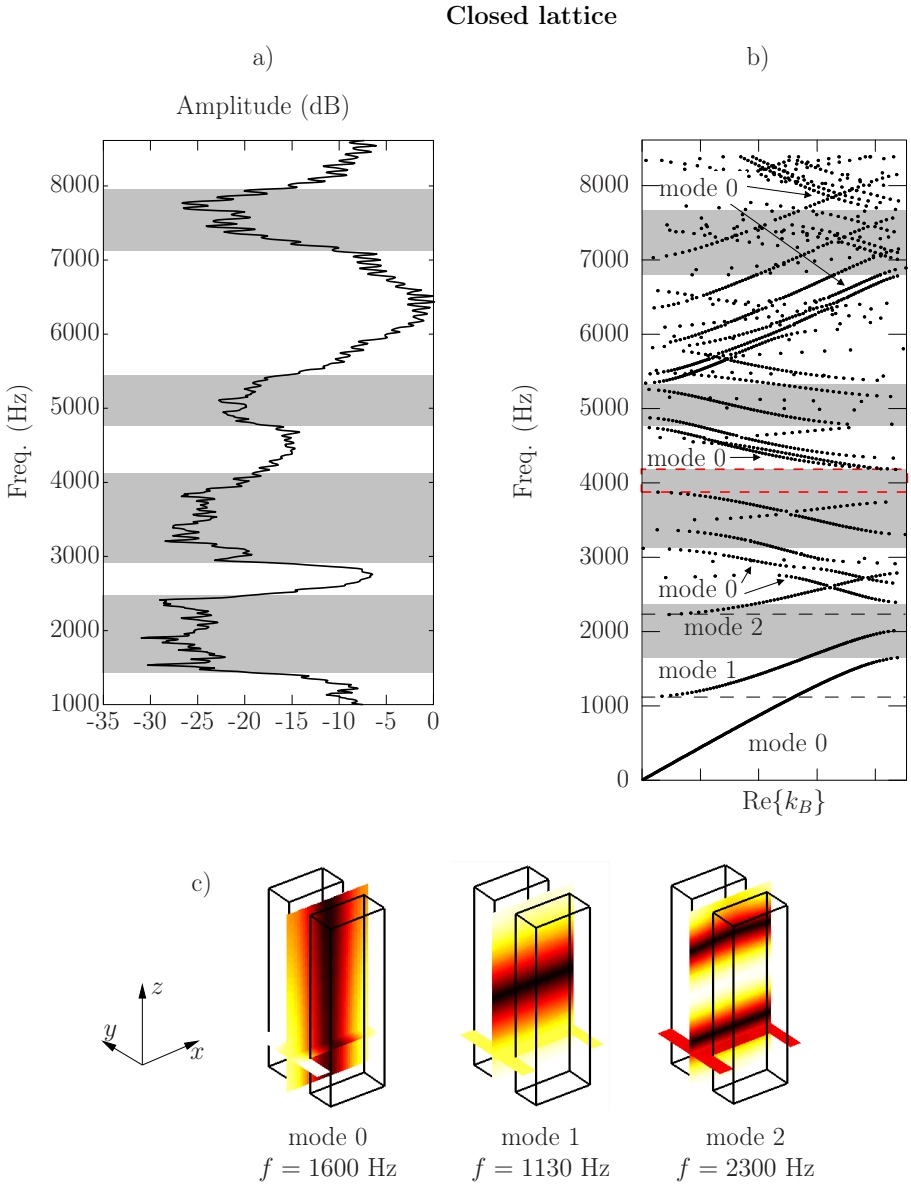


**Figure 4.8**: *Results for the closed lattice. a) Measured transfer function. Curves are normalised to 0 dB for a more comfortable reading. Shaded zones indicates band gaps. b) Band diagrams. Shaded zones indicates band gaps for the mode 0; c) Shape of modes 0, 1 and 2 at a given frequency.*

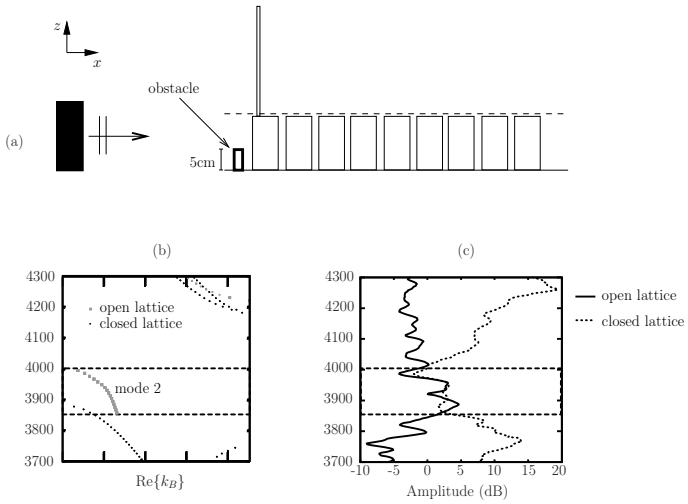


**Figure 4.9**: *a) position of the obstacle in front of the lattice, used to activate higher order modes; b) Band structure in the band* $3.7 - 4.3$ *kHz for the CL (dots) and the OL (squares). c) Measured transfer functions for the CL (dotted line) and the OL (continous line). Note that in the band* $3.85 - 4$ *kHz no propagative modes exists in the CL, while the mode 2 emerges in the OL.*

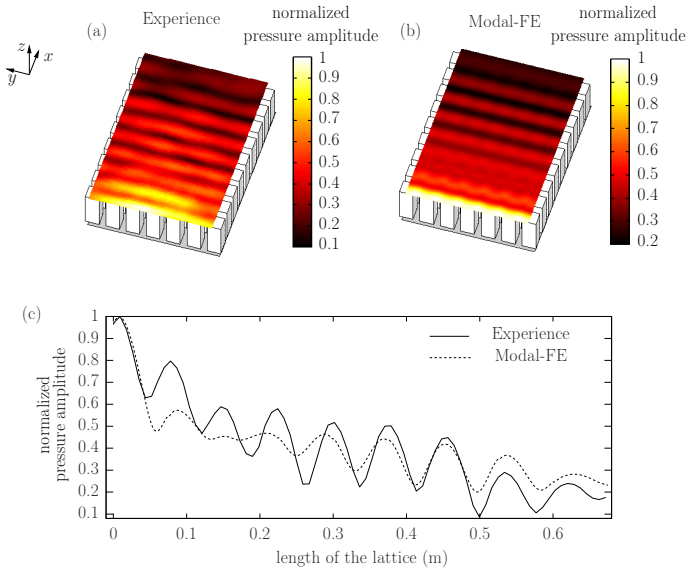


**Figure 4.10**: *a) and b) shows respectively the experimental and numerical horizontal planes of the pressure field at 2 kHz, 1 cm above the lattice. c) averaged pressure in the* $y-$*direction vs.* $x$ *for the measured and the numerical fields.*

## 4.5 Conclusion

We have investigated the propagation of acoustic waves in regular urban areas. The urban area was represented as a periodic lattice of open waveguides. By comparison of this open lattice with a more classical, closed lattice, it has been shown that the band structure for the first propagating mode remains qualitatively the same when opening the upper part of the lattice. The measured transfer functions are also very similar in both cases. Thus, for a study involving only the first mode, the problem could be simplified to a 2D geometry by eliminating the vertical coordinate. In contrast, significant differences between the closed and the open lattice appear when higher order modes are included in the study. As it seems logical, the closed lattice exhibits a more marked presence of propagative modes. However, results have shown that this behaviour can be inverted at some frequencies. Unexpectedly, we found propagative bands in the open lattice that become evanescent in the closed lattice.

# Appendix 4.A. FEM computation of the transverse periodic eigenmodes

The aim of this section is to find the eigenfunctions and eigenvalues of the different cross–sections $S_1, ..., S_4$, shown in Fig. 4.11. For each section, the eigenproblem is written as

$$\left(\frac{\partial^2}{\partial y^2} + \frac{1}{\tau}\frac{\partial}{\partial z}\left(\frac{1}{\tau}\frac{\partial}{\partial z}\right) + \alpha^2\right)\phi(y,z) = 0, \tag{4.13}$$

with the set of boundary conditions

$$\begin{cases} \partial_n\phi(y,z) = 0, \ \forall (y,z) \in \Gamma, \\ \phi(y \in \Gamma_R, z) = \mu_y \phi(y \in \Gamma_L, z), \\ \partial_n\phi(y \in \Gamma_R, z) = -\mu_y \partial_n\phi(y \in \Gamma_L, z), \end{cases} \tag{4.14}$$

where $\alpha, \Gamma, \Gamma_L$ and $\Gamma_R$ represent, respectively, the in-plane wavenumber, perfectly reflecting boundaries, left and right periodic boundaries. For sections $S_1$ or $S_2$, the parameter $\tau$ is defined by Eq. (4.4), while for sections $S_3$ or $S_4$, $\tau = 1$ in the entire cross–section. The problem is discretised using linear triangular elements. The mesh generated satisfies two conditions: firstly, in order to fulfil the periodicity, nodes on $\Gamma_R$ and $\Gamma_L$ must be symmetrical with respect to the vertical axis of symmetry. Secondly, for simplicity, the modal–FE method requires an identical mesh in the matching section $S_1 \cap S_2$ for the OL, or $S_3 \cap S_4$ for the CL [67].

Then, the field $\phi(y,z)$ is developed on the basis of the interpolating polynomials $\psi_n(y,z)$ as

$$\phi(y,z) = \sum_{n=1}^{N} \Phi_n \psi_n = {}^t\vec{\psi}\vec{\Phi}. \tag{4.15}$$

and the discretised problem takes the form

$$\left(\mathbf{K} - \alpha^2\mathbf{M}\right)\vec{\Phi} = \vec{u}, \tag{4.16}$$

where $\mathbf{K}$ and $\mathbf{M}$ are the stiffness and mass matrix, respectively defined by

$$K_{mn} = \int_{S_j} \frac{1}{\tau^2}\left(\frac{\partial\psi_m}{\partial y}\frac{\partial\psi_n}{\partial y} + \frac{\partial\psi_m}{\partial z}\frac{\partial\psi_n}{\partial z}\right)\mathrm{d}y\mathrm{d}z, \tag{4.17}$$

and

$$M_{mn} = \int_{S_j} \psi_m\psi_n \mathrm{d}y\mathrm{d}z. \tag{4.18}$$

The vector $\vec{u}$ is the contribution of the normal velocity at boundaries, which terms $u_n$

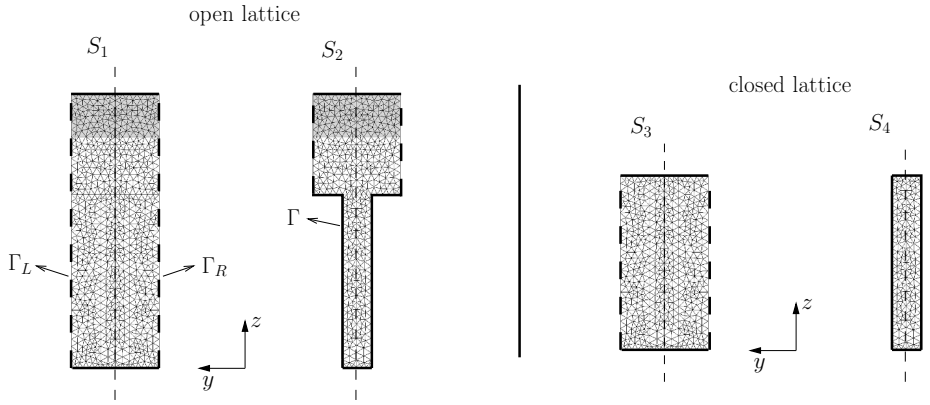


**Figure 4.11***: Meshes examples of the transverse cross–sections. Sections $S_1$ and $S_2$ are the cross–section of the open lattice. Sections $S_3$ and $S_4$ are the cross–sections of the closed one. $\Gamma$ are perfectly reflecting boundaries, represented by continuous thick lines. $\Gamma_L$ and $\Gamma_R$ denote the left and right periodic boundaries, represented by dashed lines.*

are given by

$$u_n = \int_{\Gamma_{tot}} \partial_n \phi \psi_n \mathrm{d}\Gamma_{tot}, \tag{4.19}$$

with $\Gamma_{tot} = \Gamma \cup \Gamma_L \cup \Gamma_R$. From (4.19), it is deduced that this terms are equal to zero for all nodes except for those belonging to the periodic boundaries:

$$\begin{cases} u_n \neq 0, & \text{over } \Gamma_L \text{ and } \Gamma_R \\ u_n = 0, & \text{elsewhere.} \end{cases}$$

For the section $S_4$, completely bounded by rigid walls, one has $\vec{u} = \vec{0}$ and the eigenmodes are found as the eigenvalues and eigenvectors of the matrix $\mathbf{M}^{-1}\mathbf{K}$ (see Eq. (4.16)). For the rest, a similar technique as Allard *et al.* [4] to satisfy the periodic boundary conditions is used. To turn the notation on a more compact form, the matrix $\mathbf{D} = \mathbf{K} - \alpha^2\mathbf{M}$ is defined and Eq. (4.16) is rewritten as

$$\mathbf{D}\vec{\phi} = \vec{u}. \tag{4.20}$$

Following, the problem is arranged so that nodes belonging to $\Gamma_L$ (subscript $L$) appear first, followed by the internal ones (resp. $I$), and finally by those belonging to $\Gamma_R$ (resp. $R$). The reordered problem is written as:

$$\begin{pmatrix} \mathbf{D}_{LL} & \mathbf{D}_{LI} & \mathbf{D}_{LR} \\ \mathbf{D}_{IL} & \mathbf{D}_{II} & \mathbf{D}_{IR} \\ \mathbf{D}_{RL} & \mathbf{D}_{RI} & \mathbf{D}_{RR} \end{pmatrix} \begin{pmatrix} \vec{\Phi}_L \\ \vec{\Phi}_I \\ \vec{\Phi}_R \end{pmatrix} = \begin{pmatrix} \vec{u}_L \\ \vec{0} \\ \vec{u}_R \end{pmatrix}. \tag{4.21}$$

Also, from Eqs. (4.15) and (4.19), the two last boundary conditions of Eq. (4.14) can

be traduced by the vectorial expressions

$$\begin{cases} \vec{\Phi}_R = \mu_y \vec{\Phi}_L \\ \vec{u}_R = -\mu_y \vec{u}_L. \end{cases} \tag{4.22}$$

Next, introducing Eqs. (4.22) into Eq. (4.21) and eliminating $\vec{\Phi}_R$ (or $\vec{\Phi}_L$) leads to the following eigenproblem for the remaining unknowns $\vec{\Phi}_L$ (or $\vec{\Phi}_R$) and $\vec{\Phi}_I$:

$$\mathbf{D}_p \begin{pmatrix} \vec{\Phi}_L \\ \vec{\Phi}_I \end{pmatrix} = \begin{pmatrix} \vec{0} \\ \vec{0} \end{pmatrix}, \tag{4.23}$$

with $\mathbf{D}_p = \mathbf{K}_p - \alpha^2 \mathbf{M}_p =$

$$\left[ \begin{array}{c|c} \mathbf{D}_{LL} + \mu_y \mathbf{D}_{LR} + \mu_y^{-1} \mathbf{D}_{RL} + \mathbf{D}_{RR} & \mathbf{D}_{LI} + \mu_y^{-1} \mathbf{D}_{RI} \\ \hline \mathbf{D}_{IL} + \mu_y \mathbf{D}_{IR} & \mathbf{D}_{II} \end{array} \right]$$

The eigenmodes are given by the eigenvalues $\alpha_n^2$ and eigenvectors $(\vec{\Phi}_L, \vec{\Phi}_I)$ of the matrix $\mathbf{M}_p^{-1} \mathbf{K}_p$. Note that the eliminated unknowns $\vec{\Phi}_R$ can be straightforwardly obtained from Eq. (4.22).

# Chapter 5

# A mono–mode, time domain model for the acoustic propagation in irregular urban areas

## 5.1 Introduction

We have considered until now the propagation of acoustic waves in the frequency domain. However, the urban environment presents usually impulsive or non stationary sources, which require a time domain description of the acoustic field. The goal of this Chapter is to develop a new model for the time domain acoustic propagation in urban areas, as shown in Fig. 5.1.

The time domain modelling of extended urban environments is a difficult task, due in large measure to the huge extension of the propagation domain, making computationally intractable the implementation of conventional numerical methods. Perhaps, this is the reason why the acoustic propagation in such media has been rarely addressed

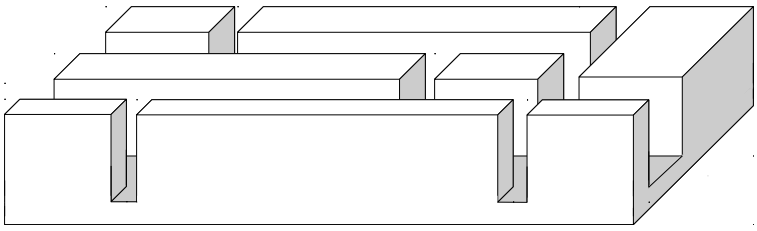

**Figure 5.1***: Irregular urban area.*

in the literature. Albert *et al.* [1, 2] investigated source localisation problems in urban environments using a FDTD approach, although limited to 2D geometries. In a recent work, Hewett [36] used a ray based model to study the propagation of high frequency waves in domains containing several interconnected streets. Due to the similarity with the problem addressed here (a network of interconnected waveguides), one can also mention the work by Depollier *et al.* [21] on a lattice of tubes connected with right–angled junctions.

The new model proposed in this Chapter is based on a previous characterisation, in the frequency domain, of each of the elements forming the network (waveguides and junctions). This characterisation is performed using the modal–FE method and the information obtained is traduced to the time domain using Fourier analysis. In the time domain, spatial discretisation is not required and the problem to solve is one–dimensional: the only unknown is the modal amplitude in the waveguide. Therefore, the model is very efficient numerically. Moreover, the model enables us to take into account the complexity of the medium, namely the modal attenuation and dispersion.

## 5.2 A mono–mode, time domain model

We want to model the acoustic propagation in an irregular urban area as the one illustrated in Fig. 5.1. The proposed model is based on the following assumptions:

- all the streets have identical cross–section and therefore identical modal basis;
- only the mode (0,0) propagates (see Fig. 2.5)
- the interaction between streets due to wave radiation above the buildings can be neglected

Under these assumption, the urban area can be regarded as a 2D network of interconnected waveguides in which only one mode propagates. The mode is characterised by its eigenvector $\vec{\Phi}_{(0,0)}$ and its transverse wavenumber $\alpha_{(0,0)}$, which are computed with FE (Sec. 1.2.1).

### 5.2.1 Propagation in the frequency domain

In each of the waveguides forming the network we define a local longitudinal coordinate, $\chi$, as shown in the Fig. 5.2. Taking into account only the mode (0,0), the acoustic field in the frequency domain is given by

$$\vec{P}(\chi, f) = \vec{\Phi}_{(0,0)} A(\chi, f), \tag{5.1}$$

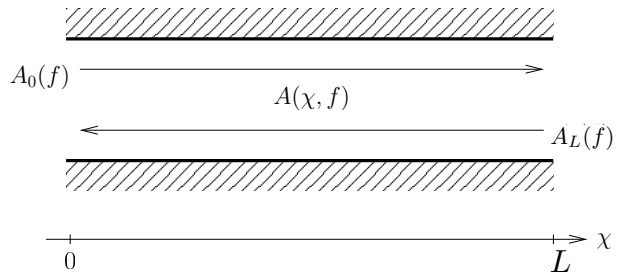


**Figure 5.2***: Definition of the local coordinate $\chi$ in the waveguide.*

where $A(\chi, f)$ is the amplitude of the mode as a function $\chi$ and frequency $f$. This quantity is expressed as

$$A(\chi, f) = A_0(f)e^{\jmath k_\chi \chi} + A_L(f)e^{\jmath k_\chi (L-\chi)}, \tag{5.2}$$

with $L$ the length of the street, $k_\chi = \sqrt{k^2 - \alpha^2_{(0,0)}}$ the propagation constant, $A_0(f)$ the amplitude of the mode at the input section, and $A_L(f)$ the amplitude of the mode at the output section. For street canyons oriented horizontally, $A_0$ (respectively $A_L$) indicates the modal amplitude at the left extremity (respectively, the right extremity). For street canyons oriented vertically, $A_0$ (respectively $A_L$) indicates the modal amplitude at the bottom extremity (respectively, the top extremity).

When the mode arrives to a given intersection, its energy is redistributed towards the segments connected to the junction. In the frequency domain, this process is described by the scattering matrix $\mathbf{S}(f)$ of the junction junction. We consider two types of junctions: a T–intersection, characterised by the matrix $\mathbf{S}_\perp(f)$, and a +–junction characterized by the matrix $\mathbf{S}_+(f)$ (see Fig. 5.3). These matrices are defined as

$$\begin{pmatrix} A_{o,L} \\ A_{o,U} \\ A_{o,R} \end{pmatrix} = \mathbf{S}_\perp \begin{pmatrix} A_{i,L} \\ A_{i,U} \\ A_{i,R} \end{pmatrix}, \tag{5.3}$$

$$\mathbf{S}_\perp = \begin{bmatrix} R_{\perp 1} & T_{\perp 3} & T_{\perp 1} \\ T_{\perp 2} & R_{\perp 2} & T_{\perp 2} \\ T_{\perp 1} & T_{\perp 3} & R_{\perp 1} \end{bmatrix}$$

and

$$\begin{pmatrix} A_{o,L} \\ A_{o,U} \\ A_{o,R} \\ A_{o,B} \end{pmatrix} = \mathbf{S}_+ \begin{pmatrix} A_{i,L} \\ A_{i,U} \\ A_{i,R} \\ A_{i,B} \end{pmatrix}, \tag{5.4}$$

$$\mathbf{S}_+ = \begin{bmatrix} R_+ & T_{+1} & T_{+2} & T_{+1} \\ T_{+1} & R_+ & T_{+1} & T_{+2} \\ T_{+2} & T_{+1} & R_+ & T_{+1} \\ T_{+1} & T_{+2} & T_{+1} & R_+ \end{bmatrix}.$$

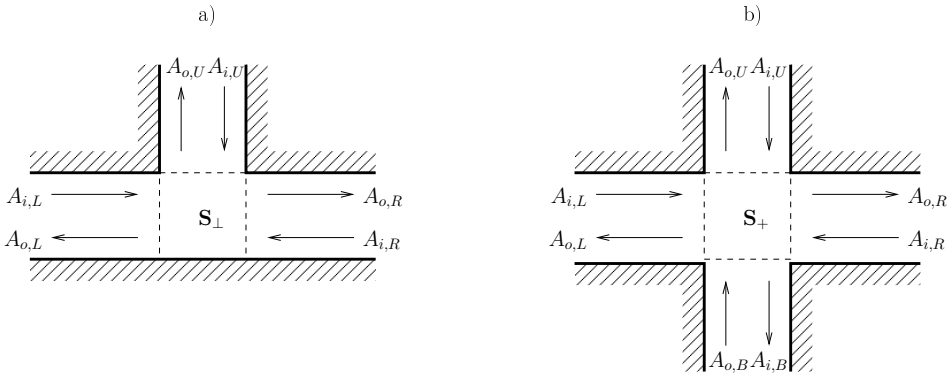


**Figure 5.3***: a) Definition of the scattering matrix of the T–intersection,* $\mathbf{S}_\perp$*. b) Definition of the scattering matrix of the +–intersection,* $\mathbf{S}_+$*.*

In previous equations (5.3) and (5.4), subscripts $i$ and $o$ indicate incident and outgoing waves, respectively, and subscripts $U, B, L$ and $R$ indicate quantities on the upper, bottom, left and right side from the of the intersection. Note that due to the symmetry of the T–junction the scattering matrix $\mathbf{S}_\perp$ has only two different reflection terms $R_{\perp 1}$ and $R_{\perp 2}$, and three transmission terms $T_{\perp 1}$, $T_{\perp 2}$, and $T_{\perp 3}$. Similarly, due to the symmetry of the +–junction the matrix $\mathbf{S}_+$ has only one reflection term $R_{+1}$ and two transmission terms $T_{+1}$ and $T_{+2}$. Note also that the notation in previous equations corresponds to the one used in Fig. 5.3. Of course, although the T–junctions may appear with different orientation, the corresponding scattering matrix would present a similar form.

The terms of these matrices are calculated using the modal–FE method as explained in Appendix 5.A. Fig. 5.4 show the modulus and phase of the terms of the scattering matrix, corresponding to a street canyon with aspect ratio $h/l = 3$ ($h$ and $l$ denotes the height and width of the street). The accident in the curves at $kl/2\pi = 0.07$ is due to the cutoff frequency of the mode, $\mathrm{Re}\{\alpha_{(0,0)}\}$.

### 5.2.2 Propagation in the time domain

The inverse Fourier transform ($\mathrm{FT}^{-1}$) of Eq. (5.2) gives the modal amplitude as a function of time and $\chi$. Given the time convention chosen in this document, $\exp(-\jmath\omega t)$, the $\mathrm{FT}^{-1}$ is defined as

$$g(t) = \mathrm{FT}^{-1}\left\{G(f)\right\} = \int_{-\infty}^{\infty} G(f) e^{-\jmath 2\pi f t} \mathrm{d}f, \tag{5.5}$$

where $G(f)$ denotes any function of $f$. Hence, the $\mathrm{FT}^{-1}$ of Eq. (5.2) is

$$a(\chi, t) = a_0(t) * d(\chi) + a_L(t) * d(L - \chi), \tag{5.6}$$

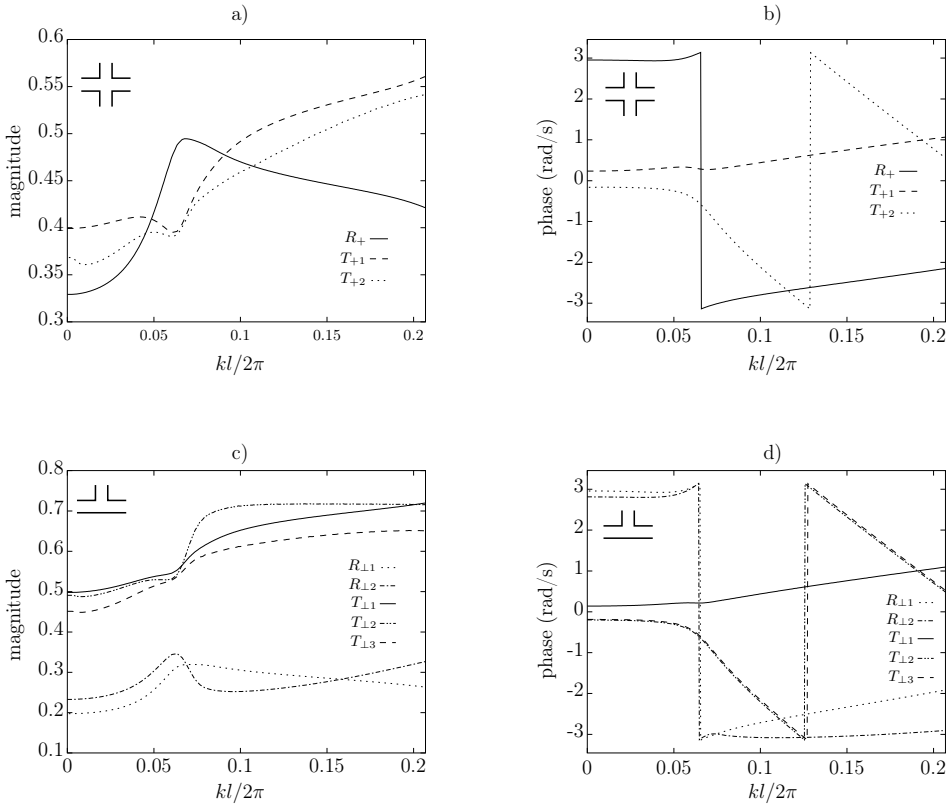


**Figure 5.4***: Terms of the scattering matrices* $\mathbf{S}_+$ *and* $\mathbf{S}_\perp$ *for a street canyon with height to width ratio* $h/l = 3$*. a) and b) represent respectively the magnitude and phase of the terms of* $\mathbf{S}_+$*. c) and d) represent respectively the magnitude and phase of the terms of* $\mathbf{S}_\perp$*.*

where '$*$' denotes the convolution product, $a_0(t) = \mathrm{FT}^{-1}\{A_0(f)\}$, $a_L(t) = \mathrm{FT}^{-1}\{A_L(f)\}$ and $d(\chi) = \mathrm{FT}^{-1}\left\{e^{\jmath k_\chi \chi}\right\}$. The quantities $a_0(t)$ and $a_L(t)$ are the modal amplitude at the input and output of the street, as a function of time. The term $d(\chi)$ represents the impulse response of the urban canyon, which takes into account the dispersion and dissipation of the mode through the propagation constant $k_\chi$.

To fix ideas, let us consider the propagation of a non–dispersive, plane mode such that $k_\chi = \omega/c_0$. For a right–going mode, one has

$$d(\chi) = \mathrm{FT}^{-1}\left\{e^{\jmath k_\chi \chi}\right\} = \delta(T - \chi/c_0), \tag{5.7}$$

which represents simply a time shift of the amplitude $a_0(t)$ on the left extremity. However, in the case of the fundamental mode of the urban canyon considered here, the propagation constant is $k_\chi = \sqrt{k^2 - \alpha^2_{(0,0)}}$, with $\alpha_{(0,0)} \in \mathbb{C}$, which represents a dispersive and dissipative mode (see Sec. 5.3 below).

The impulse response of the intersections, $\mathbf{s}_\perp(t)$ and $\mathbf{s}_+(t)$, are obtained as the inverse Fourier transform of Eqs. (5.3) and (5.4),

$$\begin{pmatrix} a_{o,L} \\ a_{o,U} \\ a_{o,R} \end{pmatrix} = \mathbf{s}_\perp * \begin{pmatrix} a_{i,L} \\ a_{i,U} \\ a_{i,R} \end{pmatrix}, \tag{5.8}$$

$$\mathbf{s}_\perp = \begin{bmatrix} r_{\perp 1} & \tau_{\perp 3} & \tau_{\perp 1} \\ \tau_{\perp 2} & r_{\perp 2} & \tau_{\perp 2} \\ \tau_{\perp 1} & \tau_{\perp 3} & r_{\perp 1} \end{bmatrix},$$

and

$$\begin{pmatrix} a_{o,L} \\ a_{o,U} \\ a_{o,R} \\ a_{o,B} \end{pmatrix} = \mathbf{s}_+ * \begin{pmatrix} a_{i,L} \\ a_{i,U} \\ a_{i,R} \\ a_{i,B} \end{pmatrix}, \tag{5.9}$$

$$\mathbf{s}_+ = \begin{bmatrix} r_+ & \tau_{+1} & \tau_{+2} & \tau_{+1} \\ \tau_{+1} & r_+ & \tau_{+1} & \tau_{+2} \\ \tau_{+2} & \tau_{+1} & r_+ & \tau_{+1} \\ \tau_{+1} & \tau_{+2} & \tau_{+1} & r_+ \end{bmatrix}.$$

Now that we have characterised each of the elements separately, it is necessary to perform an iterative process permitting to compute the multiple wave scattering in the network. This process is sketched in Fig. 5.5. Step 1 consist in defining the source conditions $a_0^{(j)}$ and $a_L^{(j)}$ for each street, whith $j = 1, 2, \cdots, N_s$, and $N_s$ the number of streets. Following, in step 2, the field along the streets is computed from using Eq. (5.6). In step 3, the wave scattering at junctions is computed from the incident fields, using Eqs. (5.8) and (5.9). Steps 2 and 3 are iterated as many times ($N_t$) as desired, using

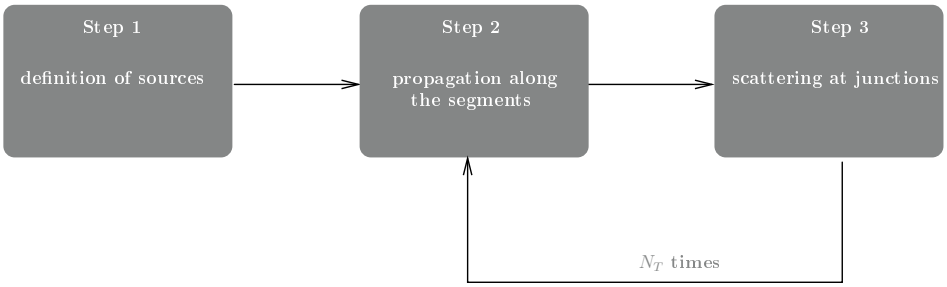


**Figure 5.5**: *Iterative process to compute the pressure field.*

the output modal amplitudes in Step 3 at iteration $n$ as the source conditions in Step 2 at iteration $n + 1$.

## 5.3 Examples

### A single street

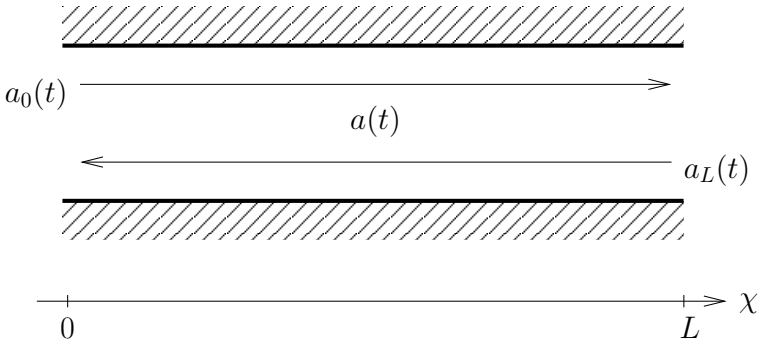


**Figure 5.6**: *A single street canyon with length L.*

The simplest possible case consists in a domain composed of a single street, as shown in the Fig. 5.6. The dimensions of the street are $h = 15$ m, $l = 5$ m and $L = 350$ m. With this parameters, the cutoff frequency of the first mode is $f_{(0,0)} = 4.5$ Hz. The amplitude of this mode along the street is given by

$$a(\chi, t) = a_0(t) * d(\chi) + a_L(t) * d(L - \chi). \tag{5.10}$$

In step 1 (see Fig. 5.5) we define the source conditions $a_0(t)$ and $a_L(t)$. We consider a source only on the left extremity ($a_L(t) = 0$). The source emits a Gaussian wave packet,

$$a_0(t) = \sin(2\pi f_s t) \exp(-(T - t_0)/\sigma), \tag{5.11}$$

with $f_s = 8$ Hz the central frequency, $t_0 = 1$ s and $\sigma = 0.0025$ s$^{-1}$. Figures 5.7.a and 5.7.b show respectively the source condition $a_0(t)$ and its spectrum $A_0(f) = \mathrm{FT}\{a_0(t)\}$.

In step 2 the modal amplitude amplitude in the canyon $a(\chi, t)$ is computed from $a_0(t)$ as

$$a(\chi, t) = a_0(t) * d(\chi). \tag{5.12}$$

The process can be stopped after this step, as there is no any scattering element in the domain.

The Fig. 5.8 shows the modal amplitude in the canyon at instants $t = 1.20$ s, $t = 1.58$ s and $t = 1.93$ s. We observe the attenuation and dispersion of the wave packet the propagation. As mentioned before, this phenomenon is described by the term $d_\chi$. The modulus of the frequency response of $e^{\jmath k_\chi \chi}$ is superposed to the spectrum of the source $a_0$ in Fig. 5.7. The dashed lines indicate the frequency responses for $\chi = 5, 50$ and 250 m. Notice that as the pulse propagates, the street behaves similarly to a high–pass filter with cutoff frequency $f_{(0,0)}$

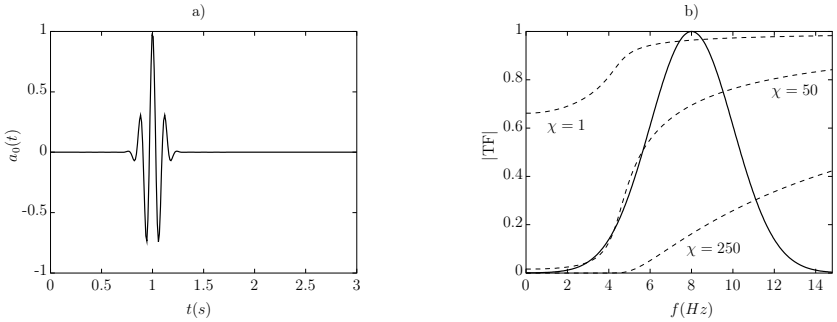


**Figure 5.7***: a) Gaussian wave packet used as a source condition, $a_0(t)$. b) Modulus of the spectrum of the source condition $A_0(f) = FT\{a_0(t)\}$ (solid line). The source condition is filtered by the frequency response of the street,* $\exp(\jmath k_\chi \chi)$*. Dashed lines represent the modulus of this response for $\chi = 5$ m, $\chi = 50$ m and $\chi = 250$ m.*

## Scattering at a single intersection

Consider now a domain composed by three street canyons, connected with a T–intersection, as shown in the Fig. 5.9. The dimensions of each street are identical to the ones used in the previous example of Sec. 5.3. Following, the computation of the modal amplitudes in each street is explained step by step, as indicated in Sec. 5.2.2.

Coming back to step 1, we consider again a single source on the left extremity of the left inferior waveguide, $a_0^{(1)} = \sin(2\pi f_s t)\exp(-(T - t_0)/\sigma)$, and $a_L^{(1)} = a_0^{(2)} = a_L^{(2)} = a_0^{(3)} = a_L^{(3)} = 0$ for the rest of waveguides.

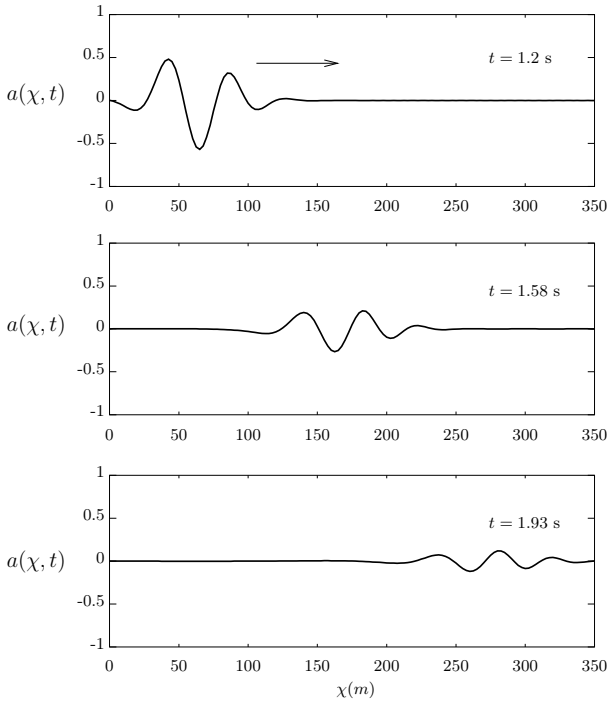


**Figure 5.8***: Modal amplitude versus $\chi$ at different times.*

In step 2, these source conditions are used to compute the modal amplitude along each of the canyons. One has

$$a^{(1)} = a_0^{(1)} * d(\chi), \tag{5.13}$$

$$a^{(2)} = 0, \tag{5.14}$$

$$a^{(3)} = 0. \tag{5.15}$$

In step 3, the scattering at the intersection is computed from the incident fields using Eq. (5.8). Since in this case the only incident wave is the one arriving from the left canyon, the scattered modal amplitudes are given by

$$\begin{pmatrix} a_{o,L} \\ a_{o,U} \\ a_{o,R} \end{pmatrix} = \mathbf{s}_\perp * \begin{pmatrix} a_{i,L} \\ 0 \\ 0 \end{pmatrix}, \tag{5.16}$$

where the incident field is in this case $a_{i,L} = a_0^{(1)} * d(L)$. Next, output fields $a_{o,L}, a_{o,U}, a_{o,R}$ are used as the source conditions $a_0^{(1)'}$, $a_L^{(2)'}$ and $a_0^{(1)'}$ for the next iteration,

$$a_0^{(1)'} = a_{o,L} = a_0^{(1)} * d(L) * r_{\perp 1},$$

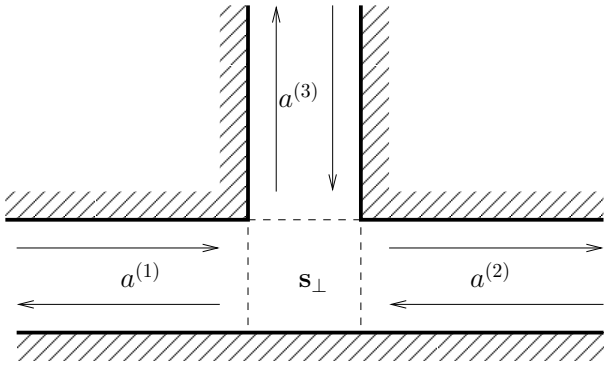


**Figure 5.9***: Domain consisting of 3 urban canyons connected with a T–intersection.*

$$a_L^{(2)'} = a_{o,R} = a_0^{(1)} * d(L) * \tau_{\perp 1},$$
$$a_0^{(1)'} = a_{o,U} = a_0^{(1)} * d(L) * \tau_{\perp 2}.$$

In the next iteration the field is computed along the street canyons using the new source conditions obtained previously,

$$a^{(1)} = a_0^{(1)'} * d(\chi), \tag{5.17}$$
$$a^{(2)} = a_L^{(2)'} * d(L-\chi), \tag{5.18}$$
$$a^{(3)} = a_0^{(3)'} * d(\chi). \tag{5.19}$$

The process can be stopped after this step, as there is no any scattering element in the domain. The process explained above is illustrated in Fig. 5.10.

## Multiple scattering in a domain containing 2 intersections

Consider a composed of 5 streets connected with two T–intersections, Fig. 5.11. The only source is located on street 1. The process in this case gets more complex than in previous cases, due to the higher number of canyons and to the multiple scattering generated by the two intersections. For the sake of clarity, we describe only how to calculate the modal amplitude at the input of the street 3, $a_0^{(3)}$, as a function of the source in street 1, $a_0^{(1)}$.

Tracing the multiple paths that the wave emitted in street 1 must follow to reach

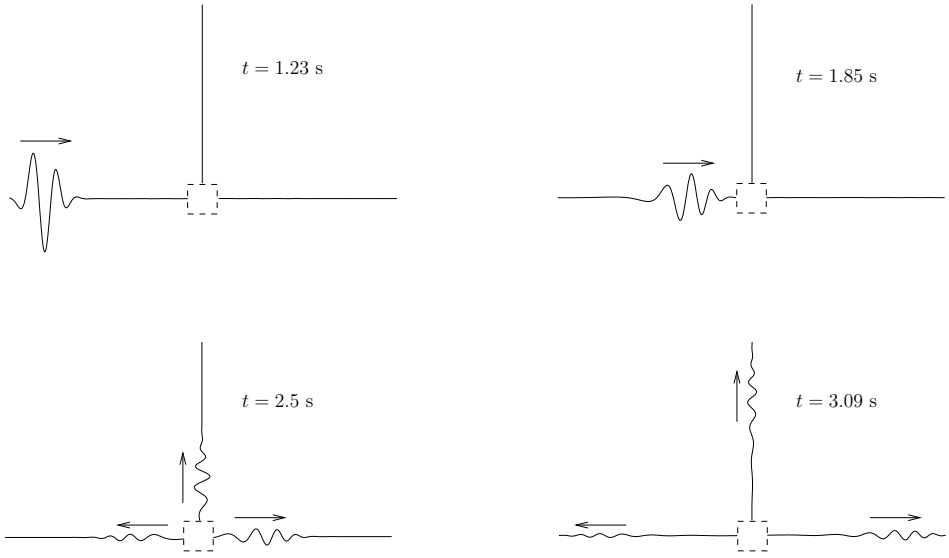


**Figure 5.10***: Wave scattering at the T–intersection.*

street 3 (see Fig. 5.11), enables us to write an expression of $a_0^{(3)}$ as

$$a_0^{(3)} = \overbrace{a_0^{(1)} * d_L * \tau_{\perp 1} * d_L * \tau_{\perp 1}}^{\text{term 1}} + \overbrace{a_0^{(1)} * d_L * \tau_{\perp 1} * d_L * r_{\perp_1} * d_L * r_{\perp 1} * d_L * \tau_{\perp 1}}^{\text{term 2}} + \overbrace{a_0^{(1)} * d_L * \tau_{\perp 1} * d_L * r_{\perp_1} * d_L * r_{\perp 1} * d_L * r_{\perp 1} * d_L * r_{\perp 1} * d_L * \tau_{\perp 1}}^{\text{term 3}} + \cdots \tag{5.20}$$

Due to the radiative losses ($\mathrm{Im}\{\alpha_{(0,0)}\}$) and the wave radiation towards the side streets, the sum (5.20) converges after a finite number of iterations. Recalling that at each iteration the propagation along a street and the scattering at junctions is computed once (see Fig. 5.5), we see that the first term of the Eq. (5.20) is obtained after 2 iterations, the term 2 is obtained after 4 iterations, the term 3 after 6 iterations, and so on.

In order to evaluate the convergence of Eq. (5.20), Fig. 5.12 shows $a_0^3$ as a function of the number of iterations. The influence of the second term is visible after $t \approx 1.5$ s, where the curve corresponding to 2 iterations differs from that corresponding to 4 iterations. Then, we observe that the results for 4 or 6 iterations are almost identical. This means that the series in Eq. (5.20) can be truncated after the second term, as the subsequent echoes arriving to street 3 have very weak amplitude.

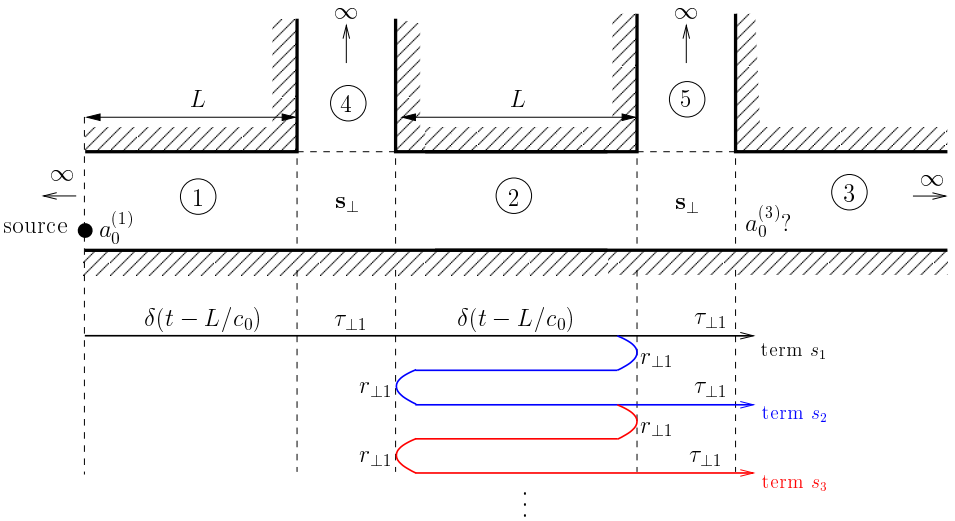


**Figure 5.11**: *System containing 2 T–intersections. The arrows below indicate the paths of the multiple reflections arriving to street 3.*

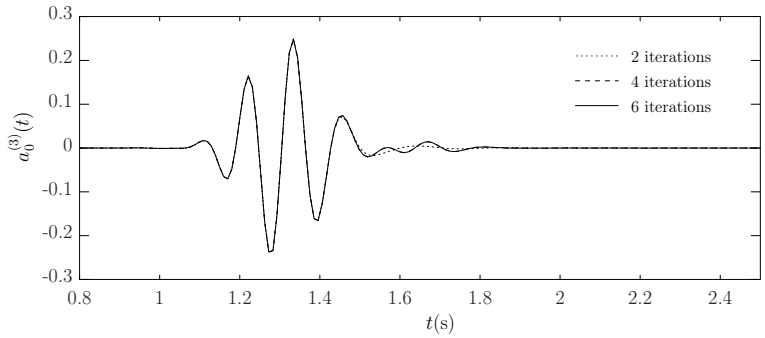


**Figure 5.12**: *Transmitted modal amplitude, $a_0^{(3)}$, as a function of the number of interations: 2 iterations (dotted line), 4 iterations (dashed line), and 6 iterations (solid line).*

## Urban area

A last example is shown to illustrate the acoustic propagation in the urban area considered initially in Fig 5.1. The dimensions of the transverse sections of the canyons are $l = 10$ m and $h = 30$ m. The length of the streets varies between 40 m, 80 m and 120 m. The total extension of the urban area in the horizontal plane is $390 \times 220$ m$^2$. The source is located at the upper left street, and emits a Gaussian wave packet with central frequency 6 Hz. Fig. 5.13 shows snapshots of the pressure field at $t = 2$ s, $t = 2.5$ s, and $t = 3$ s. The result was obtained performing 20 iterations.

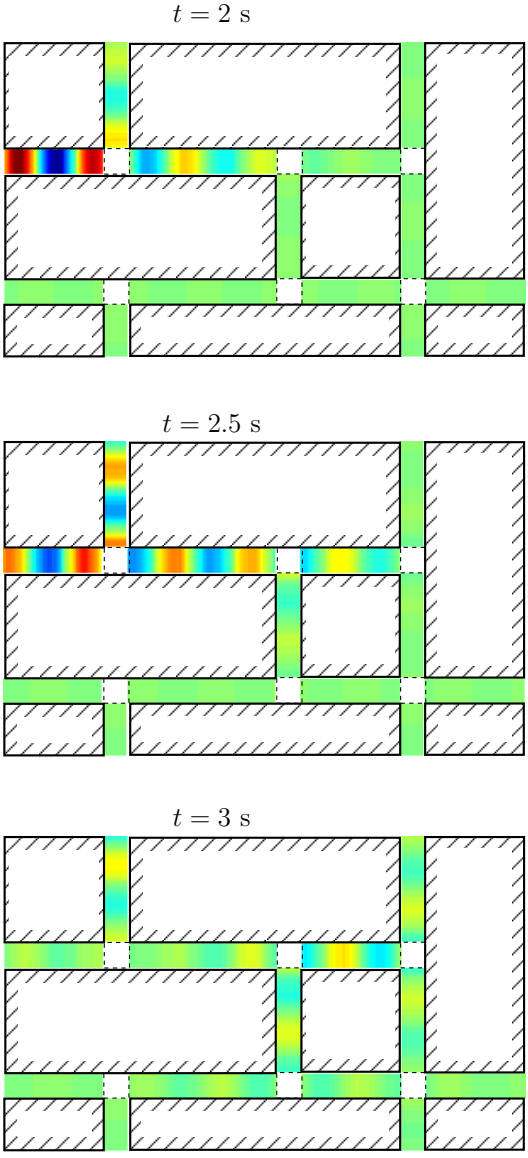


**Figure 5.13**: *Pressure field in the urban area at $t = 2$ s, $t = 2.5$ s, and $t = 3$ s.*

# Appendix 5.A. Computation of the scattering matrices

The terms of the scattering matrix relating quantities in the axial direction ($R_{\perp 1}$, $R_{\perp 2}$, $T_{\perp 1}$, $R_{+}$, $T_{+1}$) can be computed straightforwardly with the modal–FE method, see Chapter 1. However, the terms relating the modal amplitudes in perpendicular streets ($T_{\perp_2}$, $T_{\perp_3}$, $T_{+2}$) cannot be calculated directly with this method, since the acoustic field field in the perpendicular street is not expressed on the basis of its eigenmodes. In the following we explain how to compute the term $T_{\perp_2}$ of matrix $\mathbf{S}_{\perp}$ (the terms $T_{\perp_3}$ and $T_{+2}$ can be obtained in a similar way).

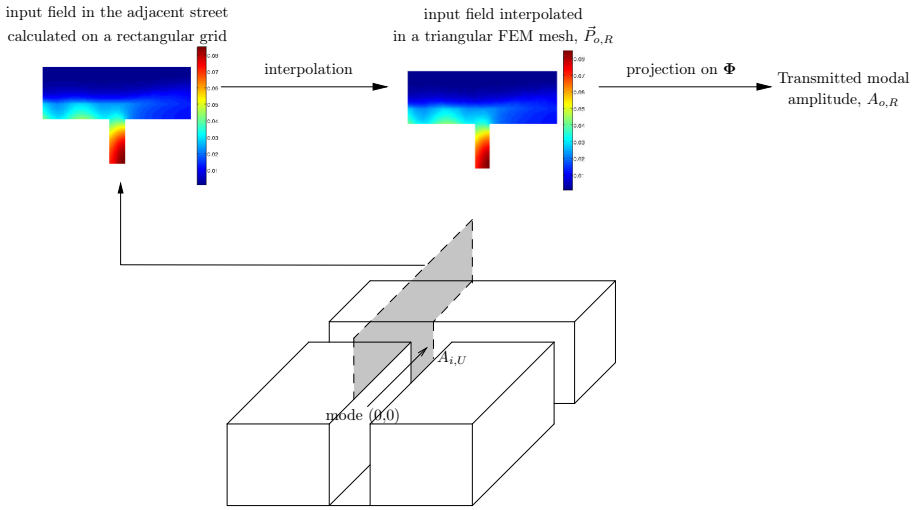


**Figure 5.14**: *Computation of the term $T_{\perp_2}$.*

We use a similar technique to the one explained in the Sec. 1.1.5 for 2D intersections. The pressure field is computed in the domain using mode (0,0) as incident field. The incident modal amplitude is $A_{i,U}$ (see Figs. 5.14 and 5.3). The resulting pressure field at the input of the adjacent street (shaded area in Fig. 5.14) is interpolated in the triangular FEM mesh. Hence, if the pressure in the FEM mesh is $\vec{P}_{o,R}$ and the modal basis of the transverse section is $\mathbf{\Phi}$, the amplitude of the transmitted modes $\vec{A}_{o,R}$ can be computed as

$$\vec{A}_{o,R} = \mathbf{\Phi}^{-1}\vec{P}_{o,R}. \tag{5.21}$$

Doing this for all frequencies and keeping only the term $A_{o,R}$ of $\vec{A}_{o,R}$, corresponding to the first mode, gives the transmission coefficient as $T_{\perp_2} = A_{o,R}/A_{i,U}$.

# Chapter 6

# Controlling the absorption and reflection of noise barriers using metasurfaces

## 6.1 Introduction

The last decade has witnessed an increasing interest in the field of acoustic metamaterials. These materials are defined as artificial structured materials in which the presence of resonances leads to an unprecedented control on wave propagation [18]. The goal of this chapter is to investigate the use of metasurfaces (*i.e.* two-dimensional versions of metamaterials) to design noise barriers with advanced acoustic properties.

Most developments on noise barriers have focused on the influence of the head piece in the barrier performance [7, 43, 58], aiming to extend as much as possible the shadow region behind de barrier; or in developing active control techniques [24]. Here we show that the use of metasurfaces enables us to obtain some unconventional properties that cannot be achieved with previous designs.

This study is inspired by recent developments in the field of electromagnetic metasurfaces [78–80]. These devices are composed of resonant RCL circuits and provide an enhanced control on the directivity of emitting antennas. These properties arises from the excitation of resonances in the RCL circuits, which creates a strong dispersion of the surface waves propagating on the device. In the present work the RCL circuits are replaced by C–resonators, Fig. 6.1. As we explain in the following, the presence of local resonances in this structure modifies the dispersion characteristics of the acoustic surface waves, giving us the possibility to control de direction of the reflected waves.

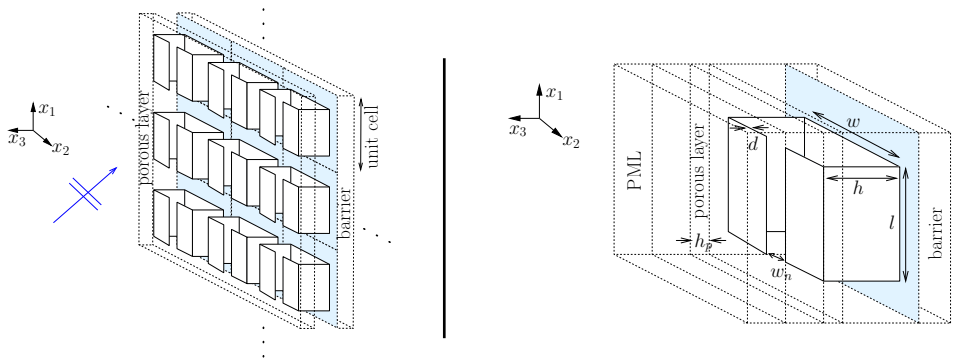


**Figure 6.1***: Left, metasurface composed of an array of C–resonators. Right, the corresponding unit cell.*

Moreover, it has been demonstrated that an absorbing material backed with an irregular surface presents enhanced absorption properties compared to the same material backed with a flat surface [26, 29, 31, 32]. In particular, through the excitation of resonances on the backing surface it is possible to achieve perfect absorption peaks at frequencies below the quarter–wavelength resonance of the absorbing layer, where the single porous material fails [31, 32]. In this Chapter, we demonstrate this behaviour combining local resonances on the metasurface and an absorbing layer.

## 6.2 Numerical modeling

The geometry of the problem is illustrated in the Fig. 6.1. It consists on a periodic arrangement of C-resonators disposed over a flat surface. The resonators are covered with a porous layer with thickness $h_p$. The spatial period in the horizontal directions is denoted by $D$. The geometry of the resonator is defined by its height $h$, length $l$, width $w$, the neck width $w_n$ and the wall thickness $d$.

### 6.2.1 Porous material modeling

The porous material is modelled using the 5 parameters Johnson-Champoux-Allard equivalent fluid model [3, 17, 47]. The equivalent speed of sound is defined as $c_{eq} = (\rho_{eq} K_{eq})^{-1/2}$ where $\rho_{eq}$ and $K_{eq}$ are respectively the dynamic density and compressibility,

| $\sigma(\mathrm{N}\cdot\mathrm{s}\cdot\mathrm{m}^4)$ | $\varphi$ | $\alpha_\infty$ | $\Lambda(\mathrm{m}^{-6})$ | $\Lambda'(\mathrm{m}^{-6})$ |
|---|---|---|---|---|
| 25000 | 0.98 | 1.02 | 90 | 180 |

**Table 6.1***: Parameters of the porous material.*

$$\frac{1}{K_{eq}} = \frac{\gamma P_0}{\varphi\left(\gamma - (1-\gamma)\left(1 + \jmath\frac{\omega_c}{P_r\omega}G(P_r\omega)\right)^{-1}\right)}, \tag{6.1}$$

$$\rho_{eq} = \frac{\rho_0\alpha_\infty}{\varphi}\left(1 + \jmath\frac{\omega_c}{\omega}F(\omega)\right), \tag{6.2}$$

with $\omega_c = \sigma\varphi/\alpha_\infty\rho_0$ the biot frequency, $\gamma$ the specific heat ratio, $P_0$ the atmospheric pressure, $P_r$ the Prandtl number, $\varphi$ the porosity, $\alpha_\infty$ the tortuosity and $\sigma$ the flow resistivity. The correction functions $G(P_r\omega)$ and $F(\omega)$ are given by

$$G(P_r\omega) = \sqrt{1 - \jmath\eta\rho_0 P_r\omega\left(\frac{2\alpha_\infty}{\sigma\varphi\Lambda'}\right)^2}, \tag{6.3}$$

$$F(\omega) = \sqrt{1 - \jmath\eta\rho_0\omega\left(\frac{2\alpha_\infty}{\sigma\varphi\Lambda}\right)^2}. \tag{6.4}$$

In previous Eqs. (6.3) and (6.4), $\eta$ is the viscosity of the fluid, $\Lambda'$ is the thermal characteristic length and $\Lambda$ is the viscous characteristic length. The material employed for the study is a Fireflex foam, which parameters are given in Tab. 6.1.

### 6.2.2 Band structure and absorption coeffcient

The modal–FE method is used to model the wave propagation in the unit cell represented in the Fig. 6.1. Considering normal incidence, $x_3$ is the longitudinal coordinate and $x_1$ and $x_2$ are the transverse coordinates. The problem to solve is in this case,

$$\left(\frac{\partial^2}{\partial x_1^2} + \frac{\partial^2}{\partial x_2^2} + \frac{\partial^2}{\partial x_3^2} + \left(\frac{\omega}{c}\right)^2\right)p(x_1, x_2, x_3) = 0, \tag{6.5}$$

where $c$ is the sound speed in the unit cell, $c = c_{eq}$ in the porous layer and $c = c_0$ elsewhere. Additionally, the field must fulfil rigid boundary conditions at walls, $\partial_n p = 0$, and periodic boundary conditions on lateral boundaries, given by

$$p(x_1, x_2 + mD, x_3) = \mathrm{e}^{\jmath m k_{x2} D}p(x_1, x_2, x_3), \tag{6.6}$$

$$p(x_1, x_2, x_3 + nD) = \mathrm{e}^{\jmath n k_{x3} D}p(x_1, x_2, x_3). \tag{6.7}$$

For the computation of the surface waves band structure, $x_1$ is the longitudinal coordinate and $x_2$ and $x_3$ are the transverse coordinates. In this case, we use a PML accounting for the wave radiation in the $x_3$ direction. The equation to solve is then given by

$$\left(\frac{\partial^2}{\partial x_1^2}+\frac{\partial^2}{\partial x_2^2}+\frac{1}{\tau}\frac{\partial}{\partial x_3}\left(\frac{1}{\tau}\frac{\partial}{\partial x_3}\right)+\left(\frac{\omega}{c}\right)^2\right)p(x_1,x_2,x_3)=0, \tag{6.8}$$

where $\tau$ is the PML absorbing parameter.

## 6.3 Control of absorption

The aim of this section is to evaluate the absorption properties of the barrier as a function of the height of the resonators, $h$. The rest of parameters are fixed to $D = 50$ cm, $w = 40$ cm, $l = 40$ cm, $w_n = 4$ cm, $d = 4$ cm and $h_p = 10$ cm. An incident plane wave traveling normal to the surface is considered. The absorption coefficient is defined as $A = 1 - R$, with $R = W_r/W_i$ the energy reflection coefficient, calculated as the ratio of the reflected intensity flux $W_r$ to the incident intensity flux $W_i$.

The top panel in Fig. 6.2 shows the evolution of $A$ for$h = 10$ cm, $h = 20$ cm and $h = 30$ cm. For comparison, two reference solutions are also plotted (bottom graph of Fig. 6.2). One is a porous layer of similar thickness $h_p$ backed with a rigid wall. The other one is the same porous layer backed with an air layer of thickness $h$, and backed by a rigid wall. We observe an absorption peak that reaches more that 80% at frequencies well below the quarter wavelength resonance of the porous layer. The peak frequency is shifted from 500 Hz ($h = 10$ cm) to 370 Hz ($h = 30$ cm).

## 6.4 Control of reflection

Figure 6.3 shows the band structure for waves traveling parallel to the $(x_1, x_2)$-plane with an angle $\theta_1 = 50°$ with respect to the $x_1$-axis. Only the propagative components of the Bloch wavenumber are represented, $\mathrm{Re}\{k_B\}$. The sound line, $k = k_B/\cos(\theta_1)$, divides the dispersion relation in two parts. Modes bellow the sound line represent acoustic surface waves, which are evanescent in the $x_3$-direction, and are therefore bounded to the surface. Modes above the sound line are propagative along the $x_3$-direction, and are therefore called radiative modes. The former of interest for us, as they can couple to an incident plane wave impinging the metasurface perpendicularly.

The three curves in Fig. 6.3 correspond to $h = 20$ cm, $h = 25$ cm and $h = 30$ cm. We observe that the dispersion relation of the radiative modes varies with $h$. In the following we see how the excitation of the radiative modes modifies the waves reflected on the metasurface.

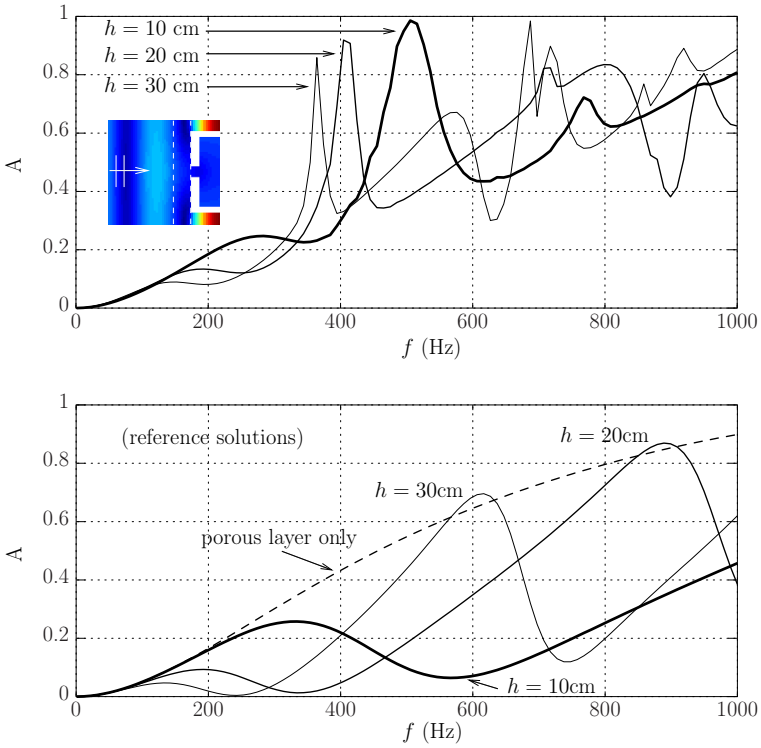


**Figure 6.2**: *Top, absorption coefficient at normal incidence for $h = 10$ cm, $h = 20$ cm and $h = 30$ cm. The inset show the acoustic field at resonance. Bottom, reference solutions. The dashed line represents the absorption coefficient of the porous layer backed with a rigid wall. The solid lines corresponds to the porous layer backed with an air layer of thickness $h = 10$ cm, $h = 20$ cm and $h = 30$ cm, and backed with a rigid wall.*

The left, central, and right panel in Fig. 6.4 represent the acoustic fields for $h = 20$ cm, $h = 25$ cm and $h = 30$ cm, respectively. The impinging wave is a Gaussian beam with incidence angle $\theta_1 = 50°$ with respect to $x_1$ and $\theta_2 = 35°$ with respect to axis $x_2$. At the excitation frequency, $f = 385$ Hz, the metasurface presents radiative modes for $h = 20$ cm and $h = 25$ cm (see Fig. 6.3). Hence, we observe the interaction of the incident beam with these radiative modes in the corresponding acoustic fields. An interesting aspect is that the wave vector of the radiative modes is directed towards the negative $x_1$ direction [78–80], meaning that the energy which is coupled to these modes is reflected with a negative angle (*i.e.*, in the same direction as the incident beam). The interference patterns in the acoustic fields of the left and central panels demonstrate this behaviour. For $h = 30$ cm (right panel in Fig. 6.4), no radiative modes exist at the excitation frequency (see dashed line in Fig. 6.3), so that the beam is reflected in the usual way. This result demonstrates that the excitation of radiative modes on the metasurface can be used to control the wave reflection.

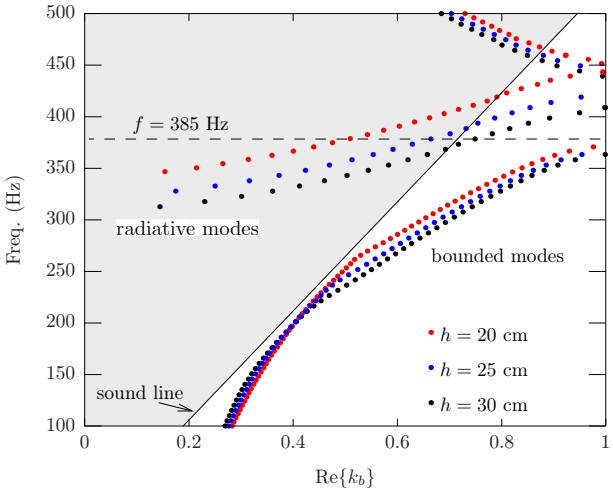


**Figure 6.3**: *Band structure of waves propagating parallel to the periodic plane with an angle $\theta_1 = 50°$ with respect to the $x_1$-axis.*

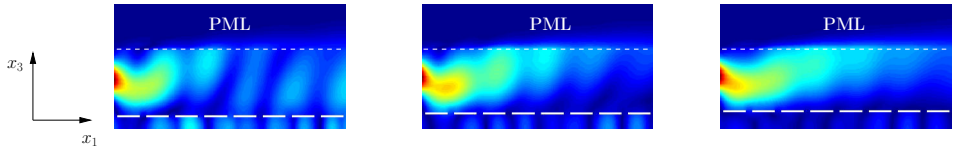


**Figure 6.4**: *From left to right, wave fields for $h = 20$ cm, $h = 25$ cm, and $h = 30$ cm. The incidence angle is $\theta_1 = 50°$ and $\theta_2 = 35°$ at frequency $f = 385$ Hz.*

## 6.5 Conclusion

This Chapter has presented a preliminary study on the use of metasurfaces to control the reflection and absorption of waves by noise barriers. Combining local resonances on the metasurface with an absorbing material, it is possible to achieve very high absorption at frequencies below the quarter–wavelength resonance of the absorbing material. Moreover the presence of local resonances creates radiative modes in the surface waves dispersion relation, the excitation of which enables us to control the waves reflected on the metasurface. Although this study is at an early stage, the results exposed in this Chapter may provide ideas to design noise barriers with novel and enhanced acoustic properties.

# Conclusions and perspectives

We conclude this dissertation with a summary of the main results and ideas for future work.

In Chapter 1, we have introduced the modal–FE method and its application to the modelling of right–angled intersections. The implementation of the method is divided in three main steps: (i) the original, open geometry is substituted with an equivalent, closed waveguide; (ii) the transverse eigenmodes of the resulting waveguide are computed with FE and introduced in a multimodal description of the acoustic propagation in the longitudinal direction, (iii) The unknown modal amplitudes are calculated using impedance matrix method. This method combines the versatility of the FEM, making it possible to deal with complicated geometries and boundary conditions, and the ability of the multimodal method to provide a good physical understanding of the studied problem.

Taking advantage of these features, we have investigated wave phenomena arising in specific urban urban configurations. In Chapter 2, we have studied the interaction between the leaky modes propagating on the street and resonances in an adjacent inner yard. It has been demonstrated that inner yards, supposedly protected from the urban noise, may present significantly high pressure levels due to the excitation of its acoustic resonances. Moreover, the courtyard resonances attenuates significantly the acoustic field propagating on the street. Remarkably, this phenomenon occurs even in the absence of a façade opening connecting the courtyard to the street, although only at the fundamental courtyard resonance.

After introducing the basic principles of wave propagation in periodic media in Chapter 3, we have investigated the acoustic propagation in periodic urban areas in Chapter 4. We accomplished this implementing periodic boundary conditions in the modal–FE method and using a scattering matrix approach. The effects of radiative losses, an essential characteristic of the urban environment, has been studied in detail comparing the dispersion relation of the open lattice (representing the urban area) to that of a closed lattice. It was found that the number of propagative modes is in general

smaller in the open lattice, which is attributed to radiative losses. However, we have seen that there exists evanescent bands in the closed lattice that become propagative bands in the open lattice.

In Chapter 5 we have developed a monomode, time domain model for the acoustic propagation modelling in an irregular urban area, regarded as a network of interconnected waveguides. The model is based on a prior characterisation in the frequency domain of each of the elements forming the network (waveguides and junctions). This characterisation is performed using the modal–FE method and the information obtained is traduced to the time domain using Fourier analysis. In the time domain, the method does not require spatial discretisation and the problem reduces to obtaining the modal amplitude within the urban canyons. Therefore, the model is very efficient numerically. Despite its relative simplicity and low computational costs, the model takes into account the essential characteristics of the propagation media, as radiative losses and wave dispersion.

The general conclusion coming out from this work is that, despite the presence of important radiative losses in the propagation media, significant interference and resonance effects are still observed. Not only this result highlights the importance of a wave approach to describe accurately low frequency urban acoustic fields, but it suggest the potential use of these phenomena for controlling the acoustic propagation in urban environments.

The strong interference phenomena reported in this work may motivate the study of additional wave phenomena in different urban configurations. For instance, it is interesting to investigate the coupling between multiple resonant courtyards. Also, adding heterogeneities in a regular urban area may induce localised modes of sound [51, 91]. Understanding and exploiting these phenomena may provide ideas to improve the sound environment at low frequencies.

The time domain model developed in Chapter 5 opens several perspectives for future work. After incorporating higher order modes to the model, it would be interesting to investigate the influence of distinct aspects of the urban morphology in the acoustic propagation, as the building's shape and size, the effect of disorder or the density of buildings. Moreover, the model could be used to extract time indicators in order to characterise acoustically the urban area, as the impulse response or the reverberation time.

Finally, the preliminary results obtained in Chapter 6, together with the rapid developments in the field of acoustic metamaterials and metasurfaces, enables us to foresee the design of noise barriers with new properties and enhanced performance.

# References


[1] Albert, D. G., and Liu, L. The effect of buildings on acoustic pulse propagation in an urban environment. *J. Acoust. Soc. Am. 127*, 3 (2010), 1335–1346.

[2] Albert, D. G., Liu, L., and Moran, M. L. Time reversal processing for source location in an urban environment. *J. Acoust. Soc. Am. 118*, 2 (2005), 616–619.

[3] Allard, J.-F., and Atalla, N. *Propagation of sound in porous media. Modelling sound absorbing materials.* Wiley,New York, 2009.

[4] Allard, J.-F., Dazel, O., Gautier, G., Groby, J.-P., and Lauriks, W. Prediction of sound reflection by corrugated porous surfaces. *J. Acoust. Soc. Am. 129*, 4 (2011), 1696–1706.

[5] Amir, N., Pagneux, V., and Kergomard, J. A study of wave propagation in varying cross-section waveguides by modal decomposition. Part ii. results. *J. Acoust. Soc. Am. 100*, 4 (1996), 2034–2048.

[6] Attenborough, K., LI, K., and Horoshenkov, K. *Predicting outdoor sound.* Taylor & Francis, London and New York, 2006.

[7] Baulac, M., Defrance, J., and Jean, P. Optimization of multiple edge barriers with genetic algorithms coupled with a nelder–mead local search. *J. Sound Vib. 300*, 1–2 (2007), 71 – 87.

[8] Berenger, J.-P. A perfectly matched layer for the absorption of electromagnetic waves. *J. Comp. Phys. 114*, 2 (1994), 185 – 200.

[9] Bot, A. L. A functional equation for the specular reflection of rays. *J. Acoust. Soc. Am. 112* (2002), 1276–1287.

[10] Botten, L. C., Nicorovici, N. A., McPhedran, R. C., Sterke, C. M. d., and Asatryan, A. A. Photonic band structure calculations using scattering matrices. *Phys. Rev. E 64* (2001), 046603.

[11] Bradley, J. A study of traffic noise around buildings. *Acustica 38* (1977), 247–252.

[12] Brillouin, L. *Wave propagation in periodic structures*, second ed. Dover Publications, Inc., 1953.

[13] Bullen, R., and Fricke, F. Sound propagation in a street. *J. Sound Vib. 46* (1975), 33 – 42.

[14] Bullen, R., and Fricke, F. Sound propagation at a street intersection in an urban environment. *J. Sound Vib. 54*, 1 (1977), 123 – 129.

[15] Can, A., Leclercq, L., Lelong, J., and Botteldooren, D. Traffic noise spectrum analysis: Dynamic modeling vs. experimental observations. *Appl. Acoust. 71* (2010), 764–770.

[16] Can, A., Leclercq, L., Lelong, J., and Botteldooren, D. Traffic noise spectrum analysis: Dynamic modeling vs. experimental observations. *Appl. Acoust. 71*, 8 (2010), 764 – 770.

[17] Champoux, Y., Allard, J., and Lauriks, W. Dynamic tortuosity and bulk modulus in air saturated porous media. *J. Appl. Phys. 70* (1991), 1975–1979.

[18] Craster, R. V., and Guenneau, S. *Acoustic metamaterials: negative refraction, imaging, lensing and cloaking*. Springer Science & Business Media, 2012.

[19] Davies, H. G. Noise propagation in corridors. *J. Acoust. Soc. Am. 53*, 5 (1973), 1253–1262.

[20] Davies, H. G. Multiple-reflection diffuse-scattering model for noise propagation in streets. *J. Acoust. Soc. Am. 64*, 2 (1978), 517–521.

[21] Depollier, C., Kergomard, J., and Lesueur, J. Propagation of low frequency acoustic waves in periodic 2d-lattices of tubes. *J. Sound Vib. 142*, 1 (1990), 153 – 170.

[22] Doc, J.-B., Lihoreau, B., and Félix, S. Higher order padé approximation for the parabolic equation in a varying cross-section waveguide. *Acta Acustica united with Acustica 98* (2012), 691–699.

[23] Duclos, A., Lafarge, D., and Pagneux, V. Transmission of acoustic waves through 2D phononic crystal: visco-thermal and multiple scattering effects. *Eur. Phys. J.: Appl. Phys. 45*, 1 (2009), 1.

[24] Duhamel, D., Sergent, P., Hua, C., and Cintra, D. Measurement of active control efficiency around noise barriers. *Appl. Acoust. 55*, 3 (1998), 217 – 241.

[25] Fang, N., Xi, D., Xu, J., Ambati, M., Srituravanich, W., Sun, C., and Zhang, X. Ultrasonic metamaterials with negative modulus. *Nature Materials 6* (2006), 452–456.

[26] Félix, S., Asch, M., Filoche, M., and Sapoval, B. Localization and increased damping in irregular acoustic cavities. *J. Sound Vib. 299* (2007), 965–976.

[27] Félix, S., and Pagneux, V. Multimodal analysis of acoustic propagation in three-dimensional bends. *Wave Motion 36*, 2 (2002), 157 – 168.

[28] Félix, S., and Pagneux, V. Sound attenuation in lined bends. *J. Acoust. Soc. Am. 116*, 4 (2004), 1921–1931.

[29] Félix, S., Sapoval, B., Filoche, M., and Asch, M. Enhanced wave absorption through irregular interfaces. *Eurpophysics Letters 85* (2009), 14004.

[30] Feng, L., Liu, X.-P., Lu, M.-H., Chen, Y.-B., Chen, Y.-F., Mao, Y.-F., Zi, J., Zhu, Y.-Y., Zhu, S.-N., and Ming, N.-B. Refraction control of acoustic waves in a square-rod-constructed tunable sonic crystal. *Phys. Rev. B 73* (2006), 193101.

[31] Groby, J.-P., Duclos, A., Dazel, O., Boeckx, L., and Lauriks, W. Absorption of a rigid frame porous layer with periodic circular inclusions backed by a periodic grating. *J. Acoust. Soc. Am. 129*, 5 (2011), 3035–3046.

[32] Groby, J.-P., Lauriks, W., and Vigran, T. Total absorption peak by use of a rigid frame porous layer backed by a rigid multi-irregularities grating. *J. Acoust. Soc. Am. 127*, 5 (2010), 2865–2874.

[33] Guillaume, G., Picaut, J., Dutilleux, G., and Gauvreau, B. Time-domain impedance formulation for transmission line matrix modelling of outdoor sound propagation. *J. Sound Vib. 330*, 26 (2011), 6467 – 6481.

[34] Heimann, D. Three-dimensional linearised euler model simulations of sound propagation in idealised urban situations with wind effects. *Appl. Acoust. 68*, 2 (2007), 217 – 237.

[35] Hein, S., Koch, W., and Nannen, L. Trapped modes and Fano resonances in two-dimensional acoustical duct-cavity systems. *J. Fluid Mech. 692* (2012), 257–287.

[36] Hewett, D. P. *Sound Propagation in an Urban Environment.* PhD thesis, St Catherine's College. University of Oxford, 2010.

[37] Hornikx, M., and Forssén, J. The 2.5-dimensional equivalent sources method for directly exposed and shielded urban canyons. *J. Acoust. Soc. Am. 122*, 5 (2007), 2532–2541.

[38] Hornikx, M., and Forssén, J. A scale model study of parallel urban canyons. *Acta Acustica united with Acustica 94* (2008), 265–281.

[39] Hornikx, M., and Forssén, J. Noise abatement schemes for shielded canyons. *Appl. Acoust. 70*, 2 (2009), 267 – 283.

[40] Hornikx, M., and Forssén, J. Noise abatement schemes for shielded canyons. *Appl. Acoust. 70* (2009), 267–283.

[41] Hornikx, M., and Forssén, J. Modelling of sound propagation to three-dimensional urban courtyards using the extended Fourier PSTD method. *Appl. Acoust. 72* (2011), 665–676.

[42] Hu, J., and Menyuk, C. R. Understanding leaky modes: slab waveguide revisited. *Adv. Opt. Photon 1* (2009), 58–106.

[43] Ishizuka, T., and Fujiwara, K. Performance of noise barriers with various edge shapes and acoustical conditions. *Appl. Acoust. 65*, 2 (2004), 125 – 141.

[44] Iu, K. K., and Li, K. M. The propagation of sound in narrow street canyons. *J. Acoust. Soc. Am. 112*, 2 (2002), 537–550.

[45] Joannopoulos, J. D., Johnson, S. G., Winn, J. N., and Meade, R. D. *Photonic Crystals. Molding the flow of light.* Princeton University Press, New Jersey, 2008.

[46] John, S. Strong localization of photons in certain disordered dielectric superlattices. *Phys. Rev. Lett. 58* (1987), 2486–2489.

[47] Johnson, D., Koplik, J., and Dashen, R. Theory of dynamic permeability and tortousity in fluid-saturated porous media. *J. Fluid Mech. 176* (1987), 1379–402.

[48] Kang, J. Numerical modelling of the sound fields in urban streets with diffusely reflecting boundaries. *J. Sound Vib. 258* (2002), 793–813.

[49] Kang, J. Numerical modelling of the sound fields in urban square. *J. Acoust. Soc. Am. 117* (2005), 3695–3706.

[50] Kang, J. *Urban Sound Environment.* Taylor & Francis, London and New York, 2007.

[51] Khelif, A., Wilm, M., Laude, V., Ballandras, S., and Djafari-Rouhani, B. Guided elastic waves along a rod defect of a two-dimensional phononic crystal. *Phys. Rev. E 69* (Jun 2004), 067601.

[52] Lihoreau, B., Gauvreau, B., Bérengier, M., Blanc-Benon, P., and Calmet, I. Outdoor sound propagation modeling in realistic environments: Application of coupled parabolic and atmospheric models. *J. Acoust. Soc. Am. 120*, 1 (2006), 110–119.

[53] Lyon, R. H. Role of multiple reflections and reverberation in urban noise propagation. *J. Acoust. Soc. Am. 55*, 3 (1974), 493–503.

[54] Markos, P., and Soukoulis., C. M. *Wave Propagation: From Electrons to Photonic Crystals and Left-Handed Materials.* Princeton University Press, New Yersey, 2008.

[55] Matínez-Sala, R., Sancho, J., Sánchez, J. V., Gomez, V., LLinares, J., and Meseguer, F. Sound attenuation by sculpture. *Nature 378* (1995), 241.

[56] Molerón, M., Félix, S., Pagneux, V., and Richoux, O. Sound propagation in periodic urban areas. *J. Appl. Phys. 111*, 11 (2012), 114906.

[57] Molerón, M., Félix, S., Pagneux, V., and Richoux, O. Low frequency acoustic resonances in urban courtyards. *J. Acoust. Soc. Am.* (to be submitted).

[58] Möser, M., and Volz, R. Improvement of sound barriers using headpieces with finite acoustic impedance. *J. Acoust. Soc. Am. 106*, 6 (1999), 3049–3060.

[59] Ögren, M., and Kropp, W. Road traffic noise propagation between two dimensional city canyons using an equivalent sources approach. *Acta Acustica united with Acustica 90(2)* (2004), 293–300.

[60] Ögren, M., and W., K. Road traffic noise propagation between two dimensional city canyons using an equivalent source approach. *Acta Acustica united with Acustica 90* (2004), 293–300.

[61] Öhrström, E., Skåberg, A., and Gidölf-Gunnarsson, A. Effects of road traffic noise and the benefit of access to quietness. *J. Sound Vib. 295* (2006), 40–59.

[62] Ouis, D. Annoyance from road traffic noise: A review. *J. Environ. Psychol. 21* (2001), 101–120.

[63] Ouis, D. Annoyance from road traffic noise: a review. *J. Environ. Psychol. 21*, 1 (2001), 101 – 120.

[64] Pagneux, V., Amir, N., and Kergomard, J. A study of wave propagation in varying cross-section waveguides by modal decomposition. Part i. theory and validation. *J. Acoust. Soc. Am. 100*, 4 (1996), 2034–2048.

[65] Pelat, A. *Approche modale de la propagation acoustique dans les guides d'ondes ouverts. Application à l'acoustique urbaine.* PhD thesis, Université du Maine, 2009.

[66] Pelat, A., Félix, S., and Pagneux, V. On the use of leaky modes in open waveguides for the sound propagation modeling in street canyons. *J. Acoust. Soc. Am. 126*, 6 (2009), 2864–2872.

[67] Pelat, A., Félix, S., and Pagneux, V. A coupled modal-finite element method for the wave propagation modeling in irregular open waveguides. *J. Acoust. Soc. Am. 129*, 3 (2011), 1240–1249.

[68] Picaut, J. Numerical modeling of urban sound fields by a diffusion process. *Appl. Acoust. 63*, 9 (2002), 965 – 991.

[69] Picaut, J., Hardy, J., and Simon, L. Sound propagation in urban areas: A periodic disposition of buildings. *Phys. Rev. E 60* (1999), 4851–4859.

[70] Pichard, H., Richoux, O., and Groby, J.-P. Experimental demonstrations in audible frequency range of band gap tunability and negative refraction in two-dimensional sonic crystal. *J. Acoust. Soc. Am. 132*, 4 (2012), 2816–2822.

[71] Renterghem, T. V., and Botteldooren, D. The importance of roof shape for road traffic noise shielding in the urban environment. *J. Sound Vib. 329*, 9 (2010), 1422 – 1434.

[72] Renterghem, T. V., Salomons, E., and Botteldooren, D. Parameter study of sound propagation between city canyons with a coupled FDTD-PE model. *Appl. Acoust. 67*, 6 (2006), 487 – 510.

[73] Richoux, O., Tournat, V., and Le Van Suu, T. Acoustic wave dispersion in a one-dimensional lattice of non linear resonant scatterers. *Phys. Rev. E 75* (2007), 026615.

[74] Rogier, H., and De Zutter, D. Berenger and leaky modes in microstrip substrates terminated by a perfectly matched layer. *IEEE Trans. Microwave Theory Tech. 49*, 4 (2001), 712 –715.

[75] Romero-Garcia, V. *On the control of propagating acoustic waves in sonic crystals: analytical, numerical and optimization techniques.* PhD thesis, Universidad Politécnica de Valencia, 2010.

[76] Roure, A. *Propagation Guidée, étude des discontinuitées.* PhD thesis, Université d'Aix Marseille, 1976.

[77] Shi, S., Chen, C., and Prather, D. W. Plane-wave expansion method for calculating band structure of photonic crystal slabs with perfectly matched layers. *J. Opt. Soc. Am. A 21* (2004), 1769–1775.

[78] Sievenpiper, D. Forward and backward leaky wave radiation with large effective aperture from an electronically tunable textured surface. *IEEE Trans. Antennas Propag. 53*, 1 (2005), 236–247.

[79] Sievenpiper, D., Schaffner, J., Lee, J., and Livingston, S. A steerable leaky-wave antenna using a tunable impedance ground plane. *IEEE Antennas Wireless Propag. Lett. 1*, 1 (2002), 179 –182.

[80] Sievenpiper, D., Zhang, L., Broas, R., Alexopolous, N., and Yablonovitch, E. High-impedance electromagnetic surfaces with a forbidden frequency band. *IEEE Trans. Microwave Theory Tech. 47*, 11 (1999), 2059 –2074.

[81] Sugimoto, N., and Imahori, H. Localized mode of sound in a waveguide with Helmholtz resonators. *J. Fluid Mech. 546* (2006), 89–111.

[82] Van Renterghem, T., and Botteldooren, D. Prediction-step staggered-in-time FDTD: an efficient numerical scheme to solve the linearised equations of fluid dynamics in outdoor sound propagation. *Appl. Acoust. 68* (2007), 201–216.

[83] Van Renterghem, T., and Botteldooren, D. The importance of roof shape for road traffic noise shielding in the urban environment. *J. Sound Vib. 329* (2010), 1422–1434.

[84] Van Renterghem, T., Salomons, E., and Botteldooren, D. Parameter study of sound propagation between city canyons with a coupled FDTD-PE model. *Appl. Acoust. 67* (2006), 487–510.

[85] Vasseur, J. O., Deymier, P. A., Khelif, A., Lambin, P., Djafari-Rouhani, B., Akjouj, A., Dobrzynski, L., Fettouhi, N., and Zemmouri, J. Phononic crystal with low filling fraction and absolute acoustic band gap in the audible frequency range: A theoretical and experimental study. *Phys. Rev. E 65* (2002), 056608.

[86] Veisten, K., Smyrnova, Y., KLæboe, R., Hornikx, M., Mosslemi, M., and Kang, J. Valuation of green walls and green roofs as soundscape measures: Including monetised amenity values together with noise-attenuation values in a cost-benefit analysis of a green wall affecting courtyards. *Int. J. Environ. Res. Public Health 9* (2012), 3770–3788.

[87] Wang, X.-H., Gu, B.-Y., Li, Z.-Y., and Yang, G.-Z. Large absolute photonic band gaps created by rotating noncircular rods in two-dimensional lattices. *Phys. Rev. B 60* (1999), 11417–11421.

[88] Wiener, F. M., Malme, C. I., and Gogos, C. M. Sound propagation in urban areas. *J. Acoust. Soc. Am. 37*, 4 (1965), 738–747.

[89] World Health Organisation–Europe, Burden of desease from environmental noise-quantification of healthy life years in europe, 2011.

[90] Wu, F., Liu, Z., and Liu, Y. Acoustic band gaps created by rotating square rods in a two-dimensional lattice. *Phys. Rev. E 66* (2002), 046628.

[91] Wu, F., Liu, Z., and Liu, Y. Splitting and tuning characteristics of the point defect modes in two-dimensional phononic crystals. *Phys. Rev. E 69* (2004), 066609.

[92] Wu, T.-C., Wu, T.-T., and Hsu, J.-C. Waveguiding and frequency selection of lamb waves in a plate with a periodic stubbed surface. *Phys. Rev. B 79* (2009), 104306.

[93] Yablonovitch, E. Inhibited spontaneous emission in solid-state physics and electronics. *Phys. Rev. Lett. 58* (1987), 2059–2062.

# Sound propagation modelling in urban areas: from the street scale to the neighbourhood scale

**Miguel Ángel Molerón Bermúdez**

The improvement of the urban sound environment requires a good understanding of the acoustic propagation in urban areas. Available commercial softwares give the possibility to simulate urban acoustic fields at relatively low computational costs. However, these tools are mainly based on energy methods that do not contain information on the phase. Therefore, these tools are unable to capture interference effects (*e.g.*, resonances), providing a limited physical description of the acoustic field. Conversely, classical wave methods such as FEM, BEM or FDTD give the possibility to model interference effects, but their use is often restricted to very low frequencies due to discretisation and the huge extension of the propagation domain.

The main goal of this thesis is to develop efficient wave methods for the acoustic propagation modelling in extended urban areas, both in the frequency and time domain. The proposed approach is based on a coupled modal–finite elements formulation. The key idea is to consider the urban canyon as an open waveguide with a modal basis composed of leaky modes, *i.e.*, modes that radiate part of their energy into the atmosphere as they propagate. The approach combines a multimodal description of the acoustic field in the longitudinal direction and a finite elements computation of the transverse eigenmodes. This coupled approach, which has been successfully implemented at the scale of a single street, is extended in the present manuscript at a larger scale (the neighbourhood scale), in order to model problems arising in propagation domains containing many interconnected streets. A time domain version of the method, containing only the least damped mode, is also proposed.

Using these methods, we investigate wave phenomena arising in specific urban configurations, as forbidden frequency bands in periodic networks of interconnected streets, and resonances in inner yards. It is found that, despite the presence of significant radiative losses in the propagation medium, strong interference effects are still observed. Not only this result highlights the relevance of a wave approach to describe accurately urban acoustic fields at low frequencies, but it suggest the potential use of these phenomena to control the acoustic propagation in urban environments.

The last part of this dissertation presents a preliminary study on the use of metasurfaces (surfaces decorated with an array of resonators) to improve the performance of noise barriers. It is shown that, exciting resonances in these structures, it is possible to achieve some unconventional behaviours, including negative angles of reflection and low frequency sound absorption.